Suppression of multiple Scattering and imaging of nonlinear Scattering in Ultrasound imaging

Tollef Struksnes Jahren

Sammendrag

Arbeidet presentert er basert på en avbildningsmetode hvor det brukes en ultralyd pulse bestående av to frekvensbånd for å avbilde ulineær spredning fra harde partikle som mikro kalk. Frekvensbåndene er differensiert som et lavfrekvent manipuleringsbånd og et høyfrekvent avbildningsbånd med et forhold på i størrelsesorden 1 : 10. Denne avbildningsmetoden har vist suksess i å avbilde resonant ulineær spredning fra mikro bobler. Det å avbilde ulineær spredning fra harde partikler har derimot ikke vært mulig. Det kan vises at amplituden og fasen til den ulineære spredningen følger amplituden og fasen til pulsen bestående av de lave frekvenskomponentene. Derfor kreves det stor amplitude på den lavfrekvente pulsen når harde partikler avbildes. Det viser seg imidlertid at det ikke bare er den ulineære spredningen som påvirkes av økt amplitude. Den høyfrekvente pulsen opplever nå større trykkvariasjoner og blir derfor deformert. Det er denne deformeringen som maskerer signalkomponentene fra den ulineære spredningen. Derfor må denne deformeringen korrigeres for, for effektivt å kunne avbilde harde partikler.

I løpet av denne oppgaven har to agar-gel fantomer blitt bygget. I begge fantomene ble det montert plastikklag som skulle produsere reverberasjoner. Som harde partikler ble det brukt to stålstrenger med diameter $0.5mm$ og $0.3mm$ sammen med kalkpartikler med diameter på $190\mu m$. Bilder av fantomene ble tatt med vanlig gråtone avbildning og med den presenterte metoden. Deretter ble bildene evaluert og sammenlignet. I det første fantomet, Fantom A, ble en klasse 3 reverberasjon undertrykket ned i bakgrunnsstøyen og signal støy forholdet til en kalkpartikkel og to ståstrenger økte med 8-9dB. For det andre fantomet, Fantom B, ble signal støy forholdet til to stålstrenger økt med 11-12dB mot en klasse 1,2 reverberasjon.

Abstract

The work presented is based on an imaging method using dual-frequency band pulses for imaging of nonlinear scatters from stiff particles like micro calcifications. The pulse complex consist of a high-frequency imaging pulse and a low-frequency manipulation pulse which overlap in time. The frequency ratio between the two pulses is in the range of 10 : 1. This technique has already demonstrated to perform well while imaging resonant nonlinear scatters from such as micro bubbles. However, imaging of lower intensity nonlinear scatters from stiff particles has not yet been achieved. It can be shown that the magnitude and the polarity of the nonlinear scatters follows the magnitude and the polarity of the low-frequency pulse. Imaging of stiff particles requires higher manipulation pressure, but the manipulation pressure does not change the scattering only. The co-propagating high frequency pulse observes a non homogeneous low frequency pressure and becomes distorted. This distortion of the high frequency pulse masks the nonlinear scattering, and to achieve sufficient suppression of the linear scattering the distortion must be corrected for.

In this thesis two agar based phantoms have been made. In both phantoms reverberation layer(s) of plastic was mounted. Steel wires with diameters $0.5mm$, $0.3mm$ were positioned below the plastic layer(s) together with calcium particles of bead size $190\mu m$. Images of both phantoms have been compared using conventional B-mode imaging and the presented method. In the first phantom, Phantom A, the SNR for two steel wires and a calcium particle were increased by 8 - 9dB while class 3 reverberations were suppressed down to the backscatter noise level. Similarly for the second phantom, Phantom B, class 1,2 reverberations were suppressed and the SNR for two steel wires were increased by 11 - 12dB.

Preface

This thesis has been submitted to the Department of Physics at the Faculty of Natural Sciences at the Norwegian University of Science and Technology (NTNU). The research work presented is carried out at the Department of Circulation and Medical Imaging, the Faculty of Medicine at NTNU. The thesis describes theoretical considerations, computer simulations, laboratory work and has been under the supervision of Professor Bjørn A. J. Angelsen.

Acknowledgments

First of all I would like to thank my supervisor, Professor Bjørn A. J. Angelsen, for introducing me to the field of medical ultrasound. He has shared his knowledge and guided me through the work with my master thesis. I would also like to thank members of his group consisting of PhD students Johannes Kvam, Ole Martin Brende and Master student Ola Finneng Myhre. They are great individuals who are always open for discussions. The support of Assistant Professor Tonni F. Johansen and Senior Researcher Rune Hansen with technical challenges regarding the Ultrasonix system and the SURF transducer VORA II is greatly appreciated. I would like to acknowledge PhD student Mercy Afadzi, Thomas Brakstad and Stig Tore Svee for the help they gave me when producing the two phantoms. At last I would like to thank Professor Catharina de Lange Davies for being my official main supervisor.

Contents

CHAPTER 1

Introduction

Medical ultrasound is mostly associated with fetal imaging and imaging of the human heart. The strength of medical ultrasound is its relatively low cost, easy to use and non-ionizing while providing real time images. However, ultrasound is also known to produce noisy images, with poor resolution and many artifacts.

In screening for breast cancer, mammography is used since micro calcification is recognizable on x-ray pictures [9]. Micro calcification indicates pathological changes in the breast [12], and biopsies are therefore taken from the suspicious areas. The biopsy needle can be guided with ultrasound as the needle is clearly visible on ultrasound images. However, to achieve accurate biopsies ultrasound imaging of micro calcification is important. The Second order UltRasound Field (SURF) imaging technique applied in this thesis may have the ability to enhance imaging of stiff particles such as micro calcification.

Similar to tissue harmonic imaging utilizes SURF the nonlinearity of human tissue. Tissue harmonic imaging utilizes the nonlinear accumulation of harmonics to suppress reverberations, and is suitable to suppress reverberations within the body wall. SURF imaging on the other hand uses the direct pressure dependent propagation velocity, and reverberation suppression is not limited by depth.

SURF imaging is a dual-frequency band technique [8] where the conventional imaging pulse is manipulated by a second lower frequency pulse. In imaging of nonlinear scatters such as contrast agent (micro bubbles) or stiff particles (micro calcification) SURF uses the same principle as Pulse Inversion (PI) [16]. Two (or more) pulses are transmitted in each direction with opposite phase. Unlike for PI the imaging pulses are not flipped, but rather the manipulation pulse. The manipulation pulse has shown to sufficiently modify the resonance frequency of micro bubbles, and SURF imaging perform well imaging contrast agents [10].

However, in imaging of micro calcification higher amplitude on the manipulation pulse is needed to modify the scattering properties. This becomes a challenge as the manipulation pulse modifies the imaging pulse differently for the two polarities of the manipulation pulse. The SURF imaging technique has therefore not yet been able to sufficiently improve the imaging of micro calcification.

Structure of this paper

The subject of this thesis is investigation of nonlinear scatters from stiff particles surrounded by soft tissue. Suppression of linear scatters and reverberations are studied through computer simulations and recordings from two phantoms.

Chapter 2 introduce the reader to nonlinear wave theory and the theory behind SURF imaging.

Chapter 3 contains the making of two agar gel based ultrasound phantoms.

Chapter 4, the dual-band ultrasound system is described, and the performance of the SURF transducer is investigated through computer simulations.

Chapter 5 describes how the received rf data from a SURF pulse complex is characterized, and an estimation method used for obtaining the phase relation between two SURF pulses is also presented.

Chapter 6, the material properties of the agar gel are obtained to be used in field simulations.

Chapter 7 starts with an investigation of the SURF transmit setup, before the SURF signal processing are given. A correction filer for the differences between the imaging pulses with opposite manipulation pressure is obtained from field simulations. At the end images of the two phantoms are presented where different signal processing have been used.

Chapter 8 discussion.

Chapter 9 conclusion is presented.

In the Appendixes, information of the simulation tools are given. The beamfield from the used SURF transducer is characterized through water tank recordings. At the end the Matlab code created for curve fitting the estimated time delays between to SURF pulses is given.

<div align="right">

CHAPTER 2

</div>

Ultrasound Theory

This chapter gives an introduction to Ultrasound (US) terminology, and the notation will follow Angelsen [13],[14]. The following is a repetition of nonlinear acoustics which will describe phenomenons in the presented imaging method SURF imaging.

2.1 Wave theory

This section gives a mathematical derivation of the 2nd order nonlinear wave equation for wave propagation in an absorbing heterogeneous medium. Start by defining:

- $\underline{\psi}(\underline{r}, t)$ - Particle displacement vector

- $p(\underline{r}, t)$ - Acoustic pressure

- $\underline{u}(\underline{r}, t) = \underline{\dot{\psi}}(\underline{r}, t)$ - Particle velocity vector

The vector $\underline{r}$ is defined as the distance from the unstrained equilibrium position which corresponds to Lagrangian coordinates. The acoustic pressure, p, is essentially the pressure difference from the ambient pressure, P_0, given by $p = P - P_0$. The nonlinearity in pressure, P, is often modeled as a Taylor expansion of the mass density, ρ. Writing the mass density at the same form as for the pressure, $\rho_1 = \rho - \rho_0$, where ρ_0 is the density of the unstrained material. The 2nd order Taylor expansion of the pressure becomes:

$$P = P_0 + \left.\frac{\partial P}{\partial \rho}\right|_{\rho=\rho_0, S} (\rho - \rho_0) + \left.\frac{\partial P}{\partial \rho}\right|_{\rho=\rho_0, S} (\rho - \rho_0)^2 \qquad (2.1)$$

The subscript S indicates constant entropy, meaning no absorption by heat generation during contraction/expansion of a volume element. Now A and B are introduced for simplicity when Eq. (2.1) is rewritten in terms of the acoustic pressure, p, and the relative change in ρ.

$$p = A\frac{\rho_1}{\rho_0} + \frac{B}{2}\frac{\rho_1^2}{\rho_0^2} \qquad A = \rho_0 \left.\frac{\partial P}{\partial \rho}\right|_{\rho=\rho_0,S} \qquad B = \rho_0^2 \left.\frac{\partial^2 P}{\partial \rho^2}\right|_{\rho=\rho_0,S} \qquad (2.2)$$

Through conservation of mass the relative change in mass density and the relative change in volume are linked as.

$$\rho_0 \Delta V_0 = \rho(\Delta V_0 + \delta V) \implies \frac{\rho_1}{\rho_0} = -\frac{\frac{\delta V}{\Delta V_0}}{1 + \frac{\delta V}{\Delta V_0}} \qquad (2.3)$$

The relative volume compression of an infinitesimal small volume element can be related to the particle displacement as.

$$\frac{\delta V}{\Delta V} = \nabla \underline{\psi} \qquad (2.4)$$

Further Eq. (2.3) can be approximated to since $\frac{\delta V}{\Delta V_0} \ll 1$, and by combining it with Eq. (2.4) the expression of the relative change in mass density takes the form.

$$\frac{\rho_1}{\rho_0} = -\nabla \underline{\psi}(1 - \nabla \underline{\psi}) \qquad (2.5)$$

Substituting the expression for ρ_1/ρ_0 into Eq. (2.2) gives the tissue elasticity equation

$$p = -A\nabla \underline{\psi} + A\beta_n (\nabla \underline{\psi})^2 + O(\nabla \underline{\psi}^3) \qquad \beta_n = 1 + \frac{B}{2A} \qquad (2.6)$$

By a second order approximated solution for $\nabla \underline{\psi}$ together with adding a term accounting for absorption we get.

$$\nabla \underline{\psi} = -\kappa(\underline{r})\,p + \beta_n(\underline{r})\left(\kappa(\underline{r})\,p\right)^2 - \kappa(\underline{r})h(\underline{r},t) \underset{t}{\otimes} p \qquad (2.7)$$

Here κ and $\beta_n \kappa^2$ are respectively parameters for the linear and nonlinear bulk compressibility. κ is given by $\kappa = 1/A$, β_n is given by Eq. (2.6), and both κ and β_n are functions of $\underline{r}$ in heterogeneous media. The last term represents the various mechanisms of absorption. To derive the wave equation we introduce the conservation of momentum obtained from Newtons 2nd law. Sound waves in medical US are directive beams with slightly curved phase front when focused, but they can often be approximated as plane waves [14]. This assumption forms the linear conservation of momentum equation

$$\frac{\partial \underline{u}}{\partial t} = -\frac{1}{\rho(\underline{r})}\left(\nabla p(1 + \nabla \underline{\psi}) + (\nabla p \cdot \nabla)\underline{\psi}\right) \approx -\frac{1}{\rho(\underline{r})}\nabla p \qquad (2.8)$$

By differentiating Eq. (2.7) twice with respect to time and inserting Eq. (2.8) into Eq. (2.7), we achieve the wave equation for the acoustic pressure.

$$\nabla\left(\frac{1}{\rho(\underline{r})}\nabla p\right) = \kappa(\underline{r})\frac{\partial^2 p}{\partial t^2} - \beta_n(\underline{r})\kappa(\underline{r})^2\frac{\partial^2 p^2}{\partial t^2} + \kappa(\underline{r})h(\underline{r},t) \underset{t}{\otimes} \frac{\partial^2 p}{\partial t^2} \qquad (2.9)$$

For further investigation of the wave equation, the linear compressibility, κ, the mass density, ρ and β_n can be separated into a slowly varying (scale $> \lambda$) component and a rapidly varying

4

(scale $< \lambda$) component. The notation will follow a subscript of either a for average or f for fluctuation.

$$\rho(\underline{r}) = \rho_a(\underline{r}) + \rho_f(\underline{r}) \tag{2.10}$$

$$\kappa(\underline{r}) = \kappa_a(\underline{r}) + \kappa_f(\underline{r}) \tag{2.11}$$

$$\beta_n(\underline{r}) = \beta_{na}(\underline{r}) + \beta_{nf}(\underline{r}) \tag{2.12}$$

For a more intuitively understanding $\gamma(\underline{r})$ and $\sigma(\underline{r})$ are presented as linear scattering parameters.

$$\gamma(\underline{r}) = \frac{\rho_f(\underline{r})}{\rho(\underline{r})} \qquad \sigma_l(\underline{r}) = \frac{\kappa_f(\underline{r})}{\kappa_a(\underline{r})} \tag{2.13}$$

Rewriting $\rho(\underline{r})$ and $\kappa(\underline{r})$ as they appear in Eq. (2.9) in terms of the new linear scattering parameters gives.

$$\frac{1}{\rho(\underline{r})} = \frac{\rho_a(\underline{r})}{\rho(\underline{r})\rho_a(\underline{r})} = \frac{\rho(\underline{r}) - \rho_f(\underline{r})}{\rho(\underline{r})\rho_a(\underline{r})} = \frac{1}{\rho_a(\underline{r})}\Big(1 - \gamma(\underline{r})\Big)$$
$$\kappa(\underline{r}) = \kappa_a(\underline{r})\Big(1 + \sigma_l(r)\Big) \tag{2.14}$$

Similarly a parameter for nonlinear scattering can be found as.

$$\sigma_n(\underline{r}) = \Big(2 + \sigma_l(\underline{r})\Big)\sigma_l(\underline{r})\beta_{na}(\underline{r})\kappa_a(\underline{r}) + \Big(1 + \sigma_l(\underline{r})\Big)^2\beta_{nf}(\underline{r})\kappa_a(\underline{r}) \tag{2.15}$$

By substituting $1/\rho(\underline{r})$ and $\kappa(\underline{r})$ from Eq. (2.14) into Eq. (2.9), and include the nonlinear scattering parameter the wave equation can be written as.

$$\underbrace{\nabla^2 p(\underline{r}, t) - \frac{1}{c_0^2(\underline{r})}\frac{\partial^2 p(\underline{r}, t)}{\partial t^2}}_{\text{Linear propagation}} + \underbrace{\frac{\beta_{na}(\underline{r})\kappa_a(\underline{r})}{c_0^2(\underline{r})}\frac{\partial^2 p(\underline{r}, t)^2}{\partial t^2}}_{\text{Nonlinear propagation}} - \underbrace{h(\underline{r}, t) \underset{t}{\otimes} \frac{1}{c_0^2}\frac{\partial^2 p(\underline{r}, t)}{\partial t^2}}_{\text{Absorption}}$$
$$= \underbrace{\frac{\sigma_l(\underline{r})}{c_0^2(\underline{r})}\frac{\partial^2 p(\underline{r}, t)}{\partial t^2} + \nabla\Big(\gamma(\underline{r})\nabla p(\underline{r}, t)\Big)}_{\text{Linear scattering source terms}} - \underbrace{\frac{\sigma_n(\underline{r})}{c_0^2(\underline{r})}\frac{\partial^2 p(\underline{r}, t)^2}{\partial t^2}}_{\text{Nonlinear scattering source terms}} \tag{2.16}$$

Here c_0 is defined as the linear wave velocity

$$c_0(\underline{r}) = \frac{1}{\sqrt{\rho_a(\underline{r})\kappa_a(\underline{r})}} \tag{2.17}$$

To get the wave equation on this form we have used $\nabla\rho_a \approx 0$, and in the absorption term $\kappa(\underline{r})$ has been approximated to $\kappa_a(\underline{r})$.

5

Eq. (2.16) shows that the rapid fluctuation in material parameters can be modeled as source terms in the wave equation. The linear scattering source term can be divided into a monopole source with strength $\sigma_l c_o^{-2} \partial^2 p / \partial t^2$ and a dipole source with strength $\gamma \nabla p$. The nonlinear scattering source term originates from the nonlinear term in the tissue elasticity equation, and has the strength $\sigma_n c_o^{-2} \partial^2 p / \partial t^2$. The nonlinear propagation term is responsible for the accumulative generation of second harmonics. To visualize this effect is it convenient to write Eq. (2.16) in terms of the momentum potential, ϕ, where the propagation term both include linear and nonlinear propagation. The momentum potential is defined by:

$$p(\underline{r}, t) = \frac{\partial \phi(\underline{r}, t)}{\partial t} \tag{2.18}$$

Writing the quadratic terms in Eq. (2.16) as

$$\frac{\partial}{\partial t} \frac{\partial p^2(\underline{r}, t)}{\partial t} = \frac{\partial}{\partial t} 2p(\underline{r}, t) \frac{\partial p(\underline{r}, t)}{\partial t} = \frac{\partial}{\partial t} 2p(\underline{r}, t) \frac{\partial^2 \phi(\underline{r}, t)}{\partial t^2} \tag{2.19}$$

and integrating every term with respect to time, before collecting the linear and nonlinear propagation terms, Eq. (2.16) becomes

$$
\underbrace{\nabla^2 \phi(\underline{r}, t) - \frac{1}{c^2(\underline{r}, p(\underline{r}, t))} \frac{\partial^2 \phi(\underline{r}, t)}{\partial t^2}}_{\text{Nonlinear propagation}} - \underbrace{h(\underline{r}, t) \underset{t}{\otimes} \frac{1}{c_0^2} \frac{\partial^2 \phi(\underline{r}, t)}{\partial t^2}}_{\text{Absorption}}
$$
$$
= \underbrace{\frac{\sigma_l(\underline{r})}{c_0^2(\underline{r})} \frac{\partial^2 \phi(\underline{r}, t)}{\partial t^2} + \nabla \Big(\gamma(\underline{r}) \nabla \phi(\underline{r}, t) \Big)}_{\text{Linear scattering source terms}} - \underbrace{\frac{\sigma_n(\underline{r}) 2p(\underline{r}, t)}{c_0^2(\underline{r})} \frac{\partial^2 \phi(\underline{r}, t)}{\partial t^2}}_{\text{Nonlinear scattering source terms}}
\tag{2.20}
$$

$$
\begin{aligned}
c^2(\underline{r}, p(\underline{r}, t)) &= \frac{c_0^2(\underline{r})}{1 - \beta_{na}(\underline{r}) \kappa_a(\underline{r}) 2p(\underline{r}, t)} \\
c(\underline{r}, p(\underline{r}, t)) &\approx c_0(\underline{r}) \Big(1 + \beta_{na}(\underline{r}) \kappa_a(\underline{r}) p(\underline{r}, t) \Big)
\end{aligned}
\tag{2.21}
$$

In Eq. (2.21) $|\beta_{na}(\underline{r}) \kappa_a(\underline{r}) p(\underline{r}, t)| \ll 1$ was used. The motivation for deriving an explicit equation is to show that the wave velocity is dependent on the pressure, where the wave velocity is higher in the compression phase than in the rarefaction phase. During propagation the effect will produce an accumulative pulse distortion and create higher harmonics in the transmitted wave. Below are figures illustrating pulse distortion, the pulses are plotting in retarded time and the front of the pulses are to the right.
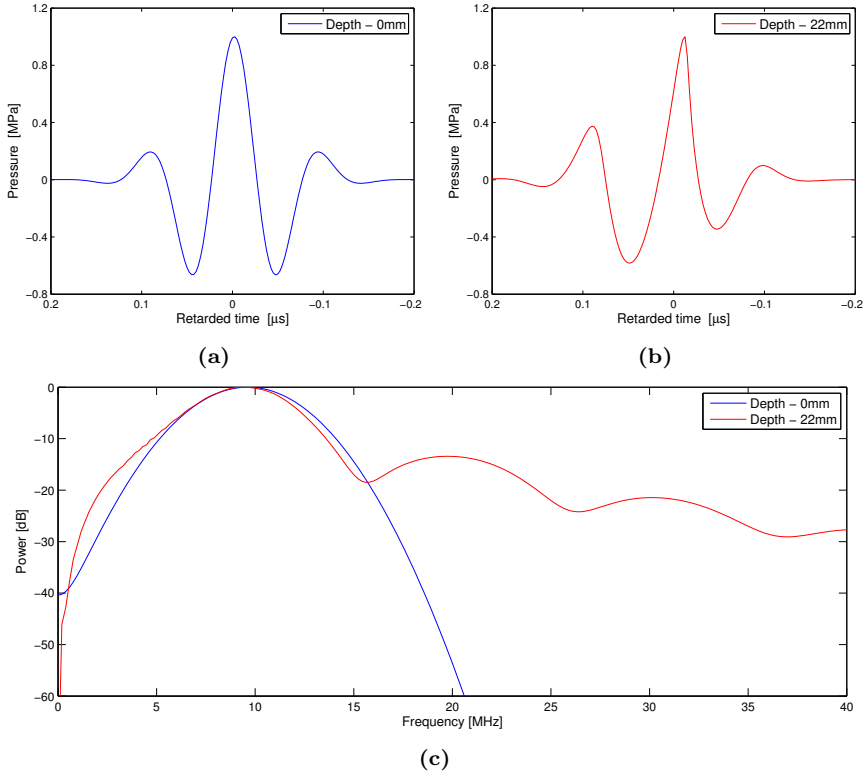
Figure 2.1: *Illustration of pulse distortion from nonlinear propagation. The images are taken from a simulation done with ForwardSIM App. (A.1). (a) shows an excited Gaussian pulse at the transducer surface (Depth = 0mm) in retarded time ($\tau = t - z/c_0$). The same pulse at the focus (Depth = 22mm) is shown in (b). Both pulses are normalized for simply illustrating the change in pulse form. The corresponding frequency components of the pulses in (a) and (b) are displayed in (c). The medium properties was given a low attenuation coefficient to exhibit sufficient amount of distortion.*

Although the pulses get distorted they will never achieve the sawtooth pulse form or acoustic shock, because the absorption term in Eq. (2.20) for tissue is almost linearly frequency dependent. Eq. (2.20) also illustrates that the strength of the nonlinear scatters are pressure dependent.

2.2 SURF imaging

This chapter will cover the principles of Second Order UltRasound Field (SURF) imaging. The technique was developed at the Department of Circulation and Medical Imaging (ISB), NTNU. It utilizes dual frequency band pulse complexes whereas conventional US imaging single frequency band pulses are transmitted. The frequency band around the low center-frequency will be referred to as the LF (low-frequency), and similar, the frequency band around the high-frequency will be referred to as the HF (high frequency). The frequency ratio between the LF and the HF is typically 1/10. The HF is the imaging frequency band as in normal US imaging. The LF is used to manipulate the tissue characteristics, affecting both the nonlinear scattering properties and the forward propagation of the HF. The SURF imaging technique transmits at least two such dual frequency band pulses in each direction, where the polarity and/or amplitude of the LF is changed. An example of two SURF pulse complexes where the HF pulse is placed at the peak and the through of the LF pulse is seen in Fig. (2.2).
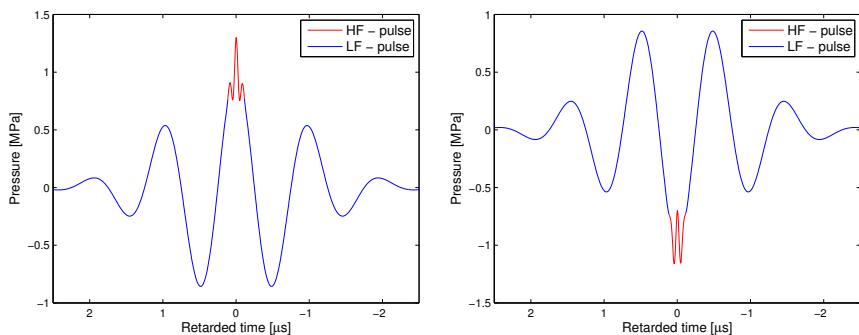
(a) *The HF pulse placed in the compression phase of the LF pulse.*

(b) *The HF pulse placed in the rarefaction phase of the LF pulse.*

Figure 2.2: *Two SURF pulse complexes with opposite positioning of the HF pulse relative to the LF pulse. In this example the HF pulse has a center frequency of $10MHz$ with length one and a half period, and the LF pulse has a center frequency of $1MHz$ with length two and a half period.*

Noise in US images can originate from reverberations, and SURF imaging has the ability to suppress these unwanted signal components. For imaging of nonlinear scatters, as ultrasound contrast agent and mirco-califications, SURF uses the same method as Pulse inversion, where the linear scatters are tried removed by subtraction of two signals. Current challenge of the SURF imaging method is to align the two signals from two SURF pulse complexes with different LF. Both because of the manipulated wave velocity and because of the nonlinear interactions between the LF and HF pulses. For this real-time estimation of a correction filter might be required.

2.2.1 Nonlinear interaction between the HF and LF pulse

With adequate acoustic pressure amplitude and a nonzero nonlinear material parameter, $\beta_n(\underline{r})$, the dual band pulse complex will experience a nonlinear interaction. By expanding the acoustic pressure in terms of the LF and HF

$$p(\underline{r},t) = p_{LF}(\underline{r},t) + p_{HF}(\underline{r},t) \tag{2.22}$$

the nonlinear quadratic term expands into:

$$p^2(\underline{r},t) = \underbrace{p_{LF}^2(\underline{r},t)}_{\text{Nonlinear self distortion}} + \underbrace{2\,p_{LF}(\underline{r},t)\,p_{HF}(\underline{r},t)}_{\text{Nonlinear interaction}} + \underbrace{p_{HF}^2(\underline{r},t)}_{\text{Nonlinear self distortion}} \tag{2.23}$$

The two nonlinear self distortion terms are responsible for the generation of harmonics explained in Section (2.1) and shown in Fig. (7.20). The amount of self distortion of the LF during forward propagation can be neglected since it only travels $\sim 26\lambda$ (for depth $40mm$ with frequency $1MHz$ and speed $1540m/s$). The HF correspondingly travels $\sim 260\lambda$ (for frequency 10MHz) and the self distortion can not be neglected [15]. The frequency components generation from the nonlinear interaction term are more easily seen in the temporal frequency domain, where the multiplication of the LF and HF pressure becomes a convolution.

$$\mathcal{F}\Big\{p_{LF}(\underline{r},t)\,p_{HF}(\underline{r},t)\Big\} = P_{LF}(\underline{r},\omega) \underset{\omega}{\otimes} P_{HF}(\underline{r},\omega) \tag{2.24}$$

This yields a production of signal components at the sum $(f_{HF}+f_{LF})$ and the difference $(f_{HF}-f_{LF})$ of the HF and LF frequencies.

A nonlinear propagation time delay

If the HF pulse is placed at the peak or through of the LF pulse, and the HF pulse is much shorter then half of the LF wave length, then the HF pulse experiences an almost constant LF pressure. The LF pressure modifies the stiffness and density of the tissue and the wave velocity of the HF pulse is changed. An explicit form for the influenced HF wave velocity can be found by: First inserting the expanded form of the pressure from Eq. (2.22) and Eq. (2.23) into the propagation terms in Eq. (2.16), and then approximating the p_{LF} to be constant over the HF pulse ($\partial p_{LF}(\underline{r},t)/\partial t \approx 0$).

$$\underbrace{\nabla^2(p_{LF}+p_{HF}) - \frac{1}{c_0^2(\underline{r})}\frac{\partial^2(p_{LF}+p_{HF})}{\partial t^2}}_{\text{Linear propagation}} + \underbrace{\frac{\beta_{na}(\underline{r})\kappa_a(\underline{r})}{c_0^2(\underline{r})}\frac{\partial^2(p_{LF}^2 + 2p_{LF}\,p_{HF} + p_{HF}^2)}{\partial t^2}}_{\text{Nonlinear propagation}}$$

$$\approx \underbrace{\nabla^2 p_{HF} - \frac{1}{c_0^2(\underline{r})}\frac{\partial^2 p_{HF}}{\partial t^2}}_{\text{HF: Linear propagation}} + \underbrace{\frac{2\beta_{na}(\underline{r})\kappa_a(\underline{r})p_{LF}}{c_0^2(\underline{r})}\frac{\partial^2 p_{HF}}{\partial t^2}}_{\text{HF: Nonlinear interaction}} + \underbrace{\frac{\beta_{na}(\underline{r})\kappa_a(\underline{r})}{c_0^2(\underline{r})}\frac{\partial^2 p_{HF}^2}{\partial t^2}}_{\text{HF: Nonlinear self distortion}}$$

$$+ \underbrace{\nabla^2 p_{LF} - \frac{1}{c_0^2(\underline{r})}\frac{\partial^2 p_{LF}}{\partial t^2}}_{\text{LF: Linear propagation}} + \underbrace{\frac{\beta_{na}(\underline{r})\kappa_a(\underline{r})}{c_0^2(\underline{r})}\frac{\partial^2 p_{LF}^2}{\partial t^2}}_{\text{LF: Nonlinear self distortion}} \tag{2.25}$$

$$\approx \underbrace{\nabla^2 p_{HF} - \frac{1}{c_0^2(\underline{r})\big(1 + 2\beta_{na}(\underline{r})\kappa_a(\underline{r})p_{LF}\big)} \frac{\partial^2 p_{HF}}{\partial t^2}}_{\text{HF: Nonlinear propagation}} + \underbrace{\frac{\beta_{na}(\underline{r})\kappa_a(\underline{r})}{c_0^2(\underline{r})} \frac{\partial^2 p_{HF}^2}{\partial t^2}}_{\text{HF: Nonlinear self distortion}}$$

$$+ \underbrace{\nabla^2 p_{LF} - \frac{1}{c_0^2(\underline{r})} \frac{\partial^2 p_{LF}}{\partial t^2}}_{\text{LF: Linear propagation}} + \underbrace{\frac{\beta_{na}(\underline{r})\kappa_a(\underline{r})}{c_0^2(\underline{r})} \frac{\partial^2 p_{LF}^2}{\partial t^2}}_{\text{LF: Nonlinear self distortion}}$$

$$(2.26)$$

The spatial and time dependence of the pressures where omitted for convenience. The manipulated HF wave velocity is:

$$c\Big(\underline{r}, p_{LF}(\underline{r})\Big) = \sqrt{c_0^2(\underline{r})\Big(1 + 2\beta_{na}(\underline{r})\kappa_a(\underline{r})p_{LF}(\underline{r})\Big)} \approx c_0(\underline{r})\Big(1 + \beta_{na}(\underline{r})\kappa_a(\underline{r})p_{LF}(\underline{r})\Big) \quad (2.27)$$

The time of flight, $t(\underline{r})$, for the HF pulse to reach a position $\underline{r}$ in space for a given trajectory (Γ) is calculated by

$$t(\underline{r}) = \int_{\Gamma(s)} \frac{ds}{c(s, p_{LF}(s))} \approx \int_{\Gamma(s)} \frac{ds}{c_0(s)} - \int_{\Gamma(s)} ds\, \frac{\beta_{na}(s)\kappa_a(s)p_{LF}(s)}{c_0(s)} = t_0(\underline{r}) + \tau(\underline{r})$$

$$t_0(\underline{r}) = \int_{\Gamma(s)} \frac{ds}{c_0(s)} \qquad \tau(\underline{r}) = - \int_{\Gamma(s)} ds\, \frac{\beta_{na}(s)\kappa_a(s)p_{LF}(s)}{c_0(s)}$$

$$(2.28)$$

where $t_0(\underline{r})$ is the unmanipulated propagation time. $\tau(\underline{r})$ will be referred to as the time delay, and is an important part of the SURF imaging signal processing. Eq. (2.28) also shows that the time delay and LF pressure have opposite signs.

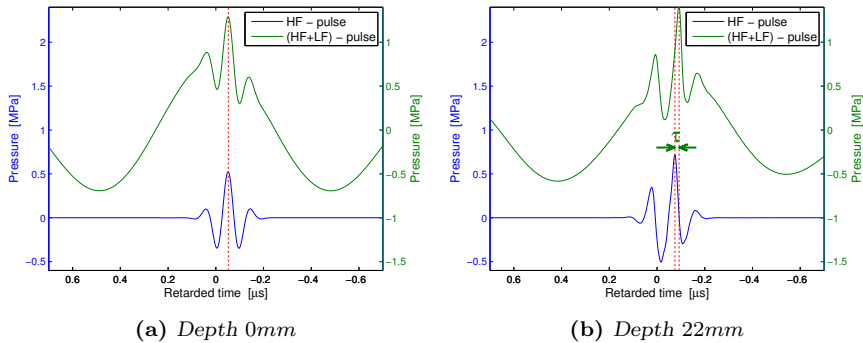**(a)** *Depth 0mm* **(b)** *Depth 22mm*

Figure 2.3: *Illustration of the time delay. (a) shows a transmitted SURF pulse complex and a HF pulse at the transducer surface. (b) shows the same two pulses at depth 22mm where the time delay, τ, is indicated with the green arrows.*

10

The approximation that the HF pulse observes a constant LF pressure over the whole pulse is not accurate. Because of this another effect of the pressure dependent velocity rises.

Pulse form distortion (PFD)

The consequence of the nonhomogeneous LF pressure experienced by the HF pulse causes various parts of the HF pulse to travel with different velocities. The pulse form distortion (PFD) will hence be accumulative. This effect changes the HF pulse form and length. Along the imaging pulse the pressure of the LF pulse can be modeled as $p_{LF} = p_{LF_a} + p_{LF_f}$, where the p_{LF_a} is the average pressure which is responsible for the nonlinear propagation time delay. The result of the fluctuating LF pressure, p_{LF_f}, is illustrated by green velocity arrows in Fig. (2.4).
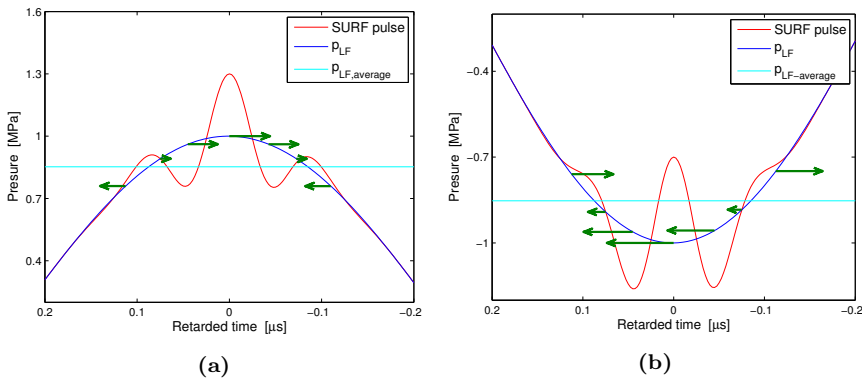

Figure 2.4: *Fluctuation of the LF manipulation pulse over the HF pulse shown for two opposite polarities of the LF. The green arrows indicate fluctuations in the HF wave velocity.*

The PFD of the HF pulse done by the LF pulse is not equal for both polarities of the LF pulse. Hence the received signal components will vary dependent on the LF pulse in addition to the propagation time delay.

Pulse form modification (PFM)

The pulse form modification (PFM) is made by transversal variations of the propagation time delay at the region of scatters. The variations in the propagation time delay originates from the transversal variations in the LF pressure, and the effect accumulates with depth. The PFM changes the interference between the received HF pulses in the beamformer.

2.2.2   SURF aberration

The difference in frequency, aperture size and focus between the HF and LF causes different diffraction patterns. Although the HF pulse can be placed nicely on top of the LF pulse for equal focused pulses at the transducer, the HF pulse will get phase changes both axially and laterally compared to the LF pulse during propagation. These phase changes cause various

parts of the HF pulse to travel at different velocities causing a phase-front aberration called SURF aberration. The effect is the same as for normal US aberration, by causing a blurry focus and increased side lobes. The blurry focus degrades the spatial resolution of the image and the increased side lobes reduces the contrast in the image. Due to these effects the transmit setup is important in SURF imaging. Three main setups can be investigated:

- Setup 1: Focused LF + Focused HF

- Setup 2: Unfocused LF + Focused HF
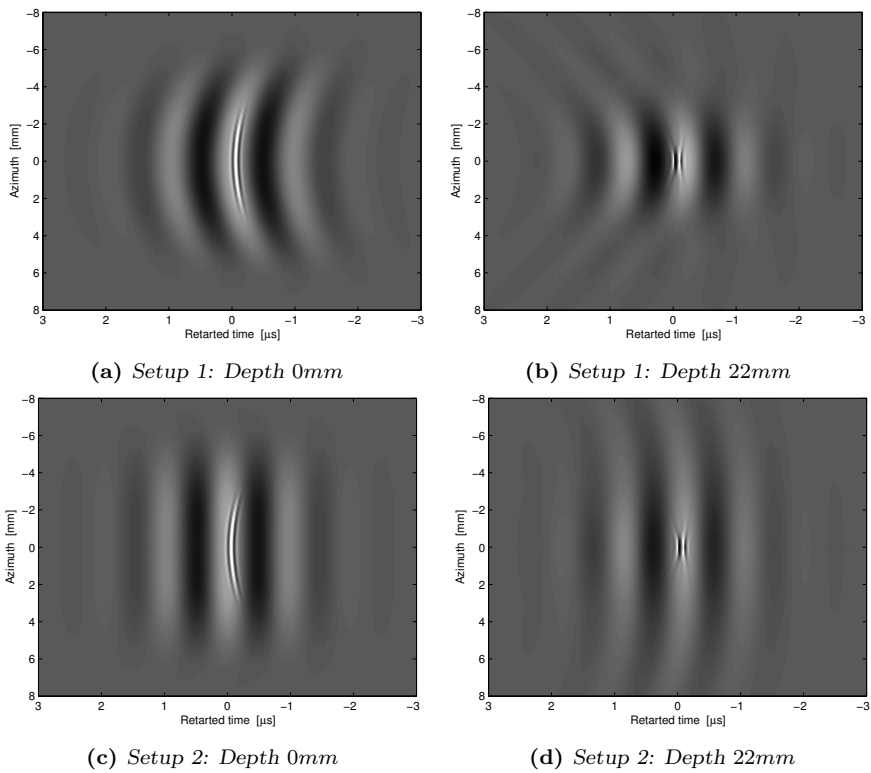
- Setup 3: Unfocused LF + unfocused HF

(a) *Setup 1: Depth 0mm*

(b) *Setup 1: Depth 22mm*

(c) *Setup 2: Depth 0mm*

(d) *Setup 2: Depth 22mm*

Figure 2.5

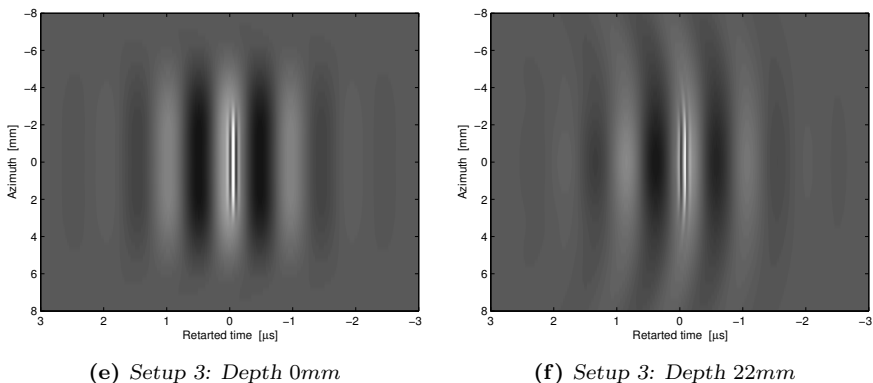**(e)** *Setup 3: Depth 0mm*   **(f)** *Setup 3: Depth 22mm*

Figure 2.5: *Illustration of the phase relation between the HF pulse and LF pulse for three different transmit setups. (If focused use, F = 22mm)*

The term "phase relation" will be used as the spatial distance between the maximum of the envelope of the HF pulse and the peak/through of the LF pulse. Setup 1 has a more even lateral phase relation than setup 2 close to the transducer, but due to sliding of the HF pulse during propagation setup 2 can have a better overall phase relation (sliding of the HF pulse will be treated in the next section). Focusing of the LF pulse also increases the manipulation pressure towards the focus, which can provide in a more nonlinear time delay curve as a function of depth (up to the LF focus). Setup 3 could be used in synthetic transmit and received beams, where the phase relation can be held small and the LF manipulation pressure can have little variation. The disadvantage with setup 3 is that it requires a more stationary imaging target. Comparison of beamforming strategies has been done in references [9] and [18]. In this thesis setup 2 will be used due to current software/hardware limitations.

Phase relation: Sliding of the HF pulse during propagation

As discussed in the last section the HF pulse is not positioned correctly at the top/trough of the LF pulse for all depths (as in Fig. (2.2)). In all focused systems propagation will produce a phase shift in the transmitted wave. The difference in the diffraction pattern between the HF pulse and the LF pulse causes the HF pulse to slide relative to the peak/trough on the LF pulse. To mathematically describe this phenomenon we review the non-absorbing homogeneous linear wave equation and show that the phase at the focal point is shifted by $\pi/2$ in the temporal frequency domain. The wave equation in terms of the momentum potential is:

$$\nabla^2 \phi - \frac{1}{c_o^2} \frac{\partial^2 \phi}{\partial t^2} = 0 \tag{2.29}$$

In reference [13] the Rayleigh integral for the momentum potential from a plane surface with rigid baffle is written in the temporal frequency domain as:

$$\Phi(\underline{r}, \omega) = H(\underline{r}, \omega) \ F(\omega) \tag{2.30}$$

13

Here, $F(\omega)$ is the surface vibration in the frequency domain and $H(\underline{r}, \omega)$ is the spatial frequency response at position $\underline{r}$. Now defining ρ as the homogeneous mass density, U_n as the normal surface velocity amplitude, k as the wave number and r_0 as the integration variable across the transducer surface, S_t, the spatial frequency response becomes:

$$H(\underline{r}, \omega) = \rho U_n \int_{S_t} dr_o^2 \frac{e^{-ik|\underline{r}-\underline{r_0}|}}{2\pi|\underline{r} - \underline{r_0}|} \tag{2.31}$$

Further, at the focal point (r_F) the spatial frequency response can be approximated to:

$$H(r_F, \omega) = \rho U_n \frac{e^{ikr_F}}{2\pi r_F} \int_{S_t} d\underline{r}_0^2 = \rho U_n \frac{e^{-ikr_F}}{2\pi r_F} S_t \tag{2.32}$$

By applying Eq. (2.18)

$$p(\underline{r}, t) = \frac{\partial \phi(\underline{r}, t)}{\partial t^2} \qquad \longleftrightarrow \qquad P(\underline{r}, \omega) = i\omega \Phi(\underline{r}, \omega) \tag{2.33}$$

we then get the pressure at the focal point:

$$p(r_F, t) = \frac{\partial}{\partial t}\left\{ f\left(t - \frac{r_F}{c}\right)\right\} \rho U_n \frac{e^{-ikr_F}}{2\pi r_F} S_t \qquad \longleftrightarrow \qquad P(r_F, \omega) = i\omega F(\omega) \rho U_n \frac{e^{-ikr_F}}{2\pi r_F} S_t \tag{2.34}$$

Eq. (2.34) shows by the $i\omega$ in front that the wave passing through the focal point have all frequency components shifted by $\pi/2$ compared to the transmitted wave. The peak/through of the LF pulse will hence get a $T_{LF}/4$ temporal change during propagation from the transducer surface to its focal point, and it is this LF peak/through movement that produces the relative sliding of the HF. If the HF is placed on the peak/through of the LF at the transducer surface, will it be located at the flank of the LF at the focal point and vice versa. An example of the HF sliding in the linear regime is shown in the figures below.
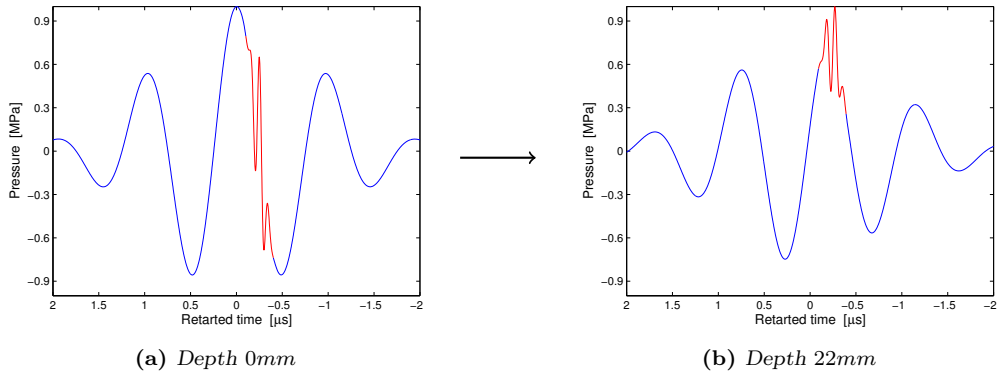

(a) *Depth 0mm*   (b) *Depth 22mm*

Figure 2.6

14

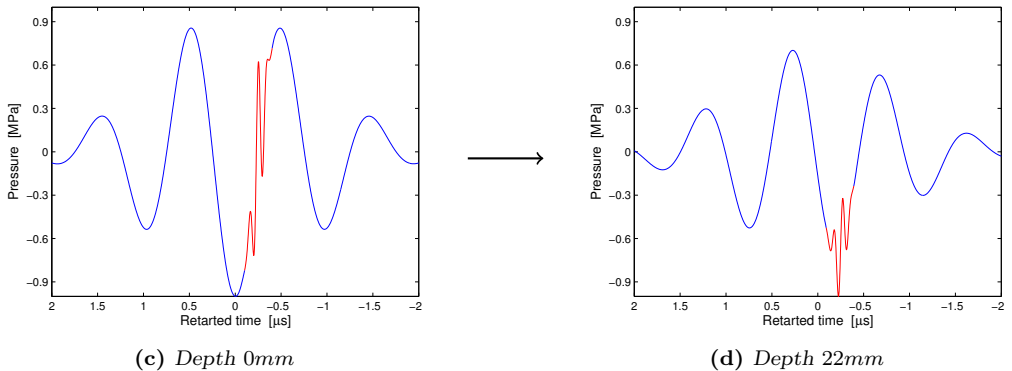**(c)** *Depth 0mm*   **(d)** *Depth 22mm*

Figure 2.6: *Sliding of the HF pulse relative to the LF manipulation pulse for two initial positions. (a) the HF is placed on a negative gradient, (b) the corresponding HF position on the LF at the focal point 22mm. (c) the HF is placed on a positive gradient, (d) the corresponding HF position on the LF at the focal point 22mm. For both the transmitted SURF pulse complexes where the LF and HF are focused at 22mm, Setup 1, the pulse amplitudes are also normalized.*

Especially when imaging micro calcification we do not want the HF to be on the zero crossing of the LF over the imaging region, since it is the LF manipulation pressure which produces the nonlinear scatters Eq. (2.39). For this reason the HF can initially be placed on the flank of the LF so it is located on the peak/through of the LF at the focal point. Now, remembering the effect of the variations of the LF manipulation pulse across the HF from Section (2.2.1). We can expect a frequency shift in the HF imaging pulse during propagation if positioned at the LF zero cross section [19]. From Eq. (2.27):

$$
\begin{aligned}
c &= c_0(1 + \beta_n \kappa \Delta p_{LF}) = c_0 + \Delta c \\
\Delta c &= c_0 \beta_n \kappa \Delta p_{LF}
\end{aligned}
\tag{2.35}
$$

Here is Δp_{LF} noted as the change in the LF pressure between two zero crossings of the HF pulse. After propagating a distance Δz the HF has experienced a frequency shift:

$$
\begin{aligned}
c_0 &= \frac{\Delta z}{t} \qquad \Delta c = \frac{\Delta \lambda}{t} \\
\Delta \lambda(\Delta z) &= \frac{\Delta c}{c_0} \Delta z = \beta_n \kappa \Delta p_{LF} \Delta z
\end{aligned}
\tag{2.36}
$$

$$
f_{HF}(z + \Delta z) = \frac{\lambda_{HF}(z)}{\lambda_{HF}(z) + \Delta \lambda_{HF}(\Delta z)} f_{HF}(z)
\tag{2.37}
$$

Eq. (2.36) and Eq. (2.37) show that the frequency shift is dependent of the LF gradient. The two scenarios in Fig. (2.6) have opposite polarities on the LF gradient, producing a frequency difference between the two HF imaging pulses. This creates an unequal diffraction pattern resulting in variation in the received RF signals by not only a time delay.

2.3   Scattering

Ultrasound scattering is the result of rapid fluctuations in the compressibility and density of the tissue, and the US image is a mapping of these variations. The US image is constructed by repeatedly transmitting pulses and recording the backscattered signals for a set of scan-lines. The depth coordinate of a beamformed received signal (for each scan-line) is located by the time of flight. The assumption that the received signals only consist of 1st order scattering is incorrect. Multiple scattering occurs and it produces a fine-grained noise in the image. We can separate scattering in two types, linear and nonlinear scattering. They vary in how the LF manipulation pulse effects the scattering properties.

2.3.1   Linear and nonlinear scattering

Scattering occurs at the interface between two medias with different acoustic impedance. In medical ultrasound such a change can be represented by the interface between soft tissue and fat-muscle. The characteristic acoustic impedance is defined in [13] for linear acoustic as

$$Z_o = \sqrt{\frac{\rho}{\kappa}} \tag{2.38}$$

Besides the change in acoustic impedance scattering is effected by the relative size between the object and the wavelength [13]. For this reason scattering can be divided into two classes: Scattering from large objects compared to the wavelength is called specular scattering, and can be treated by ray acoustics. Diffusive/Rayleigh scattering occurs when the wavelength is much large than the object.

In linear scattering the ratio between the interfacing materials the acoustic impedance is pressure independent. In SURF imaging then the linear scattering is unaffected by the LF manipulation pulse.

Nonlinear scattering on the other hand occurs at interfaces where the materials acoustic impedance vary dependently of the pressure amplitude. Such scatters are effected by the polarity and amplitude of LF manipulation pulse. The nonlinear scattering term in Eq. (2.16) can be approximated for the frequencies around the HF fundamental band as

$$\frac{2\sigma_n(\underline{r}}{c_0^2(\underline{r})}\frac{\partial^2 p(\underline{r}),t)^2}{\partial t^2} \approx \frac{2\sigma_n(\underline{r})p_L(\underline{r},t)}{c_o^2(\underline{r})}\frac{\partial^2 p_H(\underline{r},t)}{\partial t^2} \tag{2.39}$$

Scattering from ultrasound contrast agents such as micro bubbles are an example of nonlinear scattering. The micro bubbles are easily compressed and when insonified they behaves like a spring with a co-oscillating fluid as mass around. This resonant system hence yield a large amount of nonlinear scattered signal [14]. Micro calcification also yields nonlinear scattered signals, but unlike micro bubbles the backscattered signals are weak. Imaging techniques such as pulse inversion has not shown adequate signal to noise ratio, because of interfering signals by linear scattering from nonlinear propagation. With SURF imaging however, it is possible to distinguish between the pure nonlinear scattering and the linear

scattering from nonlinear propagation if the nonlinear propagation time delay and the pulse form distortion are corrected for.

The micro calcium particles are very stiff particles with almost zero compressibility compared to surrounding tissue. SURF imaging with a positive polarity on the LF manipulation pulse compresses the tissue. This compression decreases the tissue compressibility and makes the acoustic impedance more equal to that of the micro calcification, which yields in less backscattered signal. Similarly for negative polarity on the LF manipulation pulse increases the backscattered signal. Eq. (2.39) shows that the strength of the nonlinear scatters are linearly dependent on the LF manipulation pressure. As the micro calcification has a low scattering cross section, a high LF pressure amplitude is necessary.

2.3.2 Multiple scattering

Conventional ultrasound images are made with the assumption that only 1st order scattering occurs, hence the most dominating noise in pulse echo imaging origin from multiple scattering [15]. This type of noise will be referred to as multiple scattering noise or reverberation noise. SURF imaging has the potential to suppress reverberation noise, and this is an area of ongoing research.

The amplitude of the transmitted wave drops for each scattering, the most damaging noise is therefore from 3rd order scattering. Strong 2nd order scattering is only apparent for special structures e.g. the ribs [14]. Reverberation noise is critical in regions where the 1st order scatters are weak, for instance imaging of plaque in vessels or imaging of micro calcifications. For further study of the reverberations it is convenient to categorize the 3rd order scattering into classes.

Class I, Class II and Class III reverberations

The three classes are defined by the positions of the 1st and 3rd scatters.

Class I - 1st scattering occurs closest to the transducer $r_1 < r_3$

Class II - 1st scattering occurs farthest from the transducer $r_1 > r_3$

Class III - 1st and 3rd scattering occur at the same depth $r_1 = r_3$

Class I and class II reverberation noise will always co-exist since they have the same three scatters. An illustration of the three types of reverberations is in Fig. (2.7). From the figure: By varying the position of the 2nd scatter, r_2, a tail of weak echoes will be introduced behind r_3 and up to r. The strongest 2nd order scatter is often from the ultrasound transducer, which can have a reflection coefficient in the range of $10dB$ higher than for soft tissue structures [15]. The reflection coefficient of the transducer is frequency dependent and will therefore to some extent change the pulse from.
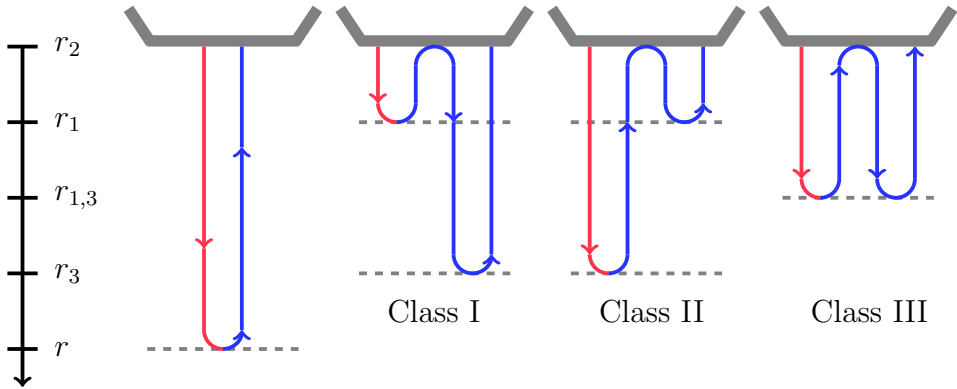
Figure 2.7: *To the left 1st order scattering and to the right the three classes of 3rd order scattering. The red and blue lines indicate an approximation to nonlinear and linear propagation respectively.*

Assuming the 2nd order scatter is located at the transducer, can we write the relations between the scattering positions:

$$r = r_1 + r_3 \qquad\qquad r = r_{1,3} + r_{1,3} \qquad\qquad (2.40)$$

It is assumed that the amplitude of the transmitted wave after 1st scatter drops so much that further propagation can be approximated to be linear. Signals from class I and class II reverberations will therefore be unequal due to different nonlinear propagation distance. The effect of nonlinear propagation of the dual band complex where presented in Section (2.2.1). Signals from class II reverberation will have a high amount of pulse form distortion, together with a larger time delay (where the time delay can be both positive and negative dependent of the LF manipulation pressure). The signal from the HF imaging pulse is also expected to be weaker from class II reverberation around the fundamental band. This since accumulation of nonlinear self distortion pumps energy up into harmonics, which can be seen as an absorption.

CHAPTER 3

Making the Phantoms

This chapter documents the process of making two ultrasound phantoms. Starting with the design of the plexiglas containers followed by the procedure of creating the tissue-mimicking agar gel. The structures of the phantoms were held simple to see SURF imaging's ability to suppress 1st and 3rd order linear scattering and enhancing 1st order nonlinear scattering. Reverberation noise have the largest impact when the reverberations are strong while 1st order scattering are weak. Therefore reverberations from fatty layers within the body wall, which can have strong specular scattering, may stand for the dominating reverberation noise. To copy this structure both phantoms were made with plane plastic layer(s) to produce reverberation noise on top of nonlinear scatters from steel wires and micro calcium particles.
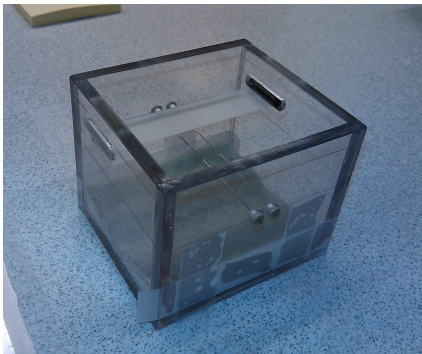
(a) *Phantom A container*   (b) *Phantom A final*
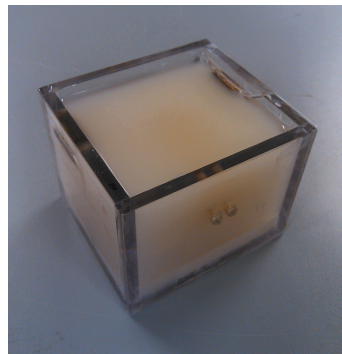
Figure 3.1

3.1 Design of the plexiglass containers

To be able to measure the effect of reverberation noise masking signals from nonlinear scatters in a simple manner, the first phantom box, Phantom A, was designed to have a class III reverberation. The second phantom box, Phantom B, was designed to have class I and II reverberations. A plastic was used as interface to produce the reverberations.

Choice of plastic layer

Three types of plastic layers were tested in a water tank setup to produce multiple scatters. All three were from plastic sheet protectors.
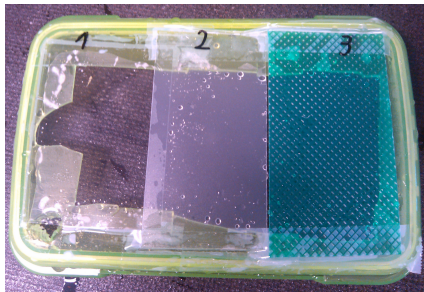
Figure 3.2: *The three types of plastic layers tested*

From Fig. (3.2): Plastic type number 1 was completely transparent and had smooth surfaces. Type number 2 had slightly uneven surfaces and was less transparent than number 1. Light was to some extent diffusely scattered. Type number 3 had the roughest surfaces, but with less diffuse scattering than number 2.

(a) *Type 1*   **(b)** *Type 2*   **(c)** *Type 3*
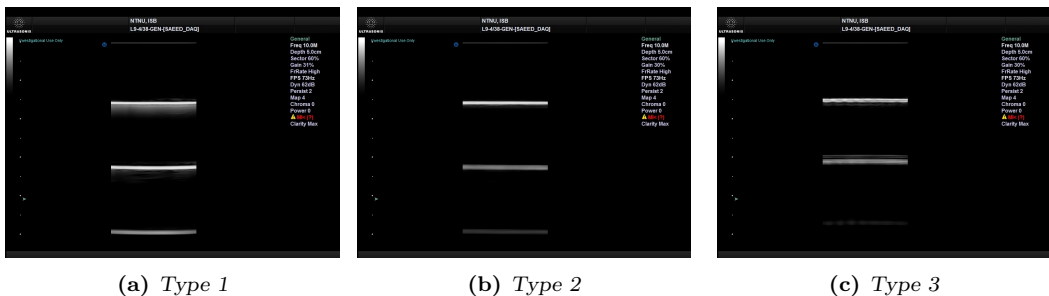
Figure 3.3: *Water tank measurements investigating the properties of the three plastic layers. To prevent standing waves/multiple scattering from the bottom of the tank a tilted glass surface was used to scatter the waves in a skew direction.*

From the water tank images all three plastic layers could represent a fatty layer within the body wall. Plastic layer number 1 seemed to have the strongest reflections by the intensity of 5th order scatters. It also has the most significant tail of weaker scatters, which is produced by multiple internal scattering within the plastic layer (or/and less possible internal

20

reflections in the transducer). The slightly uneven surfaces at the plastic layer number 2 is almost not visible in the image, and it gave the image nice reverberations. The plastic layer number 3 shows clear signs of the rough surfaces. Without any further testing plastic layer 2 was chosen to be used in the phantoms.

The thickness of plastic layer number 2 was measured with a micrometer to be 0.47mm. This is longer then the axial resolution of the SURF imaging system given by:

$$\Delta r = \frac{N_{HF} \cdot \lambda_{8MHz}}{2} = \frac{2 \cdot \lambda_{8MHz}}{2} \approx 0.2mm < 0.47mm \tag{3.1}$$

Here, N_{HF} is the number of periods in the transmitted HF imaging pulse and λ_{8MHz} is the wavelength at $8MHz$. For this reason the reflections from the front and back end of the plastic layer will be separated.

Shape of the plexiglass containers

Phantom A: The container was made with inner dimensions $80mm \times 70mm \times 67mm$ (length, width, hight) of pleixglass with thickness $5mm$. The size of the container was kept small because of the expensive Sephadex particles used in the agar gel for backscattering.
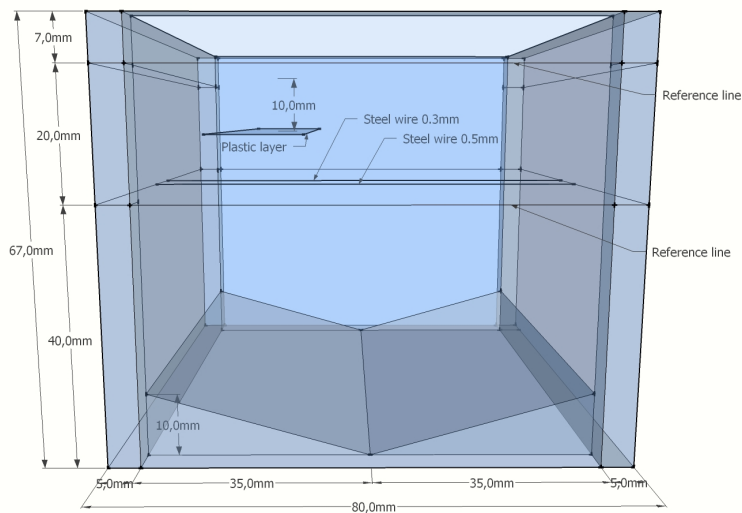
Figure 3.4: *Sketch of Phantom A*

Fig. (3.4) shows a sketch of the container drawn in Google Sketchup 8 [3]. The two reference lines were inscribed at depth $-7mm$ and $-27mm$ from the top. The lowest one was used as a reference for placing the micro calcium particles and the top reference line was used as the maximum high for the agar gel. At the same hight as the lowest reference line were also two steel wires placed with diameters $0.5mm$ and $0.3mm$. The plastic layer was placed in the middle of the two reference lines at $-17mm$ depth creating the class III reverberation.

To make it possible dropping the micro calcium particles under the plastic layer, the plastic layer was placed at the left side. This also made it possible to have one area with reverberations and one area without reverberations. The two tilted plates at the bottom were added to prevent recording reflections from the bottom of the container creating noise in the image.

Phantom B: The container for phantom B was made by the same principles as the container for phantom A. However, two plastic layers were mounted to produce the class I and II reverberations. The container was extended by increased inner width to $90mm$, since the distance between the bottom plastic layer and the position of the micro calcium particles becomes closer, making it harder placing the particles. The strength on the reverberation noise in recordings of phantom A was a little weaker than expected. Therefore the two plastic layers were not positioned symmetrically in between the two reference lines. By using water as acoustic impedance matching and recording images where the transducer was held at $-2mm$ depth, stronger reverberations could be produced due to lower attenuation in water.
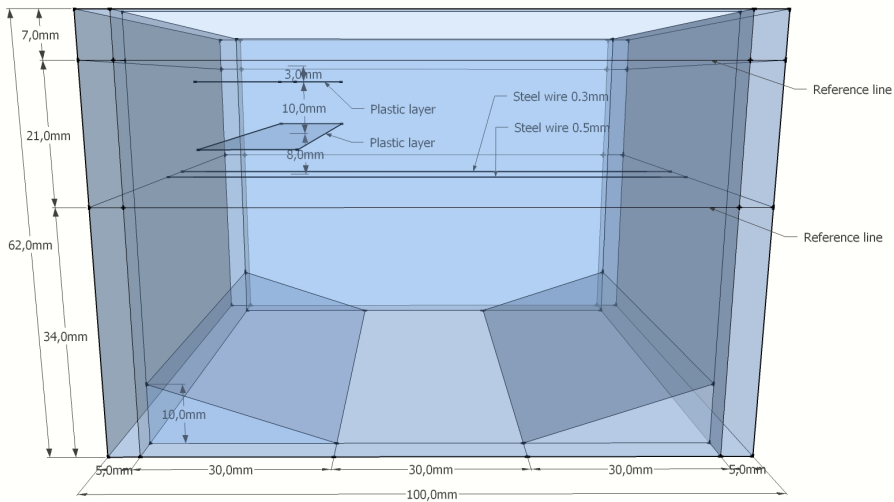

Figure 3.5: *Sketch of Phantom B*

Both phantom containers were produced at the Medical Technical Department, StOlavs hospital. All the design sketches of Phantom A and B which were sent to the Medical Technical Department can be seen in Section (B.2).

3.2 The agar-based phantom gel

The tissue-mimicking material used in phantom A and B was an agar based-gel. There are other commercially available tissue-mimicking materials such as Zerdine, condensed milk-based gel and urethane rubber-based gel, but it is only the agar-based gel that has a linear frequency dependent attenuation within the medical US frequency range [7]. The attenuation coefficient should be between 0.4 - 0.7 dB/MHz/cm and the speed of sound should be around 1460-1640 m/s. To tune the speed of sound in the agar based gel three substances can be added: Ethanol, n-propanol and glycerol. Glycerol was chosen in this case, since it has a higher boiling point. Common for all the different types of tissue mimicking materials is that they have a low acoustic backscattering coefficient. To adjust the level of backscattering, particles as chalk, tale, graphite, carbon, silicium carbide and Sephadex can be added [7]. The method followed to make Phantom A and B was found in [7] (type phantom A2).

Chemicals used to make the phantoms

The list of chemicals used to make both phantoms A and B:

- Agar

- Sephadex with bead size 20-80 μm.

- Glycerol

- Benzoic acid

- Distilled water

- Calcium particles of size 190 μm

The Agar was the base substance, making the gel adequate for tissue-mimicking. It also has low attenuation besides being robust to temperature and humidity variations. The Sephadex particles gave homogeneous backscattering. The glycerol were used to give correct speed of sound. To prevent bacterial growth Benzoic acid was added. The calcium particles were the nonlinear scattering targets, and the distilled water made up the total volume.

Procedure to make all phantoms

A detailed description of the process of making the phantom gel is found in App. (B). Below in Fig. (3.6) is a flow chart of the main steps.
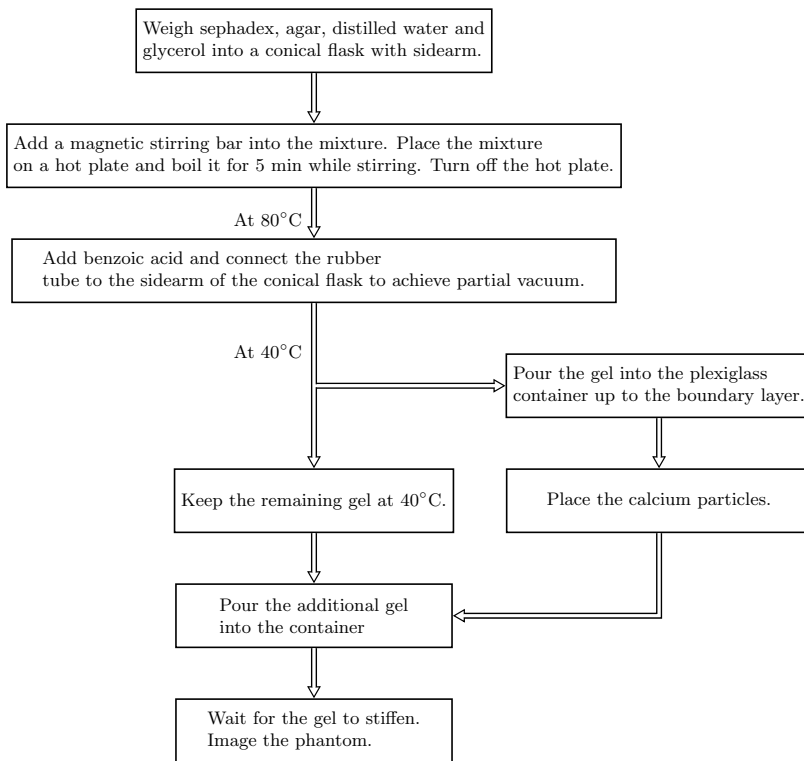
```
┌─────────────────────────────────────────────┐
│ Weigh sephadex, agar, distilled water and    │
│ glycerol into a conical flask with sidearm.  │
└─────────────────────────────────────────────┘
                      │
                      ▼
┌──────────────────────────────────────────────────────┐
│ Add a magnetic stirring bar into the mixture. Place the mixture │
│ on a hot plate and boil it for 5 min while stirring. Turn off the hot plate. │
└──────────────────────────────────────────────────────┘
           At 80°C  │
                    ▼
┌──────────────────────────────────────────────────────┐
│ Add benzoic acid and connect the rubber                │
│ tube to the sidearm of the conical flask to achieve partial vacuum. │
└──────────────────────────────────────────────────────┘

           At 40°C  │
                    │───────────────────────►┌──────────────────────────────┐
                    │                         │ Pour the gel into the plexiglass │
                    │                         │ container up to the boundary layer. │
                    │                         └──────────────────────────────┘
                    ▼                                       │
┌──────────────────────────────┐          ┌──────────────────────────────┐
│ Keep the remaining gel at 40°C. │          │   Place the calcium particles.  │
└──────────────────────────────┘          └──────────────────────────────┘
                    │                                       │
                    ▼                                       │
┌──────────────────────────────┐                           │
│      Pour the additional gel    │◄──────────────────────────┘
│      into the container         │
└──────────────────────────────┘
                    │
                    ▼
┌──────────────────────────────┐
│    Wait for the gel to stiffen. │
│    Image the phantom.           │
└──────────────────────────────┘
```

Figure 3.6: *The main steps of making an agar based phantom gel*

CHAPTER 4

The dual-band ultrasound system

SURF technology [4] has modified a Ultrasonix SonixMDP scanner with the possibility to connect to an additional amplifier for exciting the LF pulses. The amplifier can drive 128 LF channels, and it is connected through a new probe-connector board supporting the extra channels. The Sonix GUI interface is also updated for adjusting SURF parameters. Along with the extended system, new dual-band ultrasound transducers have been developed.

Figure 4.1: *SURF imaging system*

4.1 The dual-band transducer, VORA II

The transducer used for imaging the phantoms is called VORA II and it is a linear array transducer. VORA II is designed for carotid, breast and thyroid imaging.

Table 4.1: *General specifications, VORA II*

		HF	LF
Center frequency	f_c	$8MHz$	$0.8MHz$
Number of active elements azimuth	N_{Az}	128	58
Number of active elements elevation	N_{El}	1	1
Total elevation element width	El	$4.0mm$	$8.0mm$
Elevation lens focus		$20mm$	-
Azimuth element pitch	p	$300\mu m$	$900\mu m$
Maximum azimuth width	Az	$38.4mm$	$46.8mm$

The dual-band transducer stack design

The transducer stack design for VORA II differs from conventional US transducers by having two piezoelectric layers stacked behind each other. The first piezoelectric layer is $\lambda_{HF}/2$ thick achieving resonance at $8MHz$. Equivalent is the $0.8MHz$ resonance obtained by the second piezoelectric layer with thickness $\lambda_{LF}/2$. An illustration of the transducer stack is in Fig. (4.4).

One dimensional analysis of the transducer stack has been done with Xtrans. Xtrans is a simulation tool using an iterative scheme for computing the electric to acoustic transfer functions and the corresponding electrical input admittances for each par of electrodes, see App. (A.2). Important stack parameters are the thicknesses and the characteristic acoustic impedances of the layers. Piezoelectric composites have typical a characteristic impedance around $20MRayl$. However, the characteristic impedance for tissue is close to $1.5MRayl$ which corresponds to a large impedance mismatch. For this reason, two quarter wave ($\lambda_{HF}/4$) transformers are placed in front of the HF piezoelectric layer. The characteristic impedances of the two quarter wave transformers are chosen such that the HF layer achieves largest bandwidth. Backward the HF layer sees an isolation layer, the isolation layer should keep the high frequencies from the HF layer to travel and interfere with the LF layer. Choosing an isolation layer with thickness $\lambda_{HF}/4$ and low characteristic

impedance ($< 2MRayl$) has shown to perform well as isolation. However, a strong reflection between the HF layer and the isolation layer makes the HF layer ring longer. Normally the HF layer would see the backing which could have a more matched impedance. The backing would then dissipate more of the energy reducing the ringing. Having less isolation between the HF and LF layers has shown to produce ripple in the HF band [2]. The LF layer see the complete stack of layers in front as matching layers, and therefore the LF layer does not have as width relative bandwidth as the HF layer. The bandwidth of the HF layer is of great importance since the axial resolution of the image is fixed by the length of the HF pulse. On the other hand, a large bandwidth of the LF layer is not that critical because ideally the LF frequencies will be filtered out in receive.

A transducer stack for VORA II was proposed in the design rapport [2], see Table (4.2). (The final transducer design and manufacturing was done by Vermon, Tours, France [6], and is therefore not known to SURF technology.)

Table 4.2: *Xtrans model used for stack simulations, VORA II*

Symbols	h $V/m \cdot 10^8$	ϵ rel. ϵ_0	Z $(MRayl)$	c (m/s)	Q	l (μm)	A (mm^2)
Backing			5.0				
Electrode			44.5	4800	50	1	
LF piezo	15.1	1110	17.8	3630	30	1924	7.2
Electrode			44.5	4800	50	1	
Isolation			1.8	2200	30	69	
Electrode			44.5	4800	50	1	
HF piezo	13.7	1440	18.7	3810	30	203	1.2
Electrode			44.5	4800	50	1	
Matching 1			5.3	2600	30	81	
Matching 2			2.0	1800	30	56	

Using the values from Table (4.2) the electric to acoustic transfer functions and the electric impedances for the HF and LF layers have been computed using Xtrans. (The computation has been done with shorted electrodes, meaning while exciting the HF electrodes the LF electrodes are kept shorted and vice versa).
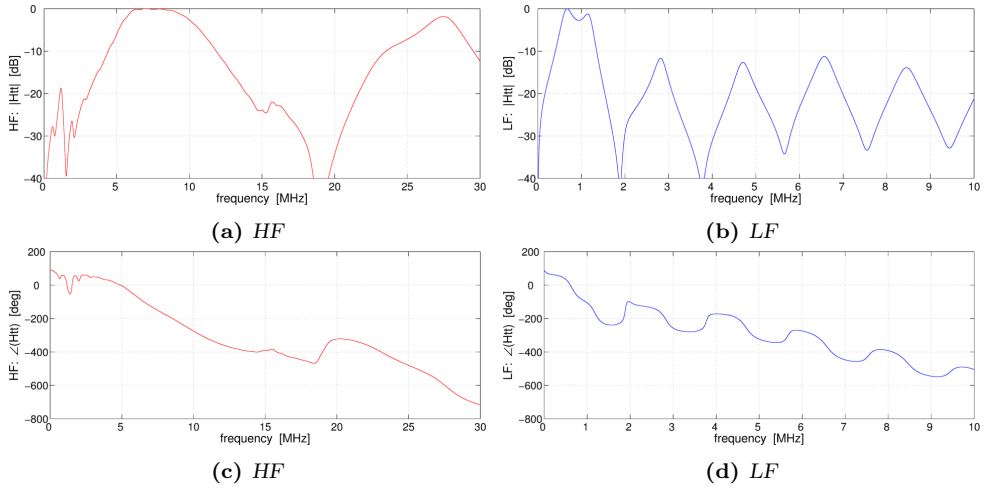
(a) *HF* **(b)** *LF*

(c) *HF* **(d)** *LF*

Figure 4.2: *Xtrans simulation of the electric to acoustic transfer functions for VORA II*

(a) *HF* **(b)** *LF*

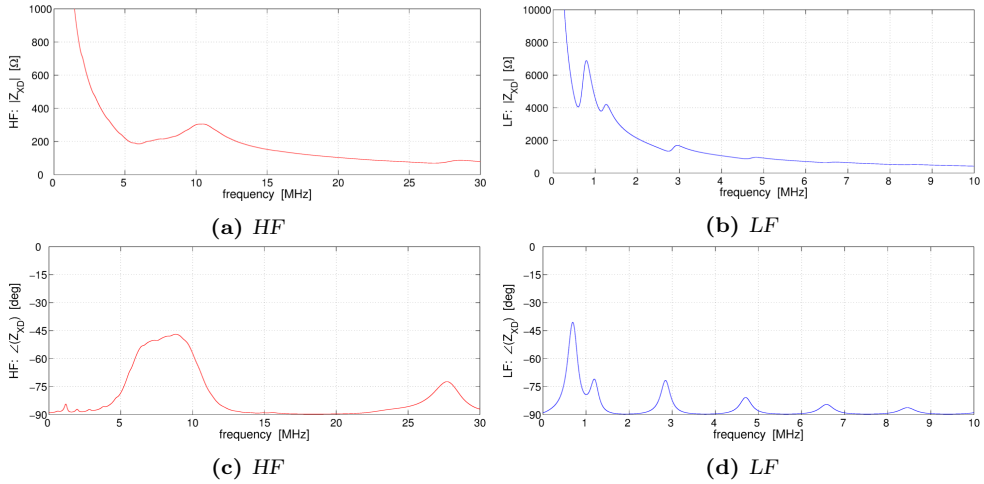**(c)** *HF* **(d)** *LF*

Figure 4.3: *Xtrans simulation of the electrical impedances for VORA II*

Fig. (4.2a) and Fig. (4.2b) shows that the dual piezoelectric stack is capable of transmitting frequencies around the $f_{c,HF}$ and $f_{c,LF}$, and that both the transfer functions have high efficiency for all odd harmonics.
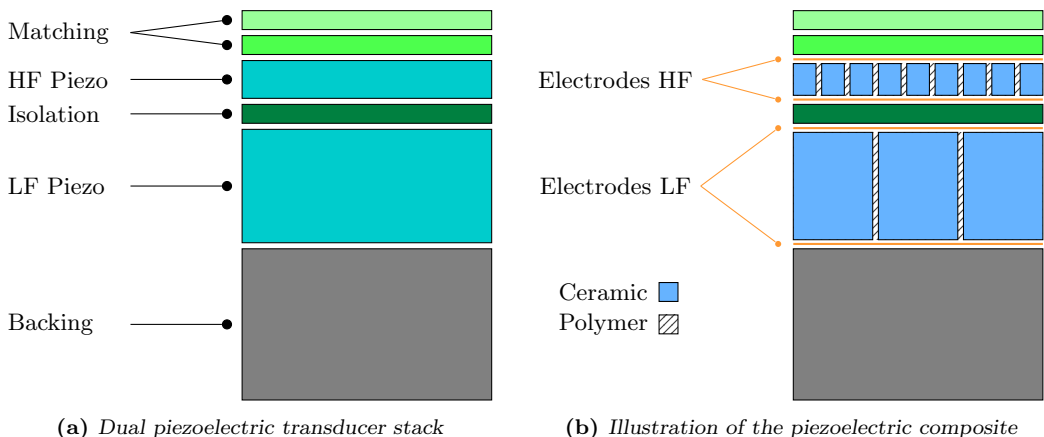
(a) *Dual piezoelectric transducer stack*

(b) *Illustration of the piezoelectric composite*

Figure 4.4: *VORA II stack design*

The SURF pulse complex

Ultrasound pulses can be modeled as a fast varying cosine with a Gaussian or a slower varying cosine as envelope. In ForwardSIM App. (A.1) is the default pulse modeled as:

$$p(t) = P_0 \, cos(2\pi f_c t) \, e^{-\left(\frac{2f_c}{N_p}t\right)^2} \tag{4.1}$$

P_0 is the maximal surface pressure, f_c is the center frequency and N_p is the number of periods. For having a more accurate model of the SURF pulse complex the HF and LF pulses is now created with its electric to acoustic transfer functions (H_{tt}). By the amplifier designs the SonixMDP scanner and the LF amplifier are only capable of transmitting squared waves. These waves are filtered by transmit electronics, the connector and the cable before exciting the electrodes of the piezoelectric layers. The LF and HF pulses can for example be modeled for three types of electrode excitations:

Model I - Pure squared wave excitation

Model II - Filtered squared wave excitation

Model III - Pure sine wave excitation

Model III is only possible with a linear amplifier. The chain from the voltage generator to the surface pressure is in the temporal frequency domain written as:

$$P(\omega) = V_g(\omega)H_{ti}(\omega)H_{tt}(\omega) \tag{4.2}$$

The voltage generation either in the SonixMDP amplifier or the LF amplifier is noted as $V_g(\omega)$. The transfer function to the transmit electronics, connector and the cable is $H_{ti}(\omega)$, and $H_{tt}(\omega)$ is again the transducer electric to acoustic transfer function.

From recordings of phantom A, it has been observed unexpected nonlinear propagation time delay estimates around strong scatters. It is thought that it originates from frequency components in the HF band within the LF pulse. For this reason the frequency content in model I, II and III will be investigated for the LF pulse.

Model I: The figure below shows the frequency content for squared waves with various length.
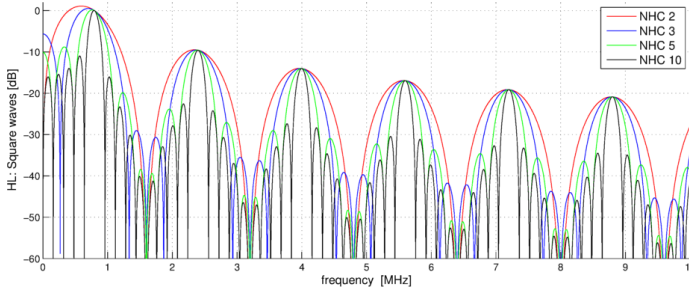

Figure 4.5: *Model I - The frequency content of square waves with excitation frequency 0.8Mhz and with length X number of half cycles (NHC). The graphs have been normalized with respect to the magnitude at 0.8MHz.*

The fourth and fifth harmonics which is in the HF band has dropped $\sim 20dB$. To calculate the final pulses and their frequency spectra $H_{ti}(\omega)$ is set to one in Eq. (4.2).
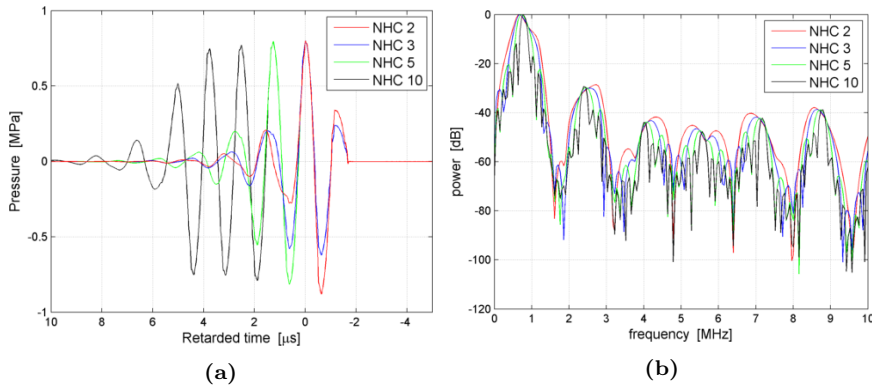

Figure 4.6: *Model I - (a) normalized pulses of different length and (b) the corresponding frequency spectra.*

Fig. (4.6b) shows that the energy within the HF band is $-40dB$, it also indicates that exciting the LF layer with longer pulses does not reduce the relative energy within the HF band.

Model II: The transmit electronics, connector and the cable will be approximated to only the cable with a series inductor located at the connector. The coil was added for tunning the

30

cables resonance frequency to match the LF center frequency [2]. The cable is represented by a lossless transmission line.
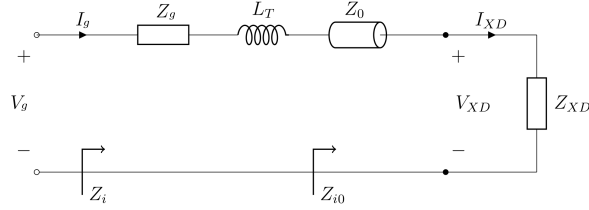

Figure 4.7: *The cable model: A transmission line with a series inductor. Taken from [11]*

L_T is the inductor inductance, giving an impedance $Z_t = i\omega L_T$. The cable characteristic electrical impedance is noted as Z_0, Z_g is the generator voltage output impedance and Z_{XD} is the impedance of one transducer element. The lossless transmission line input impedance, Z_{i0}, can be calculated by the impedance transformation formula

$$Z_{i0} = Z_0 \frac{Z_{XD}\, cos(kL) + iZ_0\, sin(kL)}{Z_0\, cos(kL) + iZ_{XD}\, sin(kL)} \tag{4.3}$$

where k is the wavenumber and L is the cable length. The voltage, V_{XD}, over the piezo-electric electrodes can be expressed by the applied voltage V_g and the currents I_g, I_{XD} in matrix form [11].

$$\begin{bmatrix} V_g \\ I_g \end{bmatrix} = \begin{bmatrix} 1 & Z_g + Zt \\ 0 & 1 \end{bmatrix} \begin{bmatrix} cos(kL) & iZ_0 sin(kL) \\ i\frac{1}{Z_0} sin(kL) & cos(kL) \end{bmatrix} \begin{bmatrix} V_{XD} \\ I_{XD} \end{bmatrix} \tag{4.4}$$

Further by using ohm's law

$$V_g = I_g \cdot Z_i \tag{4.5}$$

Eq. (4.4) can by rearranged to a voltage transfer function form V_g to V_{XD}.

$$H_{ti} = \left(1 - \frac{Z_g + Z_t}{Z_i}\right) cos(kL) - i\frac{Z_0}{Z_i} sin(kL) \tag{4.6}$$

To calculate H_{ti} was Z_i found by

$$Z_i = Z_g + Z_t + Z_{i0} \tag{4.7}$$

and the parameters used is shown in the table below:

Table 4.3: *Parameters for the lossless transmission line model.*

Cable impedance (Z_0)	75 [Ω]
Cable length (L)	2 [m]
Cable capacitance (Cc)	60 [pF/m]
Coil inductance (L_t)	270 [μH]
Voltage gen. output impedance (Z_g)	50 Ω
Cable wave propagation speed (c)	$2.2 \cdot 10^8$ [m/s]

None of the listed parameters were known, but realistic values has been chosen. The cable capacitance for a similar transducer cable has been measured to $60pF/m$. The velocity factor for coaxial cables is typically around 0.7. Also common values for cables characteristic impedance are 50Ω, 75Ω and 95Ω [5]. Of them 75Ω was chosen to match the velocity factor, since the signal velocity is given by

$$c = \frac{1}{Cc\, Z_0} \tag{4.8}$$

The inductance of the added inductor was picked so it tunned out the reactance of Z_{i0} at the LF center frequency. H_{ti} was thus calculated.
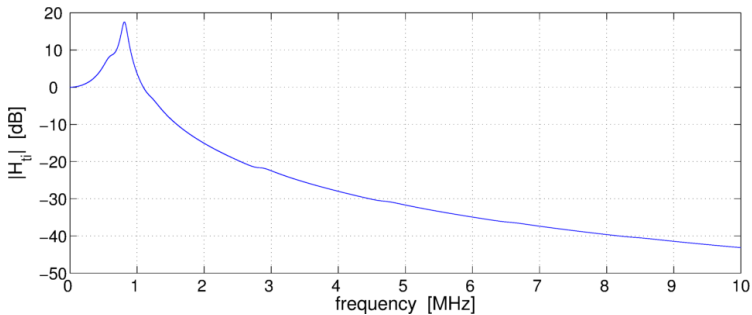

Figure 4.8: *The voltage transfer function H_{ti}.*

Fig. (4.8) indicates that the cable acts as a sharp bandpass filter, but this can not be completely true since it would make it impossible transmitting "short" LF pulses. For an adequate model of the cable system, losses needs to be taken into account. However, the analysis demonstrate that frequencies in the HF band of the LF pulse will be further reduced, although the specific amount is unknown.

Model III: As for the squared waves in Fig. (4.5) the frequency content for sine waves with different length can be calculated.
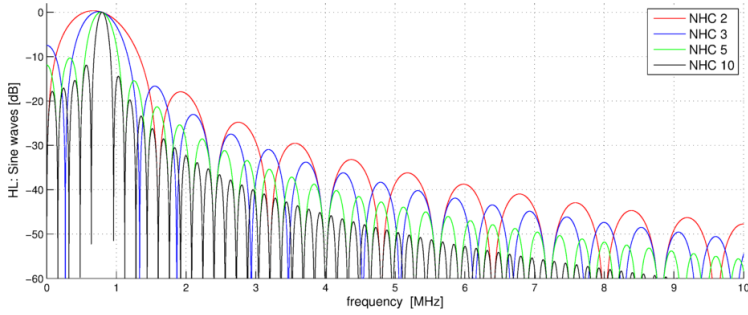
Figure 4.9: *The frequency content of sine waves with excitation frequency 0.8Mhz and with length X number of half cycles (NHC). The graphs have been normalized with respect to the magnitude at 0.8MHz.*

With the use of a linear amplifier is it possible to reduce the energy within the HF band of the LF pulse. The relative energy within the HF band also reduces with longer pulses, and can be even further reduced be applying a windows such as Hanning/Hamming. For a LF pulse of 3 half cycles the relative energy has dropped $\sim 25dB$ compared to square wave excitation.

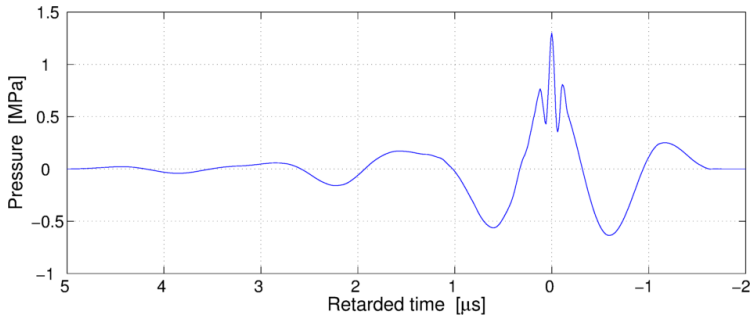An example of a SURF pulse complex for VORA II is shown in the figure below (Model III).

Figure 4.10: *Simulated VORA II SURF pulse complex*

CHAPTER 5

SURF signal processing

The first part of this chapter contains the derivation of the received signal model Eq. (5.1) [15]. After that a phase based estimation method is introduced for calculating the nonlinear propagation time delay (τ).

The received backscattered signal from a SURF pulse complex is bandpass filtered around the HF center frequency. This is done to remove interfering frequency components from the LF pulse together with removing harmonic frequency components of the HF pulse. The received bandpass filtered signal can then be expressed as [15].

$$Y(\underline{r},\omega,p) = \left\{ X_l(\underline{r},\omega) + pX_n(\underline{r},\omega) \right\} \tilde{V}_p(\underline{r},\omega,p) e^{i\omega p\tau(\underline{r})} \; + \; \tilde{N}(\underline{r},\omega,p) e^{i\omega p\tau_n(\underline{r})}$$

$$Y(\underline{r},\omega,0) = X_l(\underline{r},\omega)V_p(\underline{r},\omega,0) + \tilde{N}(\underline{r},\omega,0) \tag{5.1}$$

$$Y(\underline{r},\omega,-p) = \left\{ X_l(\underline{r},\omega) - pX_n(\underline{r},\omega) \right\} \tilde{V}_p(\underline{r},\omega,-p) e^{-i\omega p\tau(\underline{r})} + \tilde{N}(\underline{r},\omega,-p) e^{-i\omega p\tau_n(\underline{r})}$$

for Plus, Zero and Minus LF manipulation pressure. The magnitude of the transmitted LF pressure is noted as p. X_l and X_n are the signals from linear and nonlinear scattering respectively. All the nonlinear propagation effects are included in $\tilde{V}_p$, besides the nonlinear propagation time delay, τ, produced by the LF pressure. The noise, $\tilde{N}$, is considered to mainly consist of reverberation noise and the effect of the LF pressure is among others a combined phase change, τ_n, for all the reflections.

5.1 Signal models

This section contains the underlaying mathematics for the SURF signal model Eq. (5.1), which is used to interpret the received signal from the transmitted SURF pulse complex.

The SURF signal model is first derived with linear acoustics for 1st order scattering. Then the model is modified to describe nonlinear effects as nonlinear propagation and nonlinear scattering. The signal model for 3rd order scattering is derived and interpreted as noise in the last two sections. The signal model will be written in the temporal frequency domain [15].
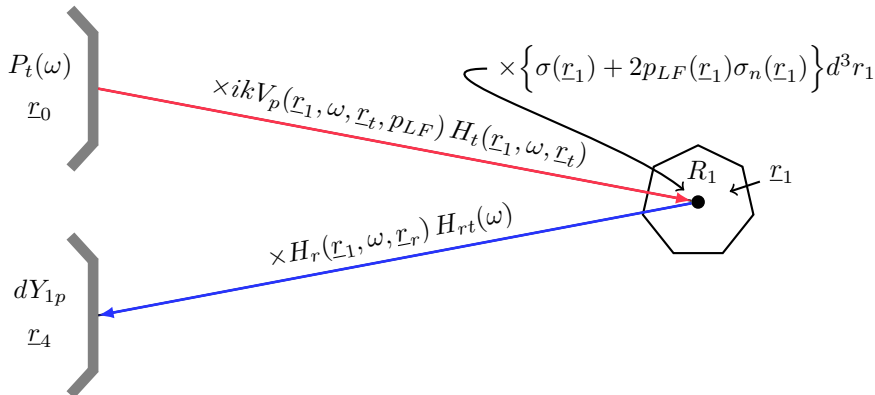

Figure 5.1: *Visualization of the signal model for 1st order scattering with nonlinear interactions. The transmitted pulse given by P_t propagate nonlinearly indicated by the red line up to the 1st scatter. The pulse is then scattered by a infinitesimal volume element $d^3 r_1$ within the resolution of the image system R_1. The backward propagating wave is approximated to propagate linearly indicated by the blue line. The transmit and receiver transducers are often the same.*

Signal model for 1st order scattering within linear acoustics

The produced pressure at position $\underline{r}_1$ is described by $P_t(\underline{r}_1, \omega, \underline{r}_t)$, where $\underline{r}_t$ is the transmit focal point. $P_t(\underline{r}_1, \omega, \underline{r}_t)$ is given by the transducer surface vibration, $P_t(\omega)$, written in the temporal frequency domain and the transfer function $ik H_t(\underline{r}_1, \omega, \underline{r}_t)$.

$$P_t(\underline{r}_1, \omega, \underline{r}_t) = P_t(\omega) \, ik \, H_t(\underline{r}_1, \omega, \underline{r}_t) \tag{5.2}$$

$$H_t(\underline{r}_1, \omega, \underline{r}_t) = \int_{S_t} d^2 \underline{r}_0 \, 2G(\underline{r}_1, \underline{r}_0, \omega) \, e^{-i\omega \tau_t(\underline{r}_0, \underline{r}_t)} \, w_t(\underline{r}_0) \, H_{abc}(\underline{r}_0, \omega, \underline{r}_t) \tag{5.3}$$

$$c \, \tau_t(\underline{r}_0, \underline{r}_t) = \underline{r}_t - |\underline{r}_0 - \underline{r}_t| \tag{5.4}$$

Here is S_t the transducer surface, ω has the relation $\omega = kc$, where k is the wave number and c is the speed of sound. H_{abc} is an aberration function, which can correct for spatial variations in propagation velocity, although estimation of an aberration filter is challenging. Apodization is applied through $w_t(\underline{r}_0)$, and can be used to reduce side lobes in expense of a wider main beam. The time delay $\tau(\underline{r}_0, \underline{r}_t)$ is what creates the focal point $\underline{r}_t$. $G(\underline{r}_1, \underline{r}_0, \omega)$ is the Greens function and for a non-absorbing homogeneous medium with pressure independent elasticity is it given in [13] as:

$$G(\underline{r}_1, \underline{r}_0, \omega) = \frac{e^{-ik|r_1-r_0|}}{4\pi|\underline{r}_1 - \underline{r}_0|} \tag{5.5}$$

The acoustic scattering density at position $\underline{r}_1$ can be model as the parameter.

$$\sigma(\underline{r}_1) = -k^2\Big(\sigma_l(\underline{r}_1) - \gamma(\underline{r}_1)\Big) \tag{5.6}$$

where σ_l is the relative spatial variation in the compressibility and γ is the relative spatial variation in the mass density, see Eq. (2.13). Similarly, to Eq. (5.3) the receive H_r is written as.

$$H_r(\underline{r}_1, \omega, \underline{r}_r) = \int_{S_r} d^2\underline{r}_4 \, 2G(\underline{r}_4, \underline{r}_1, \omega) \, e^{-i\omega\tau_r(\underline{r}_4, \underline{r}_r)} \, w_t(\underline{r}_4) \, H_{abc}(\underline{r}_4, \omega, \underline{r}_r) \tag{5.7}$$

By combining Eq. (5.2), Eq. (5.6) and Eq. (5.7) the received electrical signal from an infinitesimal volume element d^3r_1 is achieved as $dY_1(\underline{r}_1, \omega)$.

$$dY_1(\underline{r}_1, \omega) = P_t(\omega) \, ik \, H_t(\underline{r}_1, \omega, \underline{r}_t) \, \sigma(\underline{r}_1) \, H_r(\underline{r}_1, \omega, \underline{r}_r) \, H_{rt}(\omega) \, d^3r_1. \tag{5.8}$$

Here H_{rt} is the transducer acoustic to electric transfer function. The complete signal can be found by integrating $\underline{r}_1$ over the region of scatters R_1.

Signal model for 1st order scattering within nonlinear acoustic

The nonlinear propagation phenomena are all included in a filter V_p. In the signal model the backward propagating wave (after 1st scatter) is approximated to propagate linearly, since biological medias are considered to have weak scattering densities reducing the amplitude of the backward propagating wave [15]. We introduce P_{tp} as an extension of P_t in Eq. (5.2) by including V_p up to the first scatter.

$$P_{tp}(\underline{r}_1, \omega, \underline{r}_t, p_{LF}) = V_p(\underline{r}_1, \omega, \underline{r}_t, p_{LF}) \, P_t(\underline{r}_1, \omega, \underline{r}_t) \tag{5.9}$$

Together with the input arguments listed in the $V_p(\underline{r}_1, \omega, \underline{r}_t, p_{LF})$ filter, the filter is also a function of the complete setup such as LF/HF apertures, HF pressure and tissue parameters, but these independent variables are omitted since they are assumed fixed. Similar to Eq. (5.8) we can define the received signal component from linear scatters by $dY_{l1}(\underline{r}_1, \omega)$ and from nonlinear scatters by $dY_{n1}(\underline{r}_1, \omega)$.

$$dY_{l1}(\underline{r}_1, \omega, p_{LF}) = V_p(\underline{r}_1, \omega, \underline{r}_t, p_{LF}) P_t(\omega) \, ik H_t(\underline{r}_1, \omega, \underline{r}_t) \, H_r(\underline{r}_1, \omega, \underline{r}_r) \, H_{rt}(\omega) \, \sigma(\underline{r}_1) \, d^3r_1.$$
$$dY_{n1}(\underline{r}_1, \omega, p_{LF}) = V_p(\underline{r}_1, \omega, \underline{r}_t, p_{LF}) P_t(\omega) \, ik H_t(\underline{r}_1, \omega, \underline{r}_t) \, H_r(\underline{r}_1, \omega, \underline{r}_r)$$
$$H_{rt}(\omega) \, 2\sigma_n(\underline{r}) p_{LF}(\underline{r}, t) \, d^3r_1. \tag{5.10}$$

The scattering density of the nonlinear scatters are in compliance with Eq. (2.39), and the total received signal dY_{1p} will be the sum of dY_{l1} and dY_{n1}. Finally the total receive signal (dY_{1p}) is written in the form below to clarify the interaction with the LF pulse.

37

$$dY_{1p}(\underline{r}_1, \omega, p_{LF}) = V_p(\underline{r}_1, \omega, \underline{r}_t, p_{LF})\Big\{ dX_l(\underline{r}_1, \omega) + p_{LF}(\underline{r}_1)\, dX_n(\underline{r}_1, \omega) \Big\} \qquad (5.11)$$

$$dX_l(\underline{r}_1, \omega) = P_t(\omega)\, ik\, H_t(\underline{r}_1, \omega, \underline{r}_t)\, H_r(\underline{r}_1, \omega, \underline{r}_r)\, H_{rt}\, \sigma(\underline{r}_1)\, d^3 r_1$$
$$dX_n(\underline{r}_1, \omega) = P_t(\omega)\, ik\, H_t(\underline{r}_1, \omega, \underline{r}_t)\, H_r(\underline{r}_1, \omega, \underline{r}_r)\, H_{rt}\, 2\sigma_n(\underline{r})\, d^3 r_1$$
$$\qquad (5.12)$$

Observation from Eq. (5.11):

- The polarity of the nonlinear scatter follows the polarity of the LF pressure.

- The received signal dY_{1p} is effected by nonlinear propagation time delay, pulse form distortion (PFD) and pulse form modification (PFM) through the filter V_p.

- The filter V_p is different for linear and nonlinear scatters in the case of strong resonant nonlinear scatters as for micro bubbles, but for stiff particles as micro calcification an approximation of equal V_p is adequate [15].

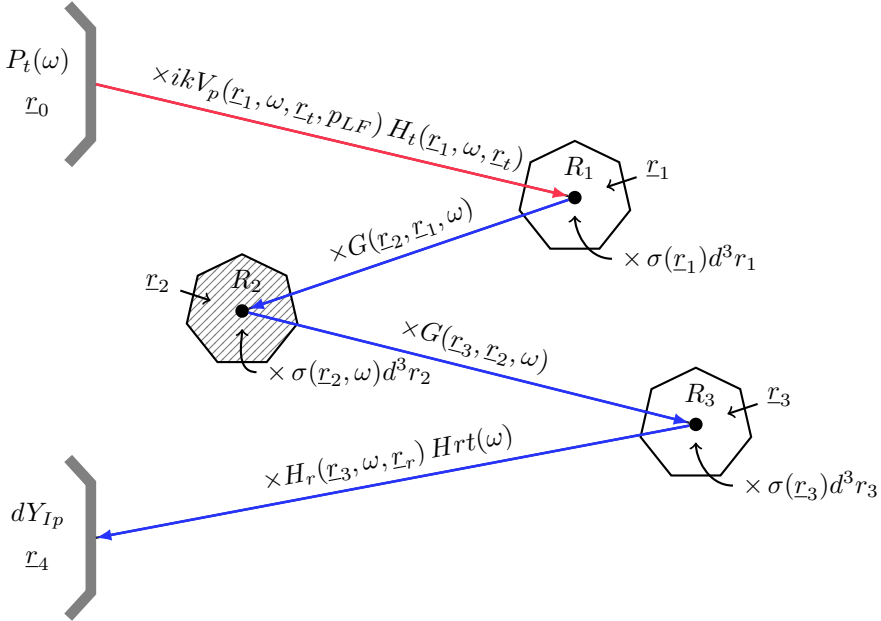**Signal model for 3rd order scattering within linear acoustics**

Figure 5.2: *Visualization of the signal model for class I 3rd order scattering with nonlinear interactions. The propagating wave is approximated to propagate linearly after the first scatter due to loss in amplitude. The nonlinear scattering component is omitted since only strong 3rd order signals are visible artifacts. The pattern of skew lines across the region R_2 indicates it has been integrated across.*

There are also received signal components from waves which have been scattered multiple times before ending at the receive transducer. The signal model for 3rd order scattering is an extension of the 1st order scattering model, and the additional propagation is included in H_{rev} ($H_{reverberation}$).

$$H_{rev}(\underline{r}_3, \underline{r}_1, \omega) = \int_{R_2} d^3 r_2 \, G(\underline{r}_3, \underline{r}_2, \omega) \, G(\underline{r}_2, \underline{r}_1, \omega) \, \sigma(\underline{r}_2, \omega) \tag{5.13}$$

To include the possibility of R_2 being the transducer $\sigma(\underline{r}_2, \omega)$ is set to be a function of ω. The received signal from 3rd order scatters is written as:

$$dY_3(\underline{r}_1, \underline{r}_3, \omega) = P_t(\omega) ik H_t(\underline{r}_1, \omega, \underline{r}_t) \sigma(\underline{r}_1) H_{rev}(\underline{r}_3, \underline{r}_1, \omega)$$
$$H_r(\underline{r}_3, \omega, \underline{r}_r) \sigma(\underline{r}_3) \, H_{rt} \, d^3 r_1 d^3 r_3 \tag{5.14}$$

Signals from both $dY_3(\underline{r}_1, \underline{r}_3, \omega)$ and $dY_3(\underline{r}_3, \underline{r}_1, \omega)$ occurs at the same time, and from Fig. (2.7) Class I and Class II reverberations are defined by:

$$dY_I(\underline{r}_1, \underline{r}_3, \omega) = dY_3(\underline{r}_1, \underline{r}_3, \omega)$$
$$dY_{II}(\underline{r}_1, \underline{r}_3, \omega) = dY_3(\underline{r}_3, \underline{r}_1, \omega) \tag{5.15}$$

The total received signal from for 3rd order scattering is the sum of class I and class II reverberations and it requires integration of $\underline{r}_1$ and $\underline{r}_3$ across R_1 and R_3.

Signal model for 3rd order scattering within nonlinear acoustic

The signal model for 3rd order scattering within nonlinear acoustic is an extension to the 3rd order scattering model for linear acoustic the same way as for 1st order scattering. We add the V_p filter up to 1st scatter, where the amplitude drops such that further prorogation is assumed linear. The received 3rd order scattered signal dY_{3p} is the sum of the reverberation classes I and II.

$$dY_{3p}(\underline{r}_1, \underline{r}_3, \omega, p_{LF}) = dY_{Ip}(\underline{r}_1, \underline{r}_3, \omega, p_{LF}) + dY_{IIp}(\underline{r}_1, \underline{r}_3, \omega, p_{LF}) \tag{5.16}$$

$$dY_{Ip}(\underline{r}_1, \underline{r}_3, \omega, p_{LF}) = V_p(\underline{r}_1, \omega, \underline{r}_t, p_{LF}) \, dY_I(\underline{r}_1, \underline{r}_3, \omega)$$
$$dY_{IIp}(\underline{r}_1, \underline{r}_3, \omega, p_{LF}) = V_p(\underline{r}_3, \omega, \underline{r}_t, p_{LF}) \, dY_{II}(\underline{r}_1, \underline{r}_3, \omega) \tag{5.17}$$

The signals from class I and class II reverberations are not received at exactly the same time for a SURF pulse complex although distance travelled is equal. This time difference is the difference in the nonlinear propagation time delay between $V_p(\underline{r}_1, \omega, \underline{r}_t, p_{LF})$ and $V_p(\underline{r}_3, \omega, \underline{r}_t, p_{LF})$, and is for a linear time delay curve proportional to the difference in path length up to 1st scatter. The difference in path length Δr is given by.

$$\Delta r = |\underline{r}_3 - \underline{r}_0| - |\underline{r}_1 - \underline{r}_0| \tag{5.18}$$

The signals from class I and II also vary due to nonlinear pulse form distortion, nonlinear pulse form modification and nonlinear self distortion. The nonlinear self distortion can be viewed as a nonlinear attenuation, since energy is transfered into harmonics. For further investigation of the received 3rd order scattered signal dY_{3p} is expanded and written in term of dY_{II}.

$$dY_{3p}(\underline{r}_1, \underline{r}_3, \omega, p_{LF}) = K_p(\omega, \underline{r}_1, \underline{r}_3, p_{LF})\, dY_{II}(\underline{r}_1, \underline{r}_3, \omega) \tag{5.19}$$

$$K_p(\omega, \underline{r}_1, \underline{r}_3, p_{LF}) = V_p(\underline{r}_3, \omega, \underline{r}_t, p_{LF}) + V_p(\underline{r}_1, \omega, \underline{r}_t, p_{LF})Q(\omega, \underline{r}_1, \underline{r}_3) \tag{5.20}$$

$$Q(\omega, \underline{r}_1, \underline{r}_3) = \frac{H_t(\underline{r}_1, \omega, \underline{r}_t)H_r(\underline{r}_3, \omega, \underline{r}_t)}{H_t(\underline{r}_3, \omega, \underline{r}_t)H_r(\underline{r}_1, \omega, \underline{r}_t)} \tag{5.21}$$

The received signal dY_{3p} from 3rd order scatters is hence a filtered version of the linear class II reverberation dY_{II}, and the difference in class I and class II reverberation is described though $Q(\omega, \underline{r}_1, \underline{r}_3)$ for linear acoustics.

Interpretation of the received signal model

The received signal model Eq. (5.1) is an addition of Eq. (5.11) with multiple combinations of Eq. (5.19)

$$Y(\underline{r}, \omega, p_{LF}) = dY_{1p}(\underline{r}, \omega, p_{LF}) + \sum_i dY_{3p}(\underline{r}_{1i}, \underline{r}_{3i}, \omega, p_{LF}) \tag{5.22}$$

where all combinations satisfy:

$$\underline{r} = \underline{r}_{1i} + \underline{r}_{3i} - \underline{r}_{2i} \tag{5.23}$$

The noise, N, is assumed to only originate from reverberation noise and is hence written as the 3rd order scattering term.

$$N(\underline{r}, \omega, p_{LF}) = \tilde{N}(\underline{r}, \omega, p_{LF})e^{i\omega p_{LF}\tau_n(\underline{r})} = \sum_i dY_{3p}(\underline{r}_{1i}, \underline{r}_{3i}, \omega, p_{LF}) \tag{5.24}$$

Since the magnitude and the phase of the LF pulse affects the interference between the class I and class II reverberations, suppression of reverberation noise is challenging. In order to investigate the change in interference it is practical to extract the nonlinear propagation time delay for both the classes. Eq. (5.20) then takes the form:

$$\begin{aligned} K_p(\omega, \underline{r}_1, \underline{r}_3, p_{LF}) = \tilde{V}_p(\underline{r}_3, \omega, \underline{r}_t, p_{LF})e^{i\omega p_{LF}\tau(\underline{r}_3)} \\ + \tilde{V}_p(\underline{r}_1, \omega, \underline{r}_t, p_{LF})e^{i\omega p_{LF}\tau(\underline{r}_1)}\, Q(\omega, \underline{r}_1, \underline{r}_3) \end{aligned} \tag{5.25}$$

Further, a common time delay for both classes can be extracted, which it is also possible to correct for.

$$K_p(\omega, \underline{r}_1, \underline{r}_3, p_{LF}) = e^{i\omega p_{LF}\{\tau(\underline{r}_1) + \tau(\underline{r}_3)\}/2} \, \tilde{K}_p(\omega, \underline{r}_1, \underline{r}_3, p_{LF}) \tag{5.26}$$

Here $\tilde{K}_p$ is:

$$\begin{aligned}
\tilde{K}_p(\omega, \underline{r}_1, \underline{r}_3, p_{LF}) &= \tilde{V}_p(\underline{r}_3, \omega, \underline{r}_t, p_{LF}) e^{i\omega p_{LF}\{\tau(\underline{r}_3) - \tau(\underline{r}_1)\}/2} \\
&+ \tilde{V}_p(\underline{r}_1, \omega, \underline{r}_t, p_{LF}) e^{-i\omega p_{LF}\{\tau(\underline{r}_3) - \tau(\underline{r}_1)\}/2} \, Q(\omega, \underline{r}_1, \underline{r}_3)
\end{aligned} \tag{5.27}$$

In the simplified situation where the LF manipulation pressure only produces a time delay and the reverberations noise only consist of class III reverberation ($Q = \tilde{V}_p = 1$) $\tilde{K}_p$ can be rewritten as:

$$\tilde{K}_p(\omega, \underline{r}_1, \underline{r}_3, p_{LF}) = 2cos\left\{\frac{\omega \, p_{LF}}{2}\left(\tau(\underline{r}_3) - \tau(\underline{r}_1)\right)\right\} \tag{5.28}$$

In this case $\tilde{K}_p$ becomes independent of the polarity of the LF pressure. Q equal one can be obtained by synthetic transmit and receive beams, and in the special case of plane reflectors while using a fixed receive focus [15]. $\tilde{V}_p = 1$ can never be achieved because of different self distortion for class I and class II reverberations, but $\tilde{V}_p$ close to one can be obtained by careful design of the transmit setup.

The combined time delay of the signal from class I and II reverberations given by the exponent in Eq. (5.26), can generally not be calculated since the positions to the reverberations $\underline{r}_1$ and $\underline{r}_3$ are unknown. For the special case of linear time delay development and the transducer as the 2nd scatter the combined time delay can however be calculated.

$$\tau(\underline{r}) = a\,\underline{r}, \qquad\qquad \underline{r} = \underline{r}_1 + \underline{r}_3 \tag{5.29}$$

$$\frac{\tau(\underline{r}_1) + \tau(\underline{r}_3)}{2} = \frac{a(\underline{r} - \underline{r}_3) + a\,\underline{r}_3}{2} = \frac{a\,\underline{r}}{2} = \frac{\tau(\underline{r})}{2} \tag{5.30}$$

The total reverberation noise for $Q = \tilde{V}_p = 1$, linear time delay development and the transducer as 2nd scatter can be written as:

$$N(\underline{r}, \omega, p_{LF}) = e^{i\omega\tau(\underline{r})/2} \sum_i dY_{II}(\underline{r}_{1i}, \underline{r}_{3i}, \omega) \, 2cos\left\{\frac{\omega \, p_{LF}}{2}\left(\tau(\underline{r}_{3i}) - \tau(\underline{r}_{1i})\right)\right\} \tag{5.31}$$

Here the reverberation noise can be removed by subtracting two SURF pulse complexes with equal LF magnitude and opposite polarity, where the phase difference $\omega\tau(\underline{r})/2$ has been corrected for.

As just illustrated SURF imaging can suppress reverberation noise, but strong suppression requires a transmit setup were the pulse form distortion is minimal and the time delay development is close to linear. The next section derives the phase based method used for estimating the time delay $\tau(\underline{r})$.

5.2 Estimation of the nonlinear propagation time delay

As derived in Section (2.2.1) the HF imaging pulse will be time delayed due to the LF manipulation pressure. A real-time algorithm has been established [17] [9] to estimate the time delay between two SURF pulse complexes with different LF pressures. The method uses a phase based approach which makes no assumption on the local delay variation. Other methods could be used as correlation and interpolation techniques, but the phase based approach has been chosen due to its ability to represent delays in terms of local phase differences.

Received signal model for time delay estimation

The phase based delay estimation method uses the analytic representation of the received rf data. The analytic representation will be noted as s and is a complex signal with a real positive amplitude, a, center frequency ω_c and a modulating phase, φ.

$$s(t) = a(t) \, \exp\left[i(\varphi(t) + \omega_c t)\right] \tag{5.32}$$

For the model to be valid for discrete sampled signals s is assumed to be band limited below to $fs/2$. Further two received signals from SURF pulse complexes with opposite LF pressure can be written as:

$$
\begin{aligned}
y_p(k) &= s\left(k + \frac{1}{2}\tau(k)\right) = a\left(k + \frac{1}{2}\tau(k)\right) \exp\left[i\left(\varphi\left(k + \frac{1}{2}\tau(k)\right) + \omega_c k + \frac{1}{2}\omega_c \tau(k)\right)\right] \\
y_m(k) &= s\left(k - \frac{1}{2}\tau(k)\right) = a\left(k - \frac{1}{2}\tau(k)\right) \exp\left[i\left(\varphi\left(k - \frac{1}{2}\tau(k)\right) + \omega_c k - \frac{1}{2}\omega_c \tau(k)\right)\right]
\end{aligned}
\tag{5.33}
$$

Here $\tau(k)$ is the time-varying delay between the two signals which we want to estimate.

Estimation of the phase difference ψ, and the instantaneous frequency $\dot{\theta}$

The phase difference between the two received signals y_p and y_m is found by cross multiplication.

$$
\begin{aligned}
\psi(k) &= \arg\left(y_p(k) \cdot \overline{y_m}(k)\right) \\
&= \varphi\left(k + \frac{1}{2}\tau(k)\right) - \varphi\left(k - \frac{1}{2}\tau(k)\right) + \omega_c \tau(k)
\end{aligned}
\tag{5.34}
$$

Using the definition of the derivate and the definition of the instantaneous frequency

$$\lim_{\Delta x \to 0} = \frac{f(x + \frac{\Delta x}{2}) - f(x - \frac{\Delta x}{2}))}{\Delta x} = \dot{f}(x) \tag{5.35}$$

$$\dot{\theta}(k) = \frac{d}{dt}\left[\arg\left(s(k)\right)\right] = \dot{\varphi}(k) + \omega_c \tag{5.36}$$

the phase difference can be approximated linearly through the instantaneous frequency for small time delays $\tau(k)$. The time delay between two SURF pulse complexes is often not more than 20ns.

$$\varphi(k) = \underbrace{[\dot{\varphi}(k) + \omega_c]}_{\dot{\theta}(k)} \tau(k) \tag{5.37}$$

Assuming the signal is sampled at a high rate relative to the change in instantaneous phase can we approximate the instantaneous frequency by

$$\begin{aligned} \dot{\theta}(k) &\approx \frac{1}{2} \left[\theta(k+1) - \theta(k-1) \right] \\ &\approx \frac{1}{2} \arg[s(k+1) \cdot \bar{s}(k-1)] \end{aligned} \tag{5.38}$$

Connecting the received time delayed signal y_p and y_m with the instantaneous frequency using Eq. (5.33) and Eq. (5.38).

$$\begin{aligned} \dot{\theta}\left(k + \frac{1}{2}\tau(k)\right) &\approx \frac{1}{2} \arg[y_p(k+1) \cdot \overline{y_p}(k-1)] \\ \dot{\theta}\left(k - \frac{1}{2}\tau(k)\right) &\approx \frac{1}{2} \arg[y_m(k+1) \cdot \overline{y_m}(k-1)] \end{aligned} \tag{5.39}$$

By local linear interpolation over the interval $\tau(k)$ the instantaneous frequency is found as

$$\begin{aligned} \dot{\theta}(k) &\approx \frac{1}{2} \left[\theta\left(k + \frac{1}{2}\tau(k)\right) + \theta\left(k - \frac{1}{2}\tau(k)\right) \right] \\ &\approx \frac{1}{4} \left[\arg[y_p(k+1) \cdot \overline{y_p}(k-1)] + \arg[y_m(k+1) \cdot \overline{y_m}(k-1)] \right] \end{aligned} \tag{5.40}$$

Zero phased low pass filter

It has been shown that the phase difference can be linearly related through the instantaneous frequency, $\dot{\theta}$, by

$$\varphi(k) = \dot{\theta}(k)\,\tau(k) \tag{5.41}$$

and that the phase difference and the instantaneous frequency can be calculated from the received signals using:

$$\begin{aligned} \psi(k) &= \arg\left(y_p(k) \cdot \overline{y_m}(k)\right) \\ \dot{\theta}(k) &\approx \frac{1}{4} \left[\arg[y_p(k+1) \cdot \overline{y_p}(k-1)] + \arg[y_m(k+1) \cdot \overline{y_m}(k-1)] \right] \end{aligned} \tag{5.42}$$

These equations are generally good approximations when the time delay is small, and the received rf signals are sampled at a high sampling rate relative to the fluctuations in the signal. The estimation of the time delay, τ, is done by low pass filtering $\varphi(k)$ and $\dot{\theta}(k)$.

43

$$\tau(k) = \frac{f\left(w,\ C(k)\ \varphi(k)\ \dot{\theta}(k)\right)}{f\left(w,\ C(k)\ \dot{\theta}(k)\ \dot{\theta}(k)\right)} \qquad (5.43)$$

The filter function, $f(w, x)$, is a zero phase filter. It processes the input data x in both forward and backward direction, by convolving the input data x with w before convolving the resulting data reversely with w again. The window function, w, is a rectangular window and the vector $C(k)$ is weighing the samples by its magnitude.

$$C = |y_p(k) \cdot \overline{y_m}(k)| \qquad (5.44)$$

CHAPTER 6

Phantom gel material parameters

Field simulations can be used to correct for differences between SURF Plus and SURF Minus pulses and the phantom gel material parameters are required to obtain accurate field simulations. A smaller phantom , Phantom C, was made without any calcium particles and plastic layers. This phantom was placed in a water tank to acquire information about the phantom gel sound velocity and attenuation.
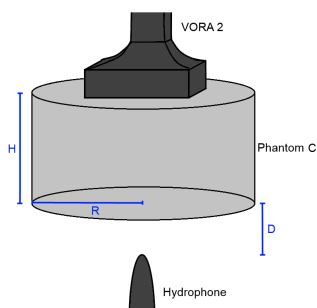
Figure 6.1: *Illustration of water tank setup with phantom C.*

6.1 Phantom gel sound velocity

Two pulses were recorded by the hydrophone with and without Phantom C positioned between VORA II and the hydrophone. The phantom gel sound velocity was calculated

by the difference in time of arrival of the two pulses. Both pulses were assumed to have traveled the same distance H within the phantom and D in water. The two recorded pulses had a time offset, (T_{os}), of $0.78\mu s$ between the maximum of the two complex envelopes. (One could argue that a more correct time offset would be between the two beginnings of the pulses.) The phantom sound velocity was calculated by

$$c_p = \frac{H\,c_w}{H - T_{os}\,c_w} \tag{6.1}$$

where the values of the variables are given in Table (6.1).

Table 6.1: *Parameters for calculation of the phantom gel velocity.*

Phantom C height(H)	$41.5mm$
Phantom C radius (R)	$27mm$
Phantom C weight	$100.22g$
Phantom C volume	$95ml$
Sound velocity phantom (c_p)	$1534m/s$
D	$8.5mm$
Sound velocity water (22.5°C) (c_w)	$1489.7m/s$
Density water (22.5°C) (ρ_w)	$998.2kg/m^3$

The phantom gel sound velocity was found to be $1534m/s$ which is close to $1540m/s$ that is known as a good average for the sound velocity in tissue. 33% less glyserol was used compared to phantom (A2) in [7] in exchange of destilled water.

6.2   Phantom gel attenuation

The phantom gel attenuation was determined by recording pulses and matching them with ForwardSIM simulations. Six pulses were recorded on the center axis: Two pulses at the transducer surface and four pulses at depth $50.0mm$.

Table 6.2: *Pulses determining the phantom gel attenuation*

Pulse NR	Propagation distance through phantom gel	Propagation distance through water	Power	Depth recorded
1	$0mm$	$0mm$	$1dB$	$0mm$
2	$0mm$	$0mm$	$2dB$	$0mm$
3	$41.5mm$	$8.5mm$	$1dB$	$50mm$
4	$41.5mm$	$8.5mm$	$2dB$	$50mm$
5	$0mm$	$50mm$	$1dB$	$50mm$
6	$0mm$	$50mm$	$2dB$	$50mm$

The transmitted pulses were focused at $20mm$ and the aperture size used was of 20 HF elements. The excitation frequency used was 10MHz, the highest frequency option in the Ultrasonix GUI, "B-Tx", and the excitation length was 1 half cycle.

The pulse transmissions between the phantom and the water are assumed to have normal incidence. For this situation the transmission coefficients for the pressure are calculated as:

$$Z_p = \rho_p \, c_p = 1.618 M Rayl \qquad T_f \quad = \frac{2Z_p}{Z_p + Z_w}$$
$$Z_w = \rho_w \, c_w = 1.487 M Rayl \qquad T_b \quad = \frac{2Z_w}{Z_p + Z_w} \tag{6.2}$$

T_f and T_b are the transmission coefficients to the front and back-end of the phantom respectively. Using the values from Table (6.1) the transmission coefficients are calculated to be:

$$T_f = 1.0422$$
$$T_b = 0.9578 \tag{6.3}$$

As ForwardSIM is unable to account for the phantom/water interfaces T_f and T_b were multiplied with the propagating pulses at depths $0mm$ and $41.5mm$. The pulse NR5 and NR6 from Table (6.2) were recorded to find the water acoustic attenuation.

The attenuation is modeled as a power law, where b will be set equal to 1.1 for all simulations.

$$P(r + \Delta r) = P(r) \, e^{-\alpha \, \omega^b \, \Delta r} \tag{6.4}$$

In the figure below pulse NR1 is simulated in water up to $50mm$ where its compared to pulse NR5. Two ways of exiting pulse NR1 were simulated: One with transmitting pulse NR1 homogeneous over the whole aperture (Sim1), and one using the variation in azimuth seen in Fig. (C.7a) (Sim2). The attenuation coefficient, α_w, was then tunned so that the maximum of the pulse in Sim2 (at $50mm$) was equal to the maximum of the recorded pulse NR5.
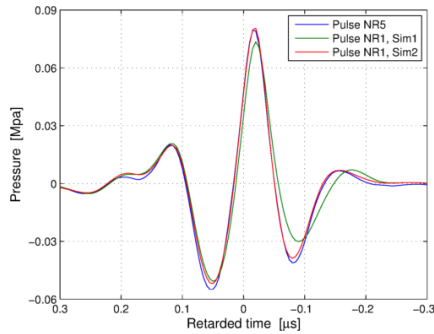

Figure 6.2: *The pulses from Sim1 and Sim2 at depth $50mm$ comparing to pulse NR5*

The variation in pressure between Sim1 and Sim2 is believed to originate from difference in the focusing quality and azimuth aperture size. Sim1 has the best focusing and largest azimuth aperture and therefore diverges the most in the far field, while Sim2 and the recorded pulse NR5 are more equal. Azimuth profiles of the two simulations Sim1 and Sim2 are shown below.
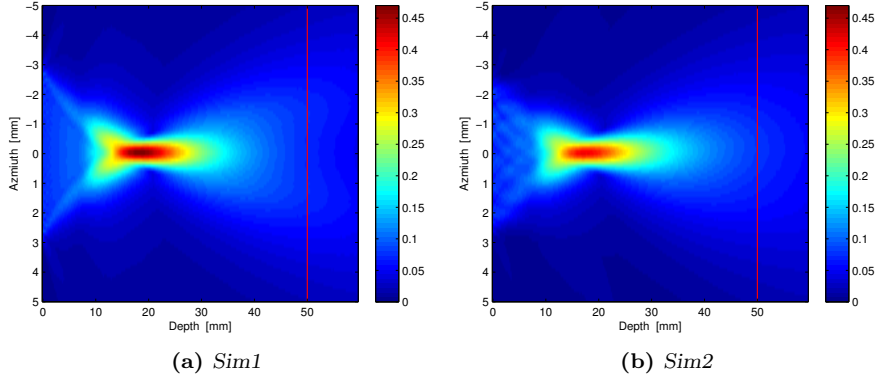

(a) *Sim1*　　　　　　　　　　　　　　(b) *Sim2*

Figure 6.3: *Azimuth profiles of Sim1 and Sim2. The red line indicate a depth of 50mm.*

The properties of water used in the simulations are listed in Table (6.4). An attempt to simulate pulse NR2 was done, but as the pressure in the focus got very high the simulation became unstable. The attenuation coefficient for the water in the water tank was found to be $0.03\,[dB/cm/Mhz]$.

The simulated pulse though the phantom did not match the recorded pulse as well as for the water simulations Fig. (6.2). For this reason the attenuation parameter, α_p, was not tuned so that the simulated pulses and the recorded pulse had the same maximum pressure. Instead the attenuation parameter was tuned so that the energy (E) became equal.

$$E = \sum_i p(i)^2 \qquad (6.5)$$

Pulse NR1 were simulated with aperture settings Sim1 and Sim2 and compared to pulse NR 3. Similar pulse NR2 was simulated and compared to pulse NR4. Below is a list of the attenuation coefficients that gave equal energy to the recorded pulses:

Table 6.3

Pulse NR1, Sim1	$0.254\,[dB/cm/Mhz]$
Pulse NR1, Sim2	$0.263\,[dB/cm/Mhz]$
Pulse NR2, Sim1	$0.212\,[dB/cm/Mhz]$
Pulse NR2, Sim2	$0.221\,[dB/cm/Mhz]$

The average of the values in the table above is $0.238\,[dB/cm/MHz]$ and this average will

be used as the phantom gel attenuation coefficient. This coefficient is less than half of the typical tissue attenuation coefficient of 0.5 $[dB/cm/MHz]$. The figures below show the comparison of the simulated pulses and the recorded pulses where the attenuation coefficients from Table (6.3) have been used:
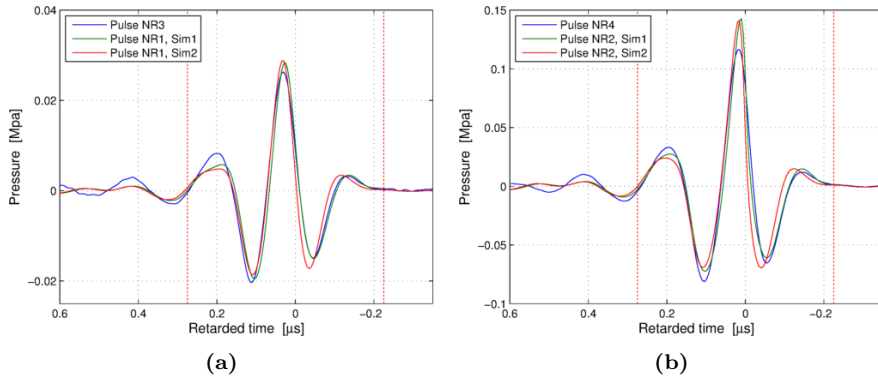

Figure 6.4: *(a) shows the comparisons of the pulses with 1dB and (b) shows the comparisons of pulses with 2dB. The two dotted red lines indicates the region where the energy was compared.*

The pulse energies were calculated within the region defined by the dotted red lines in Fig. (6.4). The reason is that recordings of pulses NR1 and NR2 do not contain the tail of the pulses, and therefore the tails of the simulated pulses have lower amplitude than the recorded pulses NR3 and NR4. Azimuth profiles of the simulations of pulse NR1 and NR2 with aperture Sim2 are shown below.

(a) *Pulse NR1, Sim2*   (b) *Pulse NR2, Sim2*
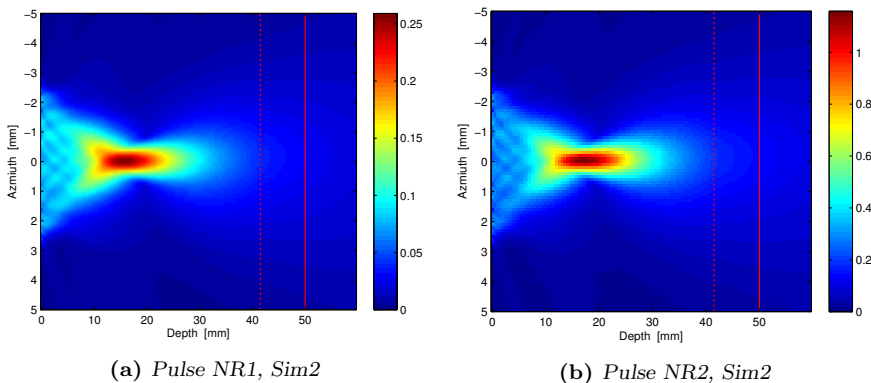
Figure 6.5: *Azimuth profiles of the field simulations of pulse NR1 and NR2. The dotted red line indicates the interface between the phantom and water, the solid red line indicate depth of 50mm.*

The material parameters used in the simulations in this section are listed below:

49

Table 6.4: *Tissue properties*

Attenuation coefficient water (α_w)	$0.03 \; [dB/cm/Mhz]$
Attenuation coefficient phantom (α_p)	$0.238 \; [dB/cm/Mhz]$
Nonlinear attenuation coefficient (b)	1.1
Speed of sound water (c_w)	$1489 \; [m/s]$
Speed of sound phantom (c_p)	$1534 \; [m/s]$
Compressibility water (κ_w)	$452 \cdot 10^{-12} \; [m^2/N]$
Compressibility phantom (κ_w)	$450 \cdot 10^{-12} \; [m^2/N]$
Nonlinear parameter water (β_n)	3.5
Nonlinear parameter phantom (β_n)	4.9

6.3 Phantom gel nonlinear parameter

A similar approach as for the attenuation coefficient will be used for finding the value of β_n. β_n is included in the nonlinear propagation term in Eq. (2.16) and is connected to the nonlinear propagation time delay. Recordings of Phantom A have been done, and estimated time delays from the recordings have been compared to the time delays obtained from field simulations using ForwardSIM.

There is an uncertainty whether the first samples in the recorded rf data correspond to the transducer surface or not. The reason for the interest in the position of the transducer surface, is because it can be used as an initial condition for the time delay estimates $\big(\tau(\underline{r} = 0) = 0\big)$. To gather information about the initial spatial position of the rf data the positions of the 1st and 3rd order scatters of the plastic layer are used (Phantom A).
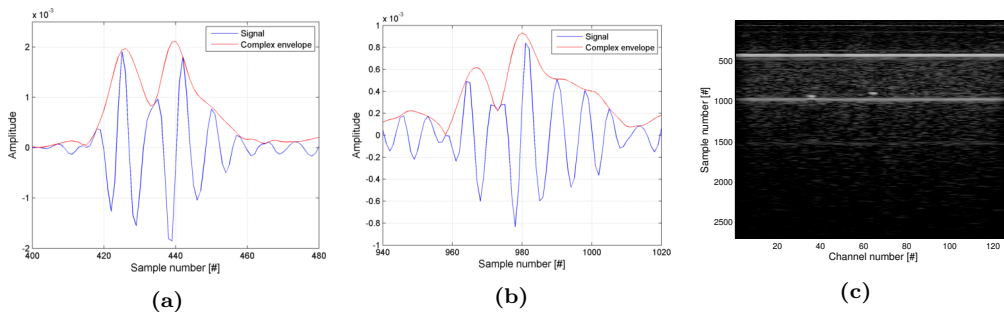

Figure 6.6: *(a) shows the received rf data around the 1st order scatter of the plastic layer (channel 50) and (b) shows the corresponding received rf data around the 3rd order scatter of the plastic layer (channel 50). (c) shows the whole section of the Phantom A*

As the phantom has one strong scatter only, the plastic layer, the main 2nd order scatter will be the transducer. We can define $z = 0$ as the interface between the first matching layer and the HF piezo layer. In the case where this interface contributes as the transmit,

2nd order scatter and the receive, the first peak from the 1st order scatters should arrive at half the sample number of the first peak from the 3rd order scatter. Using the complex envelopes from Fig. (6.6a) and Fig. (6.6b) the peaks can be located at samples 426 and 968 in the recording of Phantom A. The number of offset samples is then calculated to be:

$$N_0 = 968 - \frac{426}{2} = 116 \tag{6.6}$$

From the sampling rate of $40MHz$ 116 samples corresponds in time and distance to $2.9\mu s$ and $2.22mm$. Although it is not completely correct defining $z = 0$ at this interface, the recorded rf data will be zero padded with 116 elements at the beginning. It is not meant to state that the main reflection occurs at the interface between the first matching layer and the HF layer. The back traveling wave will to some extent be reflected at any of the interfaces in the dual layered transducer, but the strongest reflections occurs mainly at the interfaces with the piezoelectric composites where the acoustic impedances have the largest mismatch. See Table (4.2) for the transducer design stack of VORA II.

Six recordings of Phantom A were done with different LF manipulation pressure and initial phase relations. The LF excitation voltages used were $30V$, $40V$ and $50V$. The transmit setup parameters are listed in the table below:

Table 6.5: *Transmit Setup*

		HF	LF
Excitation frequencies		$10MHz$	$0.8MHz$
Number of used elements	N_{Az}	20	13
Focus	F	$20mm$	Inf
Transmit amplitude	$P0$	$2dB$	$30V,40V,50V$
Initial phase relation	τ_0	$0ns, 100ns$	$-$
(SURF Zero Adjust Delay)	(τ_0)	$(460ns, 560ns)$	$-$

The initial phase relation is not completely known. The transmit setup which corresponds to a phase relation of $0ns$ has been obtained from water tank recordings for the position of the hydrophone ($< 2mm$). This phase relation of $0ns$ was obtained by setting the parameter "SURF Zero Adjust Delay" to $460ns$ see App. (D). The phase relation for small depths has therefore been studied to estimate the original phase relation at the transducer surface.
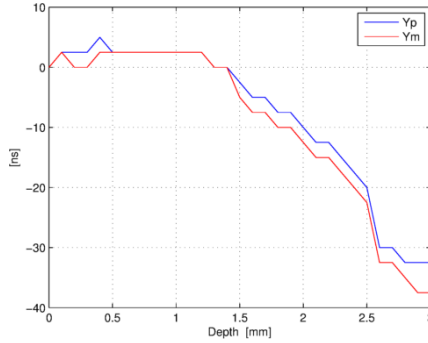
Figure 6.7: *The phase relation obtained from simulation close to the transducer for Plus (Y_p) and Minus (Y_m) LF manipulation pressure. The transmit setup corresponds to Table (6.5).*

Since the phase relation in Fig. (6.7) only varies $\sim 15ns$ the first $2mm$ the phase relation obtained from the hydrophone recordings is considered to be the correct phase relation at the transducer surface.

Before applying the phase based time delay estimation method (on the rf data from channel 105) the rf data was band pass filtered using a hamming window, a filter order of 52 and cutoff frequencies $4MHz$ and $14MHz$.
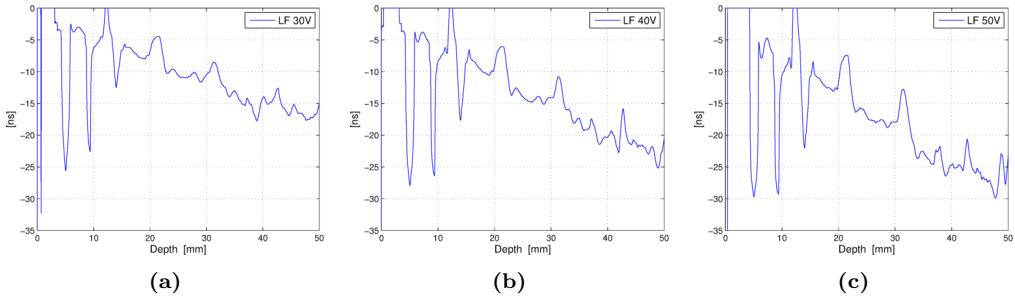
Figure 6.8: *Nonlinear time delay estimates for LF pressures 30V, 40V, 50V and initial phase relation of 100ns using the phase based method. The time delays between the Plus and Minus pulses are divided by two as then being referenced to the Zero LF pressure pulse.*

The estimation window used in the phase based method was 43 samples long, which yields an averaging over $0.82mm$. The time delay curve contains noise, and is therefore filtered before being used to correct the Plus and Minus SURF pulses. A bilateral filter is used before the curves are fitted to a polynomial of degree three. The bilateral filter is used to averaging over neighbor scan lines and it prevents counting for peaks in the time delay estimate coming from reverberations. The polynomial fitting function uses Weighted Least Squares with the constraint that the final curve goes through the origin. The time delay at the transducer surface for the Plus and Minus pulses should be zero and this is therefore a good initial condition when estimating the time delay curves. Estimating the time delays close to the transducer has proven to be difficult as the curves fluctuates substantially. For

52

this reason the samples up to approximately $6mm$ will be zero weighted.

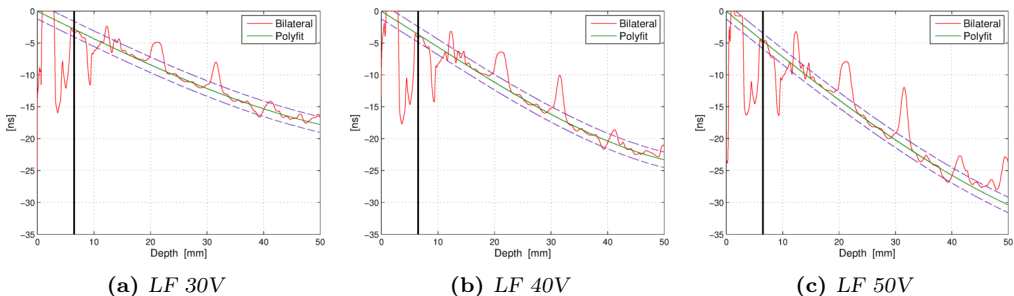**(a)** *LF 30V*   **(b)** *LF 40V*   **(c)** *LF 50V*

Figure 6.9: *Nonlinear time delay estimates for LF pressures 30V, 40V, 50V and initial phase relation of 100ns using additional bilateral filtering and polynomial curve fitting. The time delays between the Plus and Minus pulses are divided by two and then being referenced to as the Zero LF pressure pulse. The solid black line at the left indicates the first sample counted for while curve fitting the bilateral filtered curve to a polynomial. The samples used in the estimation of the polynomials have also the restriction of having values between the dotted purple lines. This is given as an criteria to prevent estimating the time delay curves on behalf of noise and reverberations.*

The polynomial fitted curves, green curves in Fig. (6.9), will now be compared to time delay estimates from field simulations for obtaining the value of β_n.

As ForwardSIM generates pulses at specified depths, it is convenient to compute time delays between the Plus and Minus pulses with a parabolic interpolation of the Normalized Correlation function. This function is used over the standard Normalized Correlation function as it has better accuracy of the maximum due to discrete samples [9].

$$\hat{\tau} = m_{max} + T_s \cdot \frac{R(m_{max} - 1) - R(m_{max} + 1)}{2\big(R(m_{max} - 1) - 2R(m_{max}) + R(m_{max} + 1)\big)} \tag{6.7}$$

m_{max} is the index maximizing the Normalized Correlation function R(m):

$$R(m) = \frac{\sum_{k=0}^{N} x(k)y(k - m)}{\sqrt{\sum_{k=0}^{N} x(k)^2 \cdot \sum_{k=0}^{N} y(k - m)^2}} \tag{6.8}$$

It has been checked that the time delay computed by Eq. (6.7) gives the same time delay estimate as the phased based method at the middle point between the Plus and Minus pulse. The transmit setups used in the simulations are equal to the one used recording Phantom A, see Table (6.5).
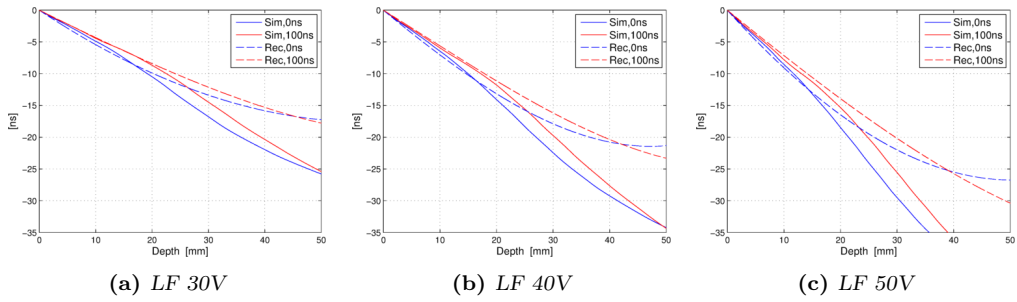
Figure 6.10: *Nonlinear time delay estimates for LF excitation voltage 30V, 40V, 50V and initial phase relations 0ns and 100ns. The solid curves show time delays estimated from simulations, and the dotted curves show time delays estimated from recordings. The time delays between the Plus and Minus pulses are divided by two and then being referenced to as the Zero LF pressure pulse.*

Unfortunately the time delay curves from simulations and recordings are not equal. For this reason it is difficult to find the correct value of β_n by comparing them. The HF and LF relation is considered to have the best fit between recording and simulation close to the transducer. β_n was therefore optimized for best match in this region and found to be 3.9. This value was used in the simulations in Fig. (6.10). 3.9 is closer to the β_n for water than the β_n for tissue Table (6.4).

CHAPTER 7

Phantom recording

The transmit setup has been investigated for achieving close to linear time delay development and minimum pulse form distortion. Both the phantoms have been processed in three different ways which will be called class 1, 2 and 3 processing. A specific description of the processing classes are given before the SURF images are presented.

7.1 Transmit setup investigation

The current SURF software implemented on the SonixMDP scanner restricts the LF aperture to be in the range of 50% -200% of the HF aperture. The number of LF elements used is always an odd number such that the center LF element is positioned behind the scan line axis. The number of HF elements used is on the other hand always an even number. Using this information the time delay development and the pulse form distortion was simulated for various transmit setups.

The deviation from linear time delay development is calculated by the RMS error between the estimated time delays and a linear time delay curve. The linear time delay curve is obtained by regression analysis of the estimated time delays with the constraint $\tau(\underline{r} = 0) = 0$. Similarly the pulse form distortion is calculated by a normalized RMS difference between time delay corrected Plus and Minus pulses, where simulated LF pulses are used as idealized band pass filters through subtraction from the SURF pulse complexes.

The filtered and time delay corrected Plus and Minus pulses will be noted u_p and u_m respectively. Using this notation the mathematical total time delay error (E_τ) and pulse form distortion ($E_{PFD}(z)$) are calculated by:

$$E_\tau = \sqrt{\frac{\sum_z^{N_z} \left(\tau(z) - \tau_{lin}(z) \right)^2}{N_z}} \qquad (7.1)$$

$$E_{PFD}(z) = \sqrt{\frac{\sum_i^{N_i} \left(u_p(z,i) - u_m(z,i) \right)^2}{N_i \; \max_i \left(u_p(z,i)^2 \right)}} \qquad (7.2)$$

By adding the contributions from all depths, an average total pulse form distortion can be expressed as.

$$E_{PFD} = \frac{\sum_z^{N_z} E_{PFD}(z)}{N_z} \qquad (7.3)$$

It is E_τ and E_{PFD} that were compared while searching for the optimal transmit setup. The combinations of HF and LF apertures that were investigated are listed in the table below.

Table 7.1: *HF / LF aperture investigation. X denotes investigated combinations.*

Number of HF elements	Number of LF elements						
	9	11	13	15	17	19	21
16	X	X	X	X	-	-	-
20	-	X	X	X	-	-	-
24	-	-	X	X	X	-	-
28	-	-	-	X	X	X	-
32	-	-	-	X	X	X	X

For all the combinations of HF and LF apertures different initial phase relations were also investigated. The initial phase relations 0ns, 50ns, 100ns and 150ns were tested. The resulting setups which gave the smallest total time delay error and total pulse form distortion for each HF aperture size is now obtained.

Table 7.2: *HF / LF aperture investigation for PFD*

HF elements	LF elements	Initial phase relation	E_{PFD}
[#]	[#]	[ns]	
16	15	50	$1.64 \cdot 10^{-4}$
20	15	50	$1.68 \cdot 10^{-4}$
24	15	0	$1.75 \cdot 10^{-4}$
28	15	0	$1.85 \cdot 10^{-4}$
32	15	0	$1.96 \cdot 10^{-4}$

Table 7.3: *HF / LF aperture investigation for linear time delay*

HF elements	LF elements	Initial phase relation	E_τ
[#]	[#]	[ns]	[ns]
16	15	100	0.343
20	15	50	0.427
24	17	0	0.377
28	17	0	0.523
32	21	0	0.563

The pulses used in the simulations were initially intended to be generated with Xtrans, but as real pulses from recordings were available those were used instead. The specific HF pulse used was generated with excitation frequency $10MHz$, one half-cycle excitation length and power $2dB$. The LF pulse used was excited by $50V$ peak, with excitation frequency $0.8MHz$ and five half-cycles length. Since the calcium particles and the reverberations in the phantom boxes occur at depth shallower than $30mm$, the above setups have been investigated for depths up to $30mm$.

Both the total pulse form distortion error and the total time delay error increase with increased HF aperture size. For this reason the HF and LF apertures that were used consist of 20 HF elements and 15 LF elements. This HF aperture size has also a typical value of F-number 3.33. Below is the corresponding time delay curve and pulse form distortion curves:

(a)

(b)
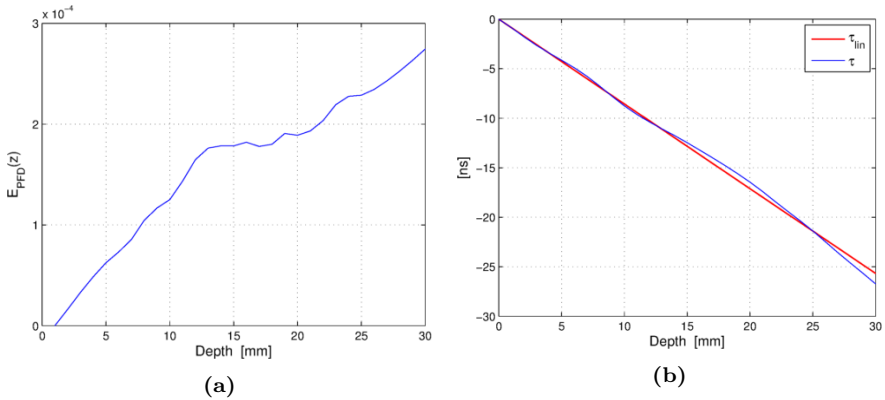
Figure 7.1: *(a) the pulse form distortion and (b) the time delay error for the apertures of 20 HF elements and 15 LF elements.*

7.2 Data processing

The band pass filtered received rf data from each channel (ch) will be noted $y_{p,ch}$ and $y_{m,ch}$ for Plus and Minus LF pressure respectively. Similarly the time delay corrected rf data are noted $\tilde{y}_{p,ch}$ and $\tilde{y}_{m,ch}$:

$$\tilde{y}_{p,ch}(z) = y_{p,ch}\big(z + c\tau(z)\big)$$
$$\tilde{y}_{m,ch}(z) = y_{m,ch}\big(z - c\tau(z)\big)$$
(7.4)

The Plus and Minus pulses will be time corrected for two cases:

- Case 1: Suppression of first order linear scatters.

- Case 2: Suppression of reverberations

In Case 1 the time delay ($\hat{\tau}$) will be correcting the time difference between the Plus and Minus pulse. In Case 2 the time delay ($\hat{\tau}_n$) will correct with the time delay at half depth. The value used as τ in Eq. (7.4) for the two cases are given in mathematical terms by:

$$\tau(z) = \hat{\tau}(z)$$
$$\tau(z) = \hat{\tau}_n(z) = \hat{\tau}(z/2)$$
(7.5)

To understand the difference between Case 1 and 2 the time delay corrections are applied to the signal model Eq. (5.1). In the signal model τ and τ_n are the true time delays, and p ,the LF pressure, is included in the magnitude of the time delays.

Case 1

$$\tilde{Y}_{ch}(z,\omega,p) = \Big\{X_l(z,\omega) + pX_n(z,\omega)\Big\}\tilde{V}_p(z,\omega,p)e^{i\omega(\tau(z)-\hat{\tau}(z))} \; + \; \tilde{N}(z,\omega,p)e^{i\omega(\tau_n(z)-\hat{\tau}(z))}$$
$$\tilde{Y}_{ch}(z,\omega,-p) = \Big\{X_l(z,\omega) - pX_n(z,\omega)\Big\}\tilde{V}_p(z,\omega,-p)e^{-i\omega(\tau(z)-\hat{\tau}(z))} + \tilde{N}(z,\omega,-p)e^{-i\omega(\tau_n(z)-\hat{\tau}(z))}$$
(7.6)

If the pulse form distortion included by V_p was not LF pressure related, and the estimated time delay, $\hat{\tau}(z)$, was equal the true time delay, $\tau(z)$, then the received signal from linear scatters, X_l, could be removed by subtraction:

$$\tilde{Y}_{ch}(z,\omega,p) - \tilde{Y}_{ch}(z,\omega,-p) = 2pX_n(z,\omega) + \; \tilde{N}(z,\omega,p)e^{i\omega(\tau_n(z)-\hat{\tau}(z))}$$
$$- \tilde{N}(z,\omega,-p)e^{-i\omega(\tau_n(z)-\hat{\tau}(z))}$$
(7.7)

Case 2

$$\tilde{Y}_{ch}(z,\omega,p) = \left\{ X_l(z,\omega) + pX_n(z,\omega) \right\} \tilde{V}_p(z,\omega,p) e^{i\omega(\tau(z)-\hat{\tau}_n(z))} \ + \ \tilde{N}(z,\omega,p) e^{i\omega(\tau_n(z)-\hat{\tau}_n(z))}$$

$$\tilde{Y}_{ch}(z,\omega,-p) = \left\{ X_l(z,\omega) - pX_n(z,\omega) \right\} \tilde{V}_p(z,\omega,-p) e^{-i\omega(\tau(z)-\hat{\tau}_n(z))} + \tilde{N}(z,\omega,-p) e^{-i\omega(\tau_n(z)-\hat{\tau}_n(z))}$$

$$(7.8)$$

Similarly if $\tilde{N}$ was not LF pressure related, and the estimated time delay, $\hat{\tau}_n(z)$, was equal to the true time delay, $\tau_n(z)$, then the received signal form reverberation noise, $\tilde{N}$, could be removed by subtraction:

$$\tilde{Y}_{ch}(z,\omega,p) - \tilde{Y}_{ch}(z,\omega,-p) = \left\{ X_l(z,\omega) + pX_n(z,\omega) \right\} \tilde{V}_p(z,\omega,p) e^{i\omega(\tau(z)-\hat{\tau}_n(z))}$$
$$- \left\{ X_l(z,\omega) - pX_n(z,\omega) \right\} \tilde{V}_p(z,\omega,-p) e^{-i\omega(\tau(z)-\hat{\tau}_n(z))}$$

$$(7.9)$$

Case 3

An extension of Case 1 can be added as Case 3 where we try to correct for the difference between $V_p(z,\omega,p)$ and $V_p(z,\omega,-p)$. The pulse form correction filter, V, was made using ForwardSIM simulations were Plus and Minus pulses were simulated nonlinearly to depth z and linearly from z to depth $2z$. This replicates the situation of a plane reflector where the amplitude of the propagating wave drops sufficiently so that further propagation can be assumed to be linear. ForwardSIM simulations were repeatedly performed for z in the range $1mm$ to $30mm$ with an increment of $1mm$. The material parameters found for the agar gel in Section (6) were used as tissue parameters. The correction filter V is then given by

$$V(z,\omega,p) = \frac{U_p(z,\omega,p)}{U_m(z,\omega,p)} \cdot K_p(z,\omega,p) = \frac{\tilde{V}_p(z,\omega,p)}{\tilde{V}_p(z,\omega,-p)} \cdot K_p(z,\omega,p)$$

$$(7.10)$$

where

$$K_p(z,\omega,p) = \frac{1}{1 + \mu \frac{U_p(z,\omega,p)}{U_m(z,\omega,p)}}$$

$$(7.11)$$

U_p and U_m are the received beamformed "rf data" from simulation of Pulse and Minus pulses respectively. K_p is used as a damping factor where U_m gets close to zero, and the value of μ determines the damping. By multiplying the pulse form correction filter with the received Minus pulse, Eq. (7.7) for Case 3 becomes:

$$\tilde{Y}_{ch}(z,\omega,p) - \tilde{Y}_{ch}(z,\omega,-p) = 2pX_n(z,\omega) + \ \tilde{N}(z,\omega,p) e^{i\omega(\tau_n(z)-\hat{\tau}(z))}$$
$$- V(z,\omega,p)\tilde{N}(z,\omega,-p) e^{-i\omega(\tau_n(z)-\hat{\tau}(z))}$$

$$(7.12)$$

Now V_p does not need to be LF pressure independent as long as the pulse form correction filter is correct.

The next sections contains images of Phantom A and Phantom B. While interpreting the images quality the Relative Tissue Suppression (RTS) will be used. The Relative Tissue Suppression is calculated with IQ data.

$$RTS(\underline{r}) = \frac{IQ\Big(\tilde{y}_p(\underline{r}) - \tilde{y}_m(\underline{r})\Big)}{IQ\big(\tilde{y}_m(\underline{r})\big)} \tag{7.13}$$

7.3   Phantom A images

Phantom A has one plastic layer, two steel wires and calcium particles. A cross section of the phantom is seen below.
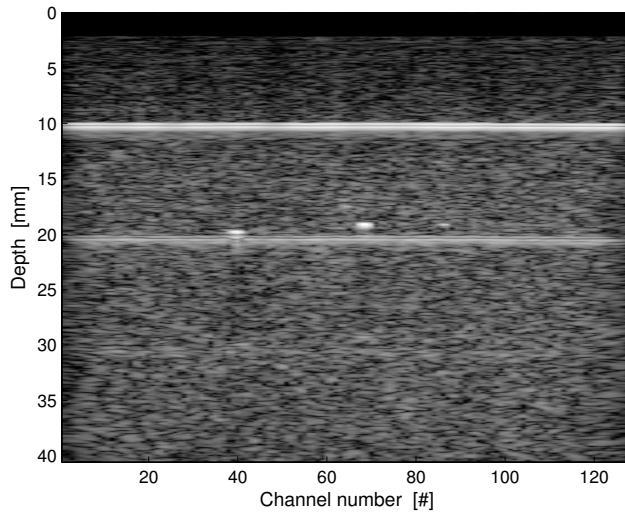
Figure 7.2: *Conventional B-mode image of a cross section of Phantom A*

To investigate the signal to noise ratio between data processed by class 1, 2 and 3 introduced in the previous section the cross section is color coded.
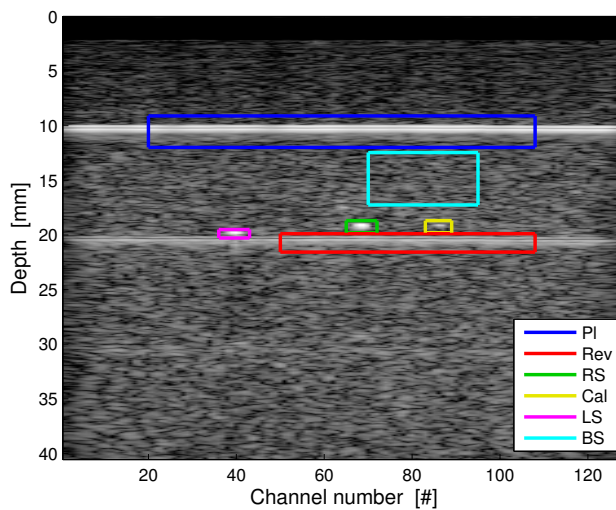
Figure 7.3: *Color coding areas of the cross section of Phantom A*

- The blue box covers a region of the plastic layer and is noted as "Pl".

- The red box covers a region of the reverberation and is noted "Rev".

- The green box covers the right steel wire and is noted "RS".

- The yellow box covers a calcium particle and is noted "Cal".

- The magenta box covers the left steel wire and is noted "LS".

- The cyan box covers a region of backscatters and is noted "BS".

The values used in the SNR calculations are the maximum value within the boxes (IQ data), except for the value of the backscatter where an average of the IQ data has been used.

Removing the received LF pulse from the SURF pulse complex has been a challenge, since the LF pulse creates frequency components within the HF frequency band. Therefore bandpass filtering only has not shown to sufficiently eliminate the LF. To improve "filtering" single LF pulses have been transmitted, and then subtracted from the SURF pulse complex. Below is an image produced by the LF pulse only. The cutoff frequencies used in the bandpass filter to filter the rf data are 3.5MHz and 14MHz, which also is the frequencies used in all other images.
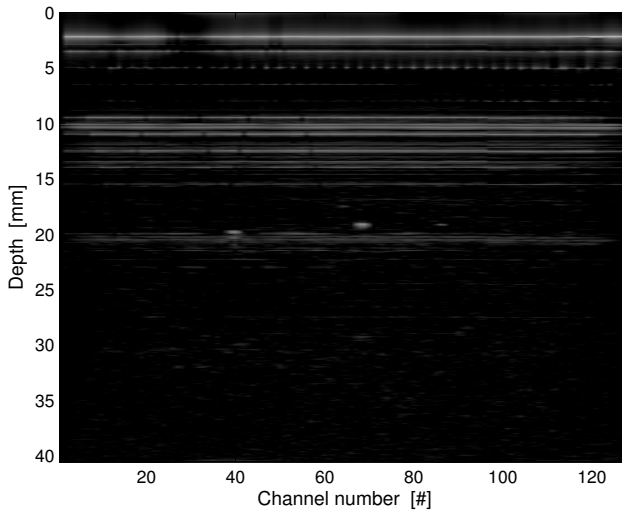
Figure 7.4: *Conventional B-mode image of the cross section of Phantom A produced by the LF pulse only.*

The rf data from channel 86 used to produce Fig. (7.5) is the main channel containing scatter from the calcium particle (Cal). The received signal from the calcium particle is seen at depth $\sim 19mm$ and the signals from the plastic layer and its main reverberation is located at $\sim 10.5mm$ and $\sim 21mm$ respectively.
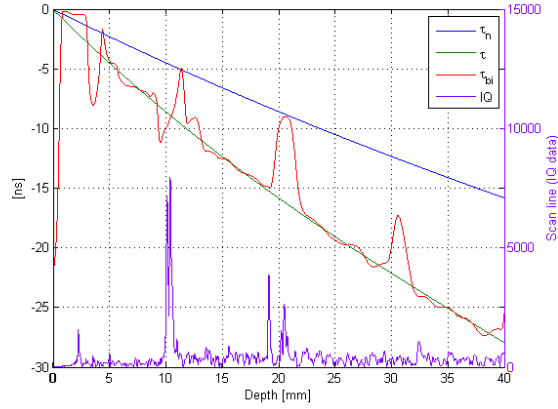
Figure 7.5: *IQ data from channel 86 is plotted with three time delay estimates. The red line is the bilaterally filtered time delay estimate (τ_{bi}), and the green line is the polynomially fitted time delay estimate (τ). The blue line is time delay estimate used to correct for reverberations (τ_n).*

The bilaterally filtered time delay estimate shows how the time delay drops at the reverberations. The time delay also varies around the plastic layer which was not expected. The reason for the variation in time delay around the plastic layer is considered to origin from interfering signal components of the LF pulse.

Now the data from the recording of Phantom A will be processed according to the three classes 1, 2 and 3. The imaging setup used can be seen in App. (D) Setup 1.

Class 1 signal processing
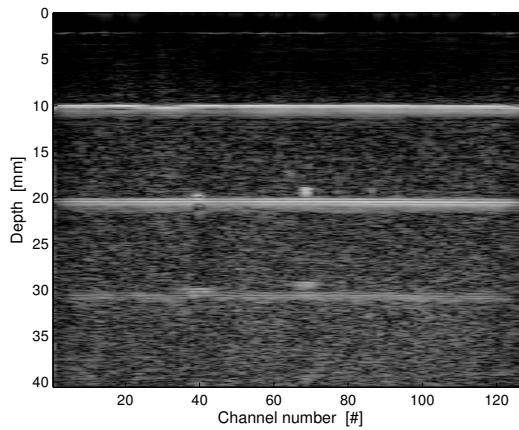
Figure 7.6: *The cross section of Phantom A processed as class 1*

63

The change in SNR ratio with respect to the areas in Fig. (7.3) is seen in the figure below.
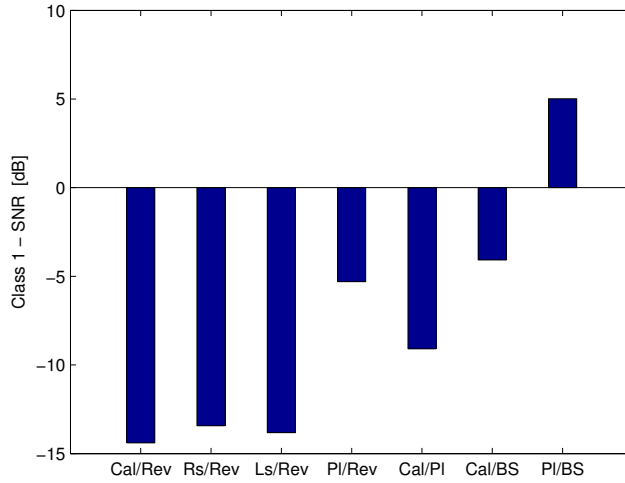

Figure 7.7: *Change in SNR by class 1 processing compared to conventional B-mode image*

Class 1 signal processing was done to enhance nonlinear scattering from the calcium particle and the two steel wires, but as seen in Fig. (7.7) the SNR for the three scatters dropped $\sim -14dB$. The only enhanced SNR was between the plastic layer and the backscatter. The figure below contains the relative tissue suppression which again indicates less suppression at the regions with reverberations. Another important observation is how the suppression of backscatter reduces as a function of depth, which indicates an accumulative pulse form distortion.
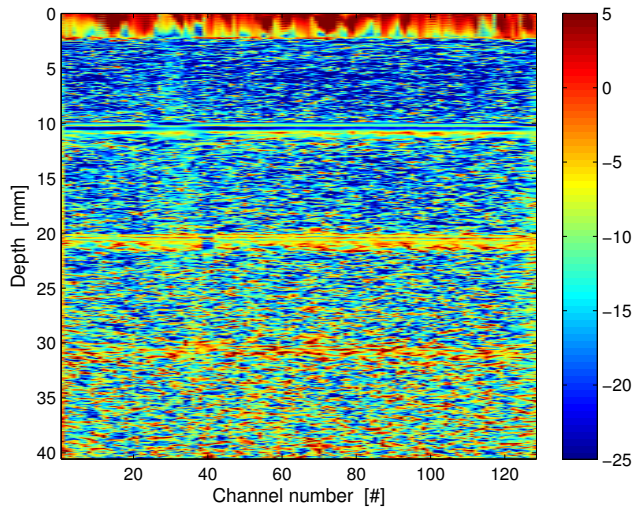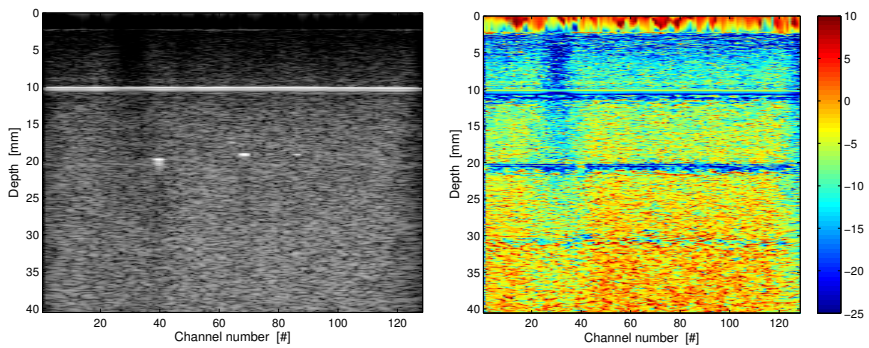

Figure 7.8: *Relative Tissue Suppression (RTS) for class 1 signal processing*

The region where the SNR to the plastic layer has increased corresponds to the depth of the crossing between bilateral filtered time delay estimate and the polynomial fitted time delay estimate.

Class 2 signal processing

(a) *The cross section of Phantom A class 2 signal processed* (b) *Relative Tissue Suppression (RTS) class 2 signal processed*

Figure 7.9

By processing the received rf data corresponding to class 2 the Class 3 reverberation can be suppressed giving an increased SNR of 8-9dB. Fig. (7.9b) also shows that the lower area of the plastic layers gets suppressed.
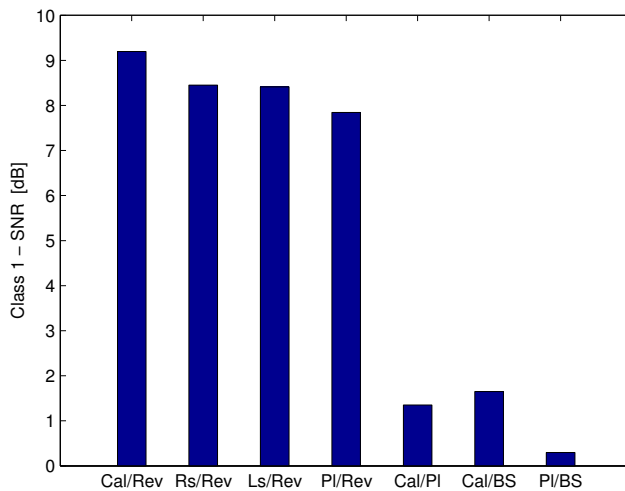

Figure 7.10: *Change in SNR by class 2 processing compared to conventional B-mode image*

Class 3 signal processing

(a) *The cross section of Phantom A class 3 signal processed*

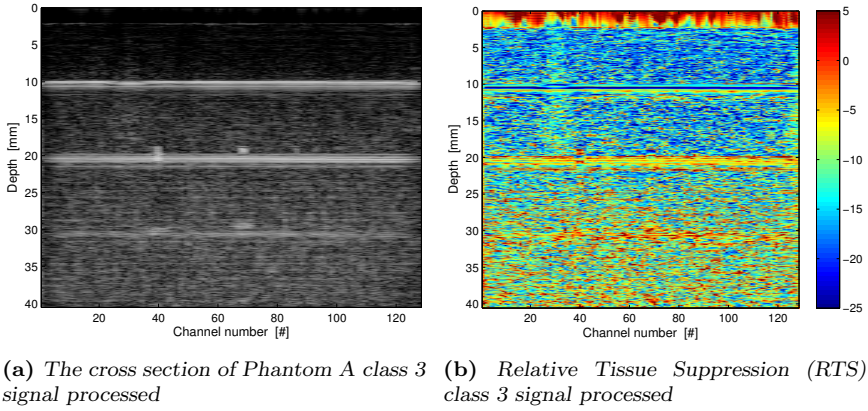(b) *Relative Tissue Suppression (RTS) class 3 signal processed*

Figure 7.11

The class 3 processing with the included pulse form correction filter does not increase the SNR compared to class 1 processing, and the SNR with respect to the reverberation is still decreased compared to conventional B-mode imaging.
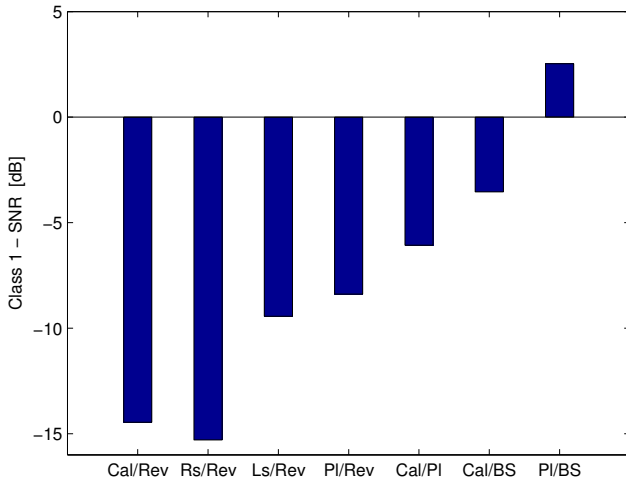

Figure 7.12: *Change in SNR by class 3 processing*

7.4 Phantom B images

Phantom B was made with two plastic layers, two steel wires and calcium particles. The Calcium particles could not to be located with ultrasound and therefore the two steel wires are the "point" scatters only. A cross section of phantom B is seen below.
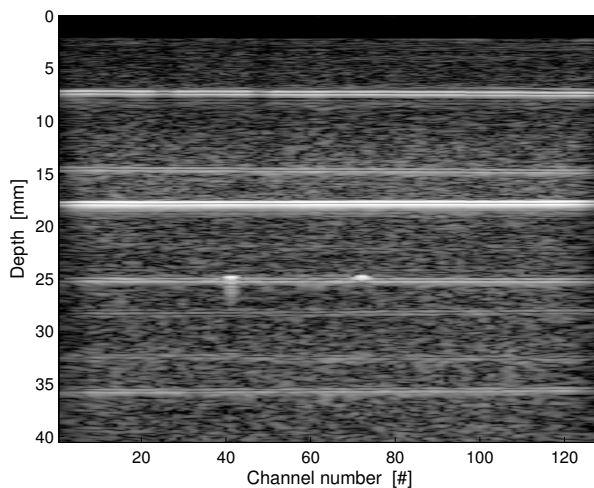

Figure 7.13: *Conventional B-mode image of a cross section of Phantom B*

Color coding is also used for Phantom B to investigate the SNR between data processed by class 1, 2 and 3 were each area gets it own abbreviation.
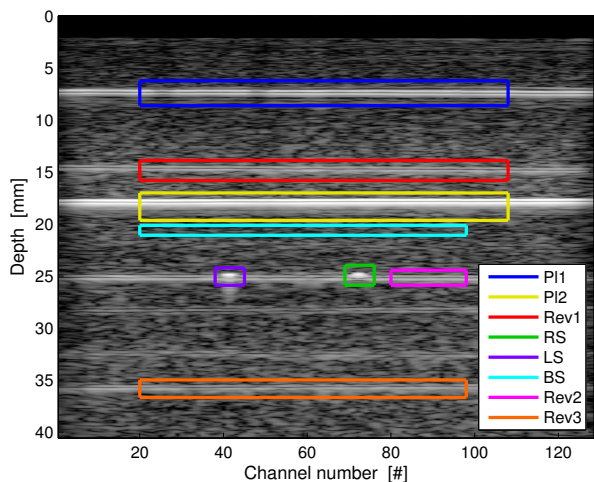

Figure 7.14: *Color coded areas of the cross section of Phantom B*

- The blue box covers a region of one of the plastic layer and is noted as "Pl1".

- The yellow box covers a region of the other plastic layer and is noted as "Pl2".

- The red box covers a region of the Class 3 reverberation produced by "Pl1" and is noted as "Rev1".

- The green box covers the right steel wire and is noted "RS".

- The purple box covers the left steel wire and is noted "LS".

- The cyan box covers a region of backscatters and is noted "BS".

- The magenta box covers the class 1/2 reverberation produced by "Pl1" and "Pl2" and is noted "Rev2".

- The orange box covers the class 3 reverberation produced by "Pl2" and is noted "Rev3".

Below the rf data from channel 85 is plotted as IQ data together with the time delay estimates. Channel 85 does not contain any signals from scattering of the two steel wires.
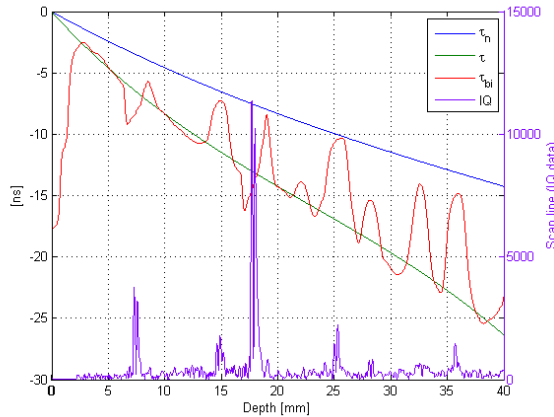

Figure 7.15: *(Phantom B) IQ data from channel 85 is plotted with three time delay estimates. The red line is the bilateral filtered time delay estimate (τ_{bi}), and the green line is the polynomial fitted time delay estimate (τ). The blue line is time delay estimate that is used to correct for reverberations (τ_n).*

The figure illustrates nicely how the time delay drops at all the reverberations, by comparing the signal strength of the IQ data together with the bilateral filtered time delay estimate.

The data recorded from of Phantom B will now be processed accordingly to the three classes 1, 2 and 3. The imaging setup used can be seen in App. (D) Setup 2.

Class 1 signal processing
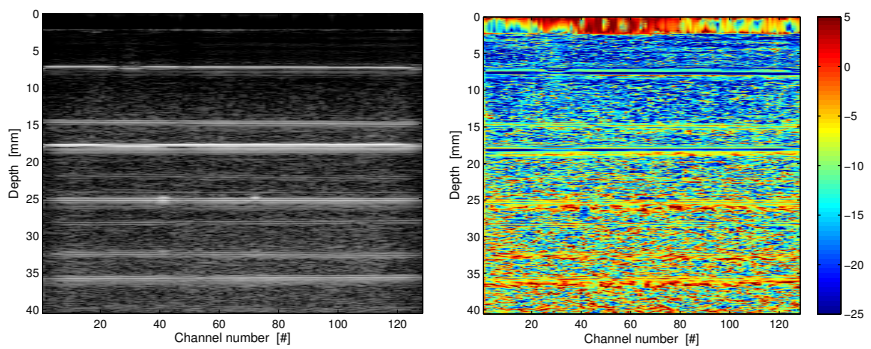
(a) *The cross section of Phantom B class 1 signal processed*

(b) *Relative Tissue Suppression (RTS) class 1 signal processed*

Figure 7.16

The image quality decreases with class 1 processing as also seen for Phantom A.
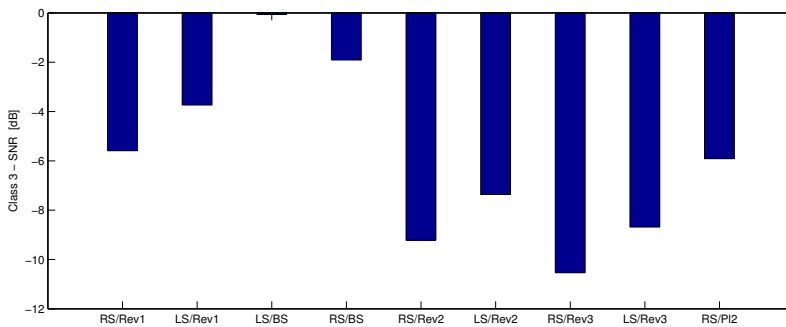
Figure 7.17: *Change in SNR by class 1 processing compared to conventional B-mode image*

Class 2 signal processing

(a) *The cross section of Phantom B class 2 signal processed*

(b) *Relative Tissue Suppression (RTS) class 2 signal processed*
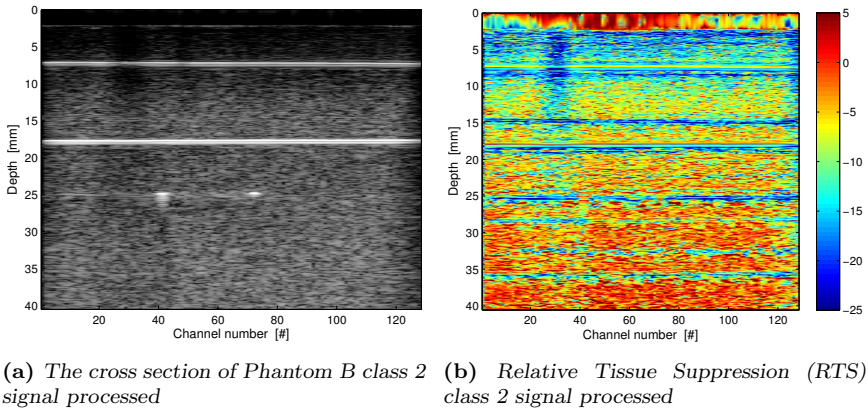
Figure 7.18

Class 2 signal processing has now shown also to successfully remove class 1 and class 2 reverberations. Both steel wires have an increased SNR $\sim 11 - 12dB$ to the coinciding reverberation.

Figure 7.19: *Change in SNR by class 2 processing compared to conventional B-mode image*

Class 3 signal processing

(a) *The cross section of Phantom B class 3 signal processed*
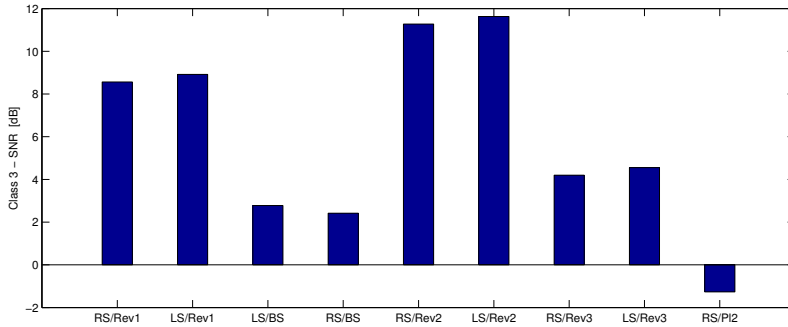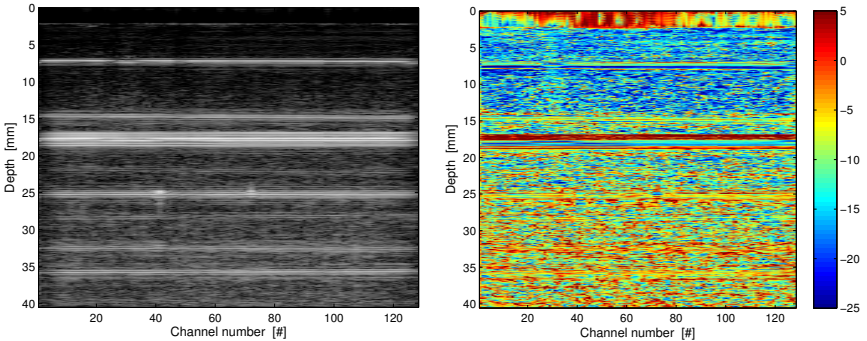
(b) *Relative Tissue Suppression (RTS) class 3 signal processed*

Figure 7.20

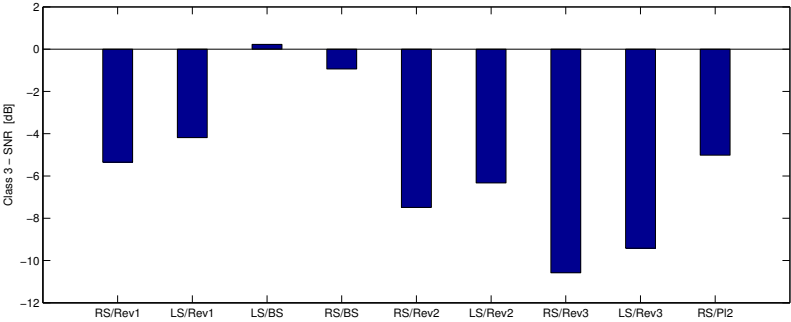There are still only small changes in the SNR compared to class 1 processing.

Figure 7.21: *Change in SNR by class 3 processing*

Discussion

In this thesis it has been demonstrated that reverberations can be suppressed by $8 - 12dB$ using class 2 processing. Class 1 and class 3 processing did not demonstrate similar results. In the following some of the challenges and possible improvements of class 1 and 3 processing are discussed.

Processing classes

The three classes defining the processing techniques for the received SURF rf data introduced in Section (7.1) did not all give results as hoped. Class 1 processing is designed to suppress 1st order linear scattering. By comparison of the conventional B-mode image and the class 1 processed image of Phantom A, in Fig. (7.2) and Fig. (7.6), it is clear that the background scatter is suppressed. It can also be observed that the suppression level of the background scatter is reduced with depth even when taking the TGC setting into consideration. This is also supported by the figure showing the Relative Tissue Suppression in Fig. (7.8). Two possible reasons for the decreased RTS with depth are pulse form distortion or wrong time delay correction. Since the signal to noise ratio in the received rf data is also high deep into the phantoms, the reason for the decreased RTS is considered to origin from pulse form distortion. The class 1 processing given by Eq. (7.7) shows that reverberations are not supposed to be suppressed which is also verified in Fig. (7.6). That the SNR between the calcium particle and background scatter is reduced by $-4dB$ indicates that the received Plus and Minus pulses have different shapes. Although pulse form distortion can reduce the signal amplitude of the subtracted Plus and Minus pulse from the calcium particle, another challenge has been observed. The received LF pulse contains frequency components within the HF pass band. Fig. (7.4) shows a B-mode images produced by the LF pulses only. After band pass filtering the SURF pulse complex, it has been observed that up to 10% of the pulse received from the first plastic layer origins from the LF pulse. The reason for the

interfering LF pulse is discussed below.

The class 2 processing was able to reduce the class 3 reverberation in Phantom A and class 1,2 and class 3 reverberations in Phantom B. Fig. (7.18a) of Phantom B shows that the class 1,2 reverberation is still present after class 2 processing. The reason for the limited suppression of class 1,2 reverberations can be that the time delay curve is not completely linear, and that Q is not equal to 1 for the class 1,2 reverberation. The Vp parameter is also different for the two reverberation layers (see Section (5.1))

Pulse form correction filter

The pulse form correction filter included in the class 3 processing had no improvement on the images. It only introduced noise as horizontal lines below depth of $20mm$. Without considering the effect of the LF produced frequencies in the HF pass band, the pulse form correction filter is mainly limited by how close its possible to reconstruct the imaging situation. The correction filter applied was created to suppress 1st order linear scatter through simulations with pulses obtained from water tank recordings. The material parameters used were those found in Section Section (6), which should be close to correct values. However, as experienced while comparing the time delay estimates from simulations and recordings Fig. (6.10), the simulations does not represent the reality. It has also been observed that the time delay estimates vary across different scan lines. Below is an image where the time delays from channel 30 to 100 is plotted on top of each other.
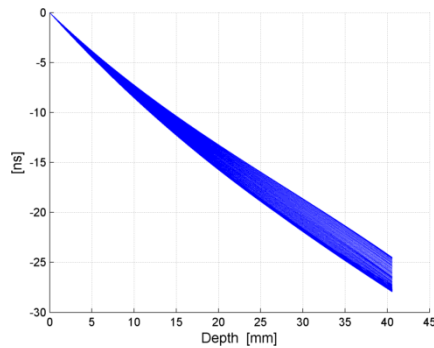
Figure 8.1: *Variation in the polynomial fitted time delay curve across the scan lines number 30 to 100.*

A more thorough design of the pulse form correction filters can be accomplished by using complete beam fields obtained from water tank recording in simulations. While designing a pulse form correction filter for reverberations suppression, complex reflection coefficients can also be obtained from Xtrans simulations.

Another pulse form correction filter has also been designed from the received rf signals produced by the reflection of the front interface of the plastic layer (Phantom A). Since this reflection is much stronger than scattering from surrounding tissue the received signal

is similar to the true pulse. A pulse form correction filter was then created for the Minus pulse, and applied for depth equal to the plastic layer and below. By studying the Minus, Plus and the corrected Minus pulse of one rf scan line, it was demonstrated that the corrected Minus pulse was equal to the Plus pulse at the interface of the plastic layer. The corrected Minus pulse did however not become more equal the Plus pulse for other depths.

LF frequency components within the HF pass band

The received LF pulse has shown to have a non negligible amount of energy within the HF frequency band. For this reason the rf data from a single transmitted LF pulse was always subtracted from the rf data from the SURF pulse complexes. The single transmitted LF pulse was not transmitted subsequently after the SURF pulse, but rather as a separate recording. Although the phantom is a stationary imaging object, only small deviations can change the received rf data significantly. For this reason the accuracy of the subtracted LF pulse is considered to be one of the main reasons why class 1 processing reduced the SNR between the calcium particle and the background scatter in Phantom A and B. All the images given in Section (7) were taken with LF excitation voltage $50V$ peak, HF power $8dB$ and initial phase relation of $50ns$. Other transmit setups have been investigated, but the resulting images from all the different transmit setups were similar, which can indicate that the interfering LF is the limiting factor. Below rf data are plotted for single LF, the SURF pulse and the SURF pulse where the LF has been subtracted.
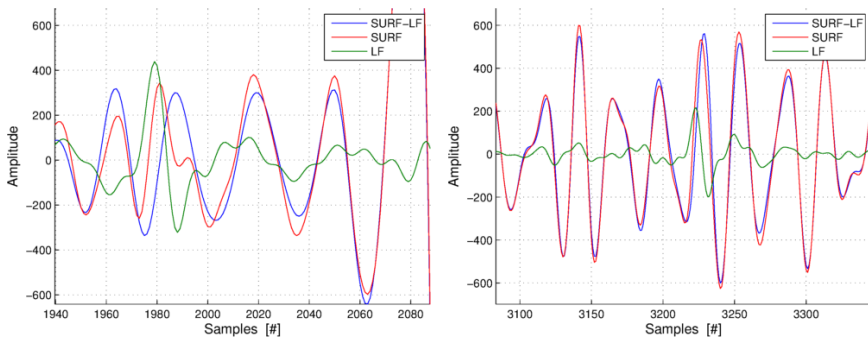
(a) *Bandpass filtered rf data from Phantom A right before the interface with the plastic layer*

(b) *Bandpass filtered rf data from Phantom A between the 1st and 3rd order scatter from the plastic layer*

Figure 8.2

At sample 1980 in Fig. (8.2a) the single LF pulse has a larger amplitude then the two SURF pulses. The reason is that the front of the LF pulse is transmitted before the HF pulse, and right before the interface of the plastic layer the received LF signals are dominated by the reflection from the plastic layer, while the HF pulse is still scattered by the background scattering only. The interfering LF pulse in this area also produces the over shot and under shot in the bilateral time delay estimate in Fig. (7.5). Similar time delay estimates have been observed around the steel wires and the calcium particle. The relative size of these

scatters are different for the HF and LF pulses, and therefore the scattering cross sections is also lower for the LF pulse. This reduces the amplitude of the interfering LF pulse compared to the region around the plastic layer.

The frequency components within the LF pulse was studied in Section (4.1) and obtained from water tank recordings, in App. (C.1). The transmitted LF pulse has a drop of $-45dB$ within the HF frequency band. As observed in figure Fig. (8.2) the received LF pulse has an increased amplitude in the received rf data. This is may to origin from both nonlinear propagation distortion or nonlinear scattering.

Polynomial fitting time delay curve

The standard method to achieve the time delay used for correcting the Plus and Minus pulses has been obtained by drawing lines between the main negative peaks in the time delay estimate. Since the LF pulse produces an overshot in the time delay estimate before each plastic layer, the previous method will fail. Therefore the polynomial time delay fitting function was developed. The function performs well for both phantoms, but in imaging of real tissue where the time delay estimate may fluctuate, the polynomial fitting function may also fail. The current implementation is also too slow for real time acquisition.

TGC

It is important to consider the Time Gain Control (TGC) settings (App. (D)) while interpreting the images. The TGC setting used during imaging of both phantoms were set to strongly suppress signals from scatters close to the transducer. This can be observed in the B-mode image of Phantom A, Fig. (7.2), where the intensity close to the transducer is lower than the intensity at depth 20 mm. The reason for this unusual TGC setting was that the received LF pulse scattered from the plastic layer saturated one or more stages of the front end electronics (the ADC is assumed to be the limiting component).

CHAPTER 9

Conclusion

In the present work, SURF imaging has demonstrated to be effective removing reverberations from plane reflectors. Both class 1,2 and class 3 reverberations are highly suppressed with time delay correction z/2 ($\tau(z/2)$). The SNR for scatters from stiff particles/wires was increased by 8 - 9dB for Phantom A and by 11 - 12dB for Phantom B while the reverberations noise was suppressed. Enhanced nonlinear scattering by suppression of linear scattering failed. This is considered to origin from interfering signals from the LF pulse within the pass band.

9.1 Future Work

The finding that the LF pulse interferes with frequencies within the HF frequency band should also be addressed in further work. The recording of the different transmit setups is currently implemented manually, and is therefore an unnecessary time consuming operation. Recording should be automated and should also facilitate the possibility to search for the optimal transmit setup. Saturation issues in the front-end electronics currently limit the maximum amplitude of the transmitted LF pulse. An analog high pass filter can be inserted to filter out most of the received LF energy. However, if the high pass filter is inserted at the connector, the filter will also affect the HF pulses during transmit. If the filter is inserted right before the Low Noise Amplifier (LNA) the compatibility with transducers with lower center frequencies is affected.

The amplitude of the transmitted LF pulse is currently limited by the issue regarding saturated in the front end. An analog high pass filter can be mounted as to filter out most of the received LF energy. However, if the high pass filter is mounted in the connector, the HF pulses will also be effected by the filter in transmit. If the filter in mounted right before the Low Noise Amplifier (LNA) an issue with the compatibility of transducers with different

center frequency occurs. The importance regarding a high pass filter should be considered.

Recording of various transmit setups has today be done manually, and is an unnecessary time consuming procedure. Recording should be atomized which also facilitates the possibility to search for the optimal transmit setup. That the LF pulse interfere with frequencies within the HF frequency band should also be addressed in further work.

Bibliography

[1] Abersim. http://www.ntnu.no/isb/abersim.

[2] Design of vora: Linear surf array.

[3] Google sketchup 8. http://www.sketchup.com/product/newin8.html.

[4] Surf technology. http://www.surftech.no/.

[5] Ultrasound transducers technical notes. http://www.olympus-ims.com/data/File/panametrics/UT-technotes.en.pdf.

[6] Vermon. http://www.vermon.com/vermon.

[7] Mercy Afadzi. *Detection of Microcalcifications for Breast Cancer Diagnosis Using SURF Imaging*. NTNU, December 2007.

[8] Tonni F. Johansen Bjørn Angelsen, Rune Hansen and Svein-Erik Msy. *Utilizing dual frequency band transmit pulse complexes in medical ultrasound imaging*, volume 127. jan 2010.

[9] Bastien Emmanuel Denarie. *Using SURF imaging for efficient detection of microcalcification*. NTNU, june 2010.

[10] Rune Hansen and Bjørn A. J. Angelsen. Surf imaging for contrast agent detection. *IEEE Transactions on Ultrasonics, Ferroelectrics, and Frequency Control*, 2:280–290, 2009.

[11] Ola Finneng Myhre. *characterization of a Dual-Band, Piezoelectric Ultrasound Transducer*. NTNU, 2012.

[12] Takeshi Nagashima, Hideyuki Hashimoto, Keiko Oshida, Shigeharu Nakano, Naoto Tanabe, Takashi Nikaido, Keiji Koda, and Masaru Miyazaki. Ultrasound demonstration of mammographically detected microcalcifications in patients with ductal carcinomain situ of the breast. *Breast Cancer*, 12(3):216–220, 2005.

[13] Bjørn Angelsen. *Ultrasound Imaging - Waves, Signals, and Signal Processing*, volume 1. Emantec, 2000.

[14] Bjørn Angelsen. *Ultrasound Imaging - Waves, Signals, and Signal Processing*, volume 2. Emantec, 2000.

[15] Bjørn Angelsen and Thor Andreas Tangen. *Nonlinear imaging with dual band pulse complexes.*

[16] D. Simpson and P. Burns. Pulse inversion doppler: a new method for detecting nonlinear echoes from microbubble contrast agents. *Ultrasonics Symposium*, 2:1597–1600, 1997.

[17] Øyvind Standal, Thor Andreas Tangen, and Bjørn Angelsen. *A Phase Based Approach for Estimation and Tracking of Locally Variable Delays.* 2007.

[18] Thor-Andreas Tangen, Svein-Erik Måsøy, Rune Hansen, Amund Skavhaug, and Bjørn Angelsen. *Comparison of beamforming strategies for dual-frequency band imaging using a large frequency separation.* `http://ntnu.diva-portal.org/smash/get/diva2: 372555/FULLTEXT02/`.

[19] Thor-Andreas Tangen, Svein-Erik Måsøyand Øvind Standal, Rune Hansen, Jochen Deibele, Amund Skavhaug, and Bjørn Angelsen. *Suppression of linear scattering for a dual-frequency band imaging technique.* `http://ntnu.diva-portal.org/smash/get/ diva2:372555/FULLTEXT02/`.

APPENDIX A

Simulation tools

A.1 ForwardSIM

ForwardSIM is a Matlab script solving the Westervelt equation numerically. The Westervelt equation describes nonlinear wave propagation including absorption in a homogeneous medium. Taking the "linear wave propagation", "nonlinear wave propagation" and "absorption" terms from Eq. (2.16) we get:

$$\underbrace{\nabla^2 p(\underline{r}, t) - \frac{1}{c_0^2(\underline{r})} \frac{\partial^2 p(\underline{r}, t)}{\partial t^2}}_{\text{Linear propagation}} + \underbrace{\frac{\beta_{na}(\underline{r})\kappa_a(\underline{r})}{c_0^2(\underline{r})} \frac{\partial^2 p(\underline{r}, t)^2}{\partial t^2}}_{\text{Nonlinear propagation}} - \underbrace{h(\underline{r}, t) \underset{t}{\otimes} \frac{1}{c_0^2} \frac{\partial^2 p(\underline{r}, t)}{\partial t^2}}_{\text{Absorption}} = 0 \qquad \text{(A.1)}$$

The equation is unable to describe scattering, but is useful in order to simulate beam profiles from various transducer apertures. ForwardSIM is similar to Abersim [1], but also allows for use of Euler integration. The ForwardSIM script is written by Johannes Kvam, but has being changed to include the possibility to transmit pulses generated from Xtrans and from water tank recordings. The "transducer aperture function" and the "focusing function" suited for the VORA II transducer have also been rewritten. The "transducer aperture function" and "focusing function" do the same as those in Abersim [1]. Fig. (A.1) shows how the aperture and focus are selected by the total number of transducer elements, N, the number of points within each element, n, the element size, e, and the spatial resolution dx.
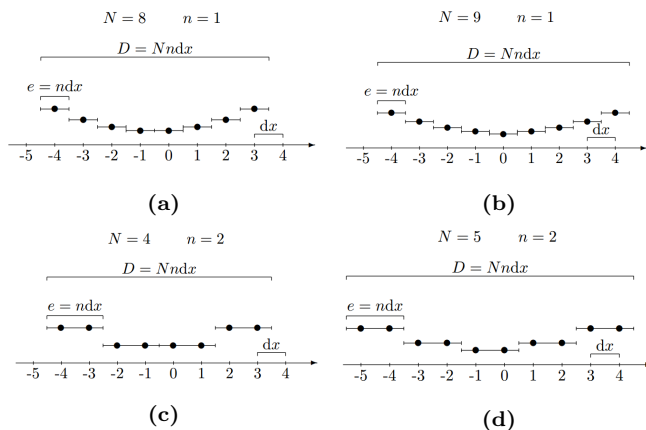
Figure A.1: *Transducer aperture setup in ForwardSIM (the figure is taken from [1]).*

A.2 Xtrans

Xtrans is a Matlab script used for calculating the electric to acoustic transfer functions for a specified transducer stack. It also calculates the input admittances for each pair of electrodes on each side of the piezoelectric composites. Xtrans computes the one dimensional transducer stack by the transmission line model given in [13], it uses an iterative scheme computing each frequency separately. Although Xtrans does not compute a three dimensional model with transient motion, it gives an understanding of the behavior of the transducer stack.

APPENDIX B

Detailed description of producing the agar gel

This chapter is mainly a reiteration of the procedure of making the agar gel found in [7].

List of equipment used for making the phantom

- A high resolution weight scale.

- Two magnetic stirring bars.

- Thermometer.

- Pipettes.

- One hot plate with a magnetic stirrer.

- One magnetic stirrer.

- A water aspirator.

- A rubber tube.

- A water tap.

- A conical flask with sidearm of size $1000ml$.

- A rubber stopper for the $1000ml$ conical flask with sidearm.

- A conical flask of size $250ml$.

- A conical flask of size $1500ml$.

- Container made by plexiglass.

- One measuring cylinder of size 200*ml*.

- One measuring cylinder of size 100*ml*

- Two measuring cylinders of 50*ml*.

- Two tweezers.

- A magnifying glass

- Toothpicks of Wood.

- Aluminum foil.

List of chemicals used for making the phantom

- Sephadex with bead size 20-80 μm. From Sigma-Aldrich type "Sephadex G-25 fine", article number G2580.

- Agar

- Glycerol

- Benzoic acid

- Distilled water

- Calcium particles of size 190 μm

Table B.1: *Material content of the two phantoms*

	Agar [g]	Sephadex [g]	Glycerol [ml]	Distilled water [ml]	Benzoic acid [ml]	Ca particle size [μm]
Phantom A:	8.51	18.42	23	264.5	57.5	190
Phantom B:	10.60	23.00	28.7	330.0	71.7	190

B.1 Procedure for making the phantoms

Producing the Benzoic Acid Soloution

- 0.55g benzoic acid was placed in a 250ml flask.

- Then 200ml of distilled water was added to produce a concentration of 0.022M.

- This mixture was boiled for 2 minuets while stirring with a magnetic stirrer.

- The solution was then cooled down and kept at 25°C prior to use.

Producing the agar solution

- The amount specified in Table (B.1) of Agar, Sephadex, Glycerol and distilled water was weight/measured into a 1000ml conical flask with sidearm.

- The top of the conical flask was coved with a cork, so the sidearm was the only exit.

- The mixture was then placed on a hot plate with a magnetic stirrer.

- The rotation speed of the magnetic stirrer bar was kept low to prevent creating air bubbles.

- After boiling the solution for 5 minutes the conical flask was placed on a separate plate (also with a magnetic stirrer but without heating).

- The rubber tube was connected to the side arm and the water aspirator before the water tap was turn on (for producing partial vacuum).

- At 80°C the amount specified by Table (B.1) of benzoic acid was added.

- At a temperature between 40°C and 41°C the solution was poured into the plexiglas container up to first reference line. The remaining gel was then placed on the hot plate at temperature 45°C.

- The calcium particles which had already been selected, and placed on a sheet of aluminum foil were now positioned as one cluster under the plastic layer(s) and as one cluster beside the plastic layer(s).

- At last the remaining gel was poured up to the wanted level.

Tips and pitfalls

- While waiting for the solution to cool down to 40/41°C, keep the pressure high enough to avoid boiling the solution which will creates air bubbles.

- Have everything prepared for placing the calcium particles as quick as possible. A smooth interface between the first and second layer is only achieved by pouring the second layer before the surface of first layer has completely stiffened.

- The calcium particles had a tendency to stick to the tweezer, making it difficult to drop the particles. Using a toothpick made by wood to gently slide across the tweezer performed well in removing the particles. In order to use a toothpick under the plastic layer, the toothpick was taped in an angle of 90° on a tweezer. This tweezer was then held by another person and slided down behind the plastic layer positioning the toothpick right under the plastic layer.

- Draw a map of the calcium particles right before pouring the second layer. The map is useful for relocalization the particles after the phantom is made.

- To reduce the bacterial growth the phantom shall be kept in a refrigerator, and to prevent the phantom drying up it needs to be kept with distilled water on top.

B.2   Phantom containers considerations

In an attempt to reduce reflections from the container a wool felt was glued on the bottom. The wool felt was considered to produce a more diffuse scattering, but since air inside the wool felt gave problems with air bubbles in the agar gel was it removed.

Two steel clamps connects the plastic layer to the Plexiglas box. From experience with Phantom box A the steel clamps in Phantom box B were changed to stainless steel because the benzoic acid got the original steel clamps to corrode.

(a) *Phantom box A: Back view*   **(b)** *Phantom box B: Back view*

(c) *Phantom box A: Top view*   **(d)** *Phantom box B: Top view*

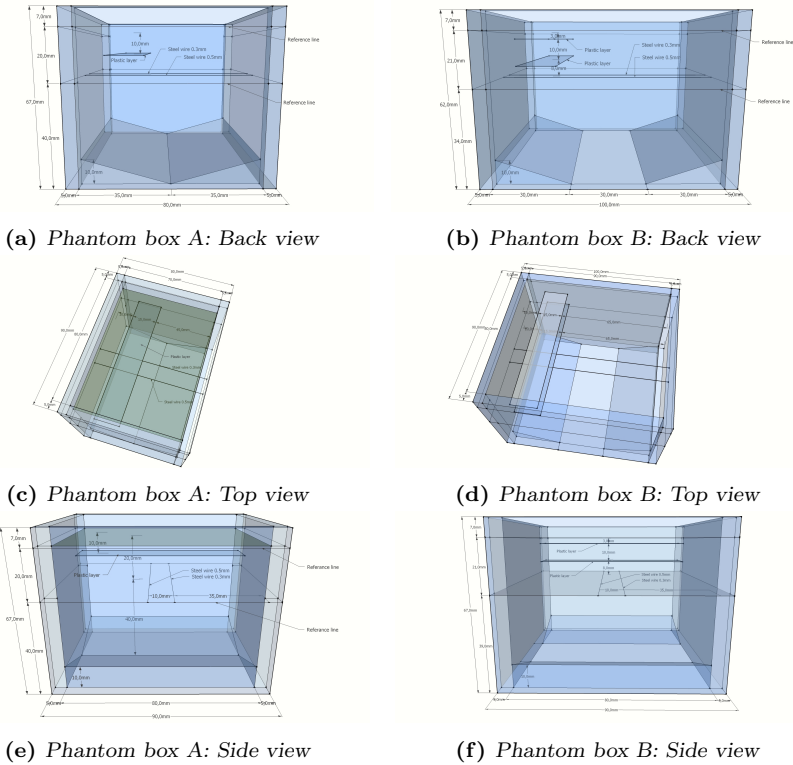**(e)** *Phantom box A: Side view*   **(f)** *Phantom box B: Side view*

Figure B.1: *Design sketches of the phantom containers made in Sketchup [3].*

APPENDIX C

Water tank recordings

To get an overview over the transmit setup water tank recordings were performed. The two main tasks were:

- SURF pulse complex characterization

- Beamfield characterization

The recordings were done at the Department of Circulation and Medical Imaging with access to:

- Onda HGL-0200,S/N1426 (hydrophone)

- Onda AH-2010,S/N1223 (preamp)

- LeCroy wave surfer 44xs (oscilloscope)

- Stepper motor (moving relative hydrophone position)

- Computer with "Probelab 1.5" (Matlab Software)

C.1   SURF pulse complex characterization

The SURF pulse complexes needed to be characterized for obtaining the relative position of the HF pulse to the LF pulse. The pulses were also recorded for use in ForwardSim simulations. For this experiment the hydrophone was placed right below the transducer center point. The distance from the transducer to the hydrophone is less then $2mm$, and the recorded pulses are therefore approximated to be equal the transmitted pulses.
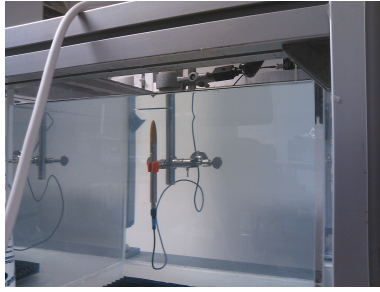
Figure C.1: *Water tank setup with the hydrophone located below the VORA II transducer.*

HF pulses

It was initially intended to use 8MHz pulses instead for 10MHz pulses, and therefore 8Mhz pulses are investigated in this section. The recorded HF pulses were low pass filtered with a sharp cutoff at frequency 40MHz and averaged over 64 pulses. In addition to achieve high axial resolution it is an advantage that the HF pulse in the SURF pulse complex is short to reduce pulse form distortion. To explore the pulse shape with respect to the number of half cycles (NHC) excitations, the HF pulses with their complex envelopes are plotted below.

(a) *NHC 1 pulse with complex envelope*

(b) *NHC 2 pulse with complex envelope*

(c) *NHC 3 pulse with complex envelope*

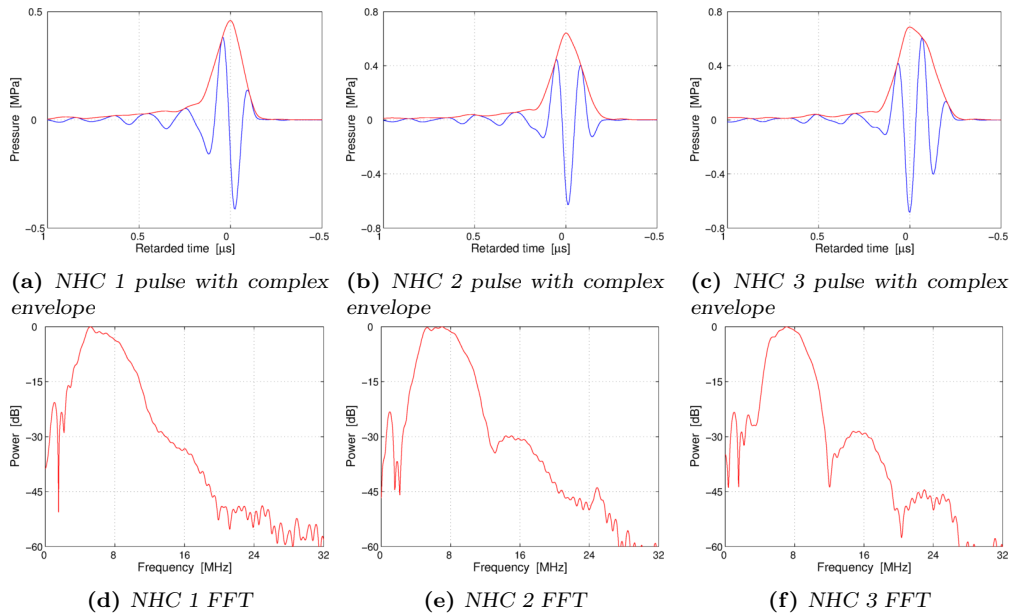**(d)** *NHC 1 FFT*

(e) *NHC 2 FFT*

(f) *NHC 3 FFT*

Figure C.2: *HF pulses excited at frequency $8MHz$ with various number of half cycles (NHC) excitation and their frequency spectra (B-Tx: Power 5dB)*

From Fig. (C.2) we can see that the HF pulse with only a half cycle excitation has the shortest temporal complex envelope. In Fig. (C.3) we can also see that the excitation voltage does

not change the pulse form so we can therefore achieve the desired pulse pressure by adjusting the excitation voltage only. For this reason pulses with only 1 NHC excitation will be used for imaging the phantoms.
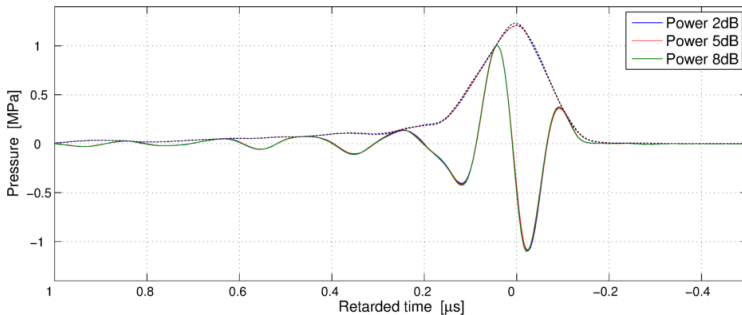
Figure C.3: *Normalized HF pulses with corresponding complex envelopes to see the dependence of the voltage on the excitation pulse (NHC = 1).*

LF pulses

The LF pulse does not have the same criteria as the HF pulse. The LF pulse can be "long" as it is filtered out both by the HF receive transfer function and in the post processing. Hence the LF pulse should have as little energy in the HF frequency band as possible. The recorded LF pulses have been low pass filtered with a sharp cutoff at frequency 40MHz.

(a) *NHC 3*   **(b)** *NHC 4*   **(c)** *NHC 5*

(d) *NHC 3*   **(e)** *NHC 4*   **(f)** *NHC 5*

Figure C.4: *LF pulses with various number of half cycles (NHC) excitation (SURF: LF Voltage 30Volt)*

89

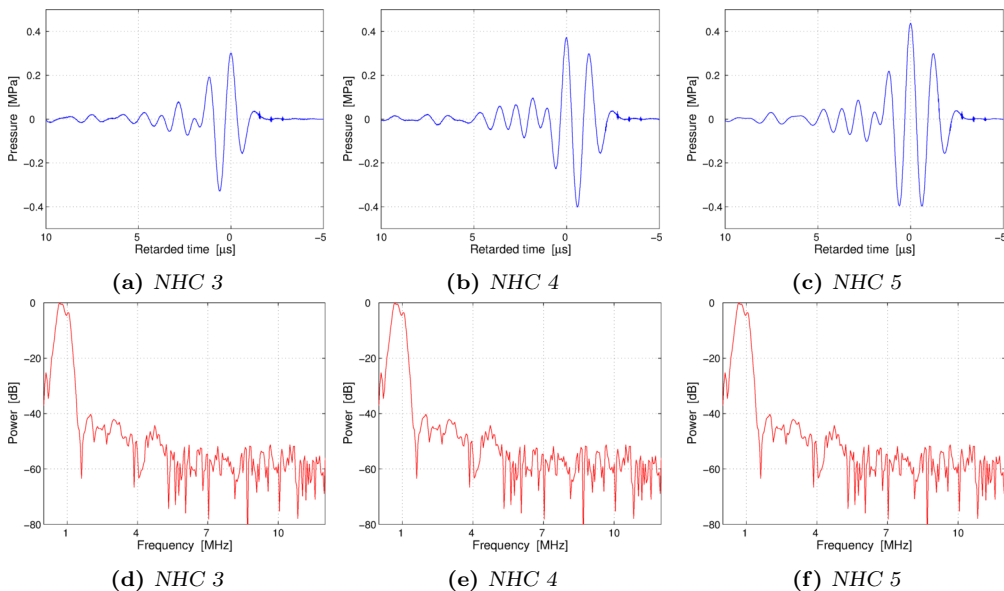The high frequency noise pulses observed in front of the LF pulses seen in Fig. (C.4) is cross coupled from the PA to the hydrophone Rx electronics. This has been verified by changing the hydrophone position and then the relative position of the LF pulse and the high frequency pulses gets changed. The applied excitation voltage does not change the relative amplitude between the LF pulse and the high frequency pulses, which proves that the coupling is proportional with the PA output voltage. The frequency spectrum of the first two high frequency pulses is shown in Fig. (C.4c).
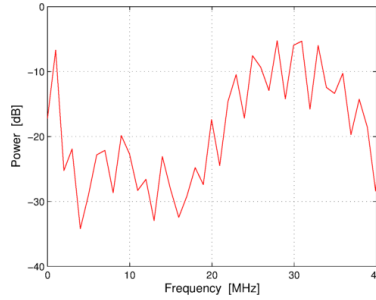

Figure C.5: *Frequency spectrum of the two high frequency pulses in front of the LF pulse in Fig. (C.4c).*

Table C.1: *HF pulses: Measurements of the maximum magnitudes [MPa] for various pulse length. "Pulse index A/B", "Pulse Repeat" and "Power" are parameters under "B-TX" in the Sonix GUI. They specify the excited pulse length in number of half cycles (NHC) and the output power.*

Pulse index A/B	Pulse Repeat	NHC	Power				
			1dB	2dB	5dB	8dB	10dB
1	1	1	-	0.280	0.414	0.609	0.735
2	1	2	-	0.425	0.631	0.810	0.816
1	2	3	0.116	0.464	0.687	0.804	-

Table C.2: *LF pulses: Measurements of the maximum magnitudes [MPa] for various number of half cycles (NHC) excitations. The specified voltage is the peak voltage (not peak to peak)*

NHC	25Volt	30Volt	35Volt	40Volt	45Volt	50Volt
3	-	0.328	-	-	-	-
4	-	0.402	-	-	-	-
5	0.376	0.437	0.516	0.580	0.685	0.763

C.2   Beam field characterization

The beam field "at" the transducer was obtained by scanning the hydrophone in both elevation and azimuth direction close to the transducer ($< 2mm$). All points were averaged over 64 beams.

Table C.3: *VORA II aperture specification*

		HF	LF
Number of elements used in azimuth	N_{Az}	20	13
Number of elements used in elevation	N_{El}	1	1
Elevation element width	El	4.0mm	8.0mm
Azimuth element pitch	p	300μm	900μm
Used azimuth width	Az	6.0mm	11.7mm

C.2.1   HF aperture

The beam field of the HF aperture was scanned while transmitting with 20 HF elements. The "B-Tx: Power" setting used was "2dB".

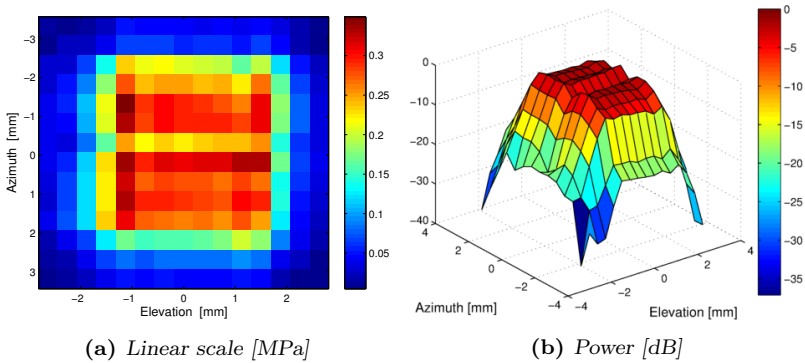**(a)** *Linear scale [MPa]*   **(b)** *Power [dB]*

Figure C.6: *Two dimensional scan of the HF aperture where the pressure plotted are the peak pressures.*

The figures in (C.6) have low step resolution because of "long" recording time. For this reason two one-dimensional recordings were performed in azimuth and elevation direction
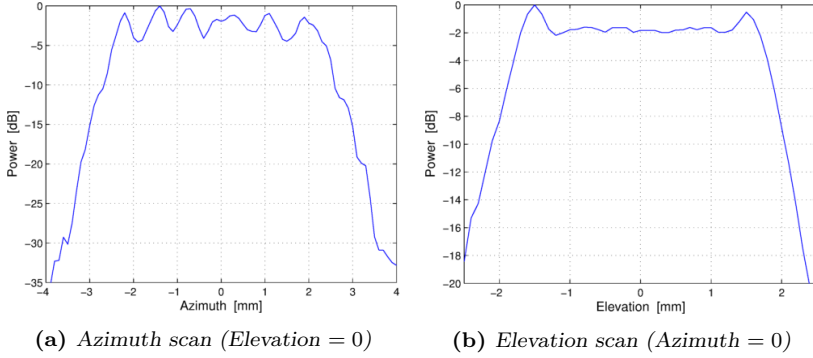
as shown in Fig. (C.7).

(a) *Azimuth scan (Elevation = 0)*   **(b)** *Elevation scan (Azimuth = 0)*

Figure C.7: *Azimuth and elevation scans at the transducer surface. The values used are from the peak pressures.*

The ripple in the azimuth profile seen in Fig. (C.7a) is almost systematically. The period of the ripple is around $0.8mm$. The reason for the periodic peaks is not known. The ripple may origin from interference patterns but this has not been shown in field simulations.

The pressure drop at azimuth equal $-0.3mm$ in Fig. (C.6a) and Fig. (C.6b) can come from a dead/poor element, or sampling from one of the dips in Fig. (C.7a).

C.2.2 LF aperture

The beam field of the LF aperture were scanned while transmitting with 13 LF elements. The "SURF: LF voltage" setting "30V" was used.
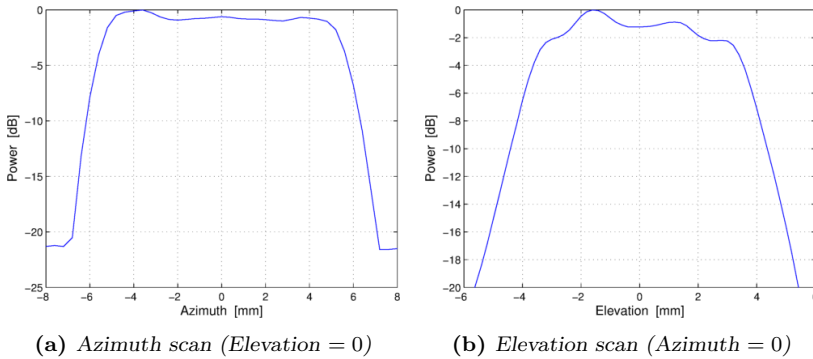

(a) *Azimuth scan (Elevation = 0)*   **(b)** *Elevation scan (Azimuth = 0)*

Figure C.8: *Azimuth and elevation scans at the transducer surface. The values used are from the peak pressures.*

APPENDIX D

Ultrasonix Sonix image parameters

The parameters listed are the main parameters influencing the recorded rf data. The values listed are the values used if not specified otherwise.

Table D.1: *SURF*

Imaging Parameters	Values		
	Setup 1	Setup 2	Setup 3
SURF Mode On:	1	1	
SURF LF Freq:	0.8MHz	0.8MHz	
SURF LF Voltage	50Volts	50Volts	
SURF LF Half Cycles:	5	5	
SURF LF Flip:	1	1	
SURF LF Plane Wave:	1	1	
SURF LF Center Active:	1	1	
SURF LF Outer Active:	1	1	
SURF LF Relative Apt Size:	200	200	
SURF HF Position:	0%	0%	
SURF Zero Adjust Delay:	510ns	510ns	

Table D.2: *B-GAIN*

Imaging Parameters	Values		
	Setup 1	Setup 2	Setup 3
TGC: Analog: [C]	10,20,55,40	10,30,55,70	
TGC: Depth:	40mm	40mm	
VCA Amplification:	20	20	

Table D.3: *B-Rx*

Imaging Parameters	Values		
	Setup 1	Setup 2	Setup 3
Rx Aperture Max:	32	32	
Sound Velocity:	1540	1540	
B Weight Type:	0	0	
Rx F Number:	50	50	

Table D.4: *B-FOCUS*

Imaging Parameters	Values		
	Setup 1	Setup 2	Setup 3
Focus Count:	1	1	
Focus Depth:	20.0mm	20.00mm	

Table D.5: *B-Tx*

Imaging Parameters		Values	
	Setup 1	Setup 2	Setup 3
Tx Frequency:	10MHz	10MHz	
Tx Aperture: [C]	10,50,100,50	10,50,100,50	
Tx Aperture Max:	10	10	
Tx Curve depth:	20.00mm	20.00mm	
Pulse Index A:	1	1	
Pulse Index B:	1	1	
Pulse Repeat:	1	1	
Tx Delay:	60	60	
Power:	8dB	8dB	
Voltage+:	15	15	
Voltage-:	15	15	
Voltage Offset+:	0	0	
Voltage Offset-:	0	0	

APPENDIX E

Matlab code

The Matlab code selected contains the functions needed to fit the time delay estimate to a polynomial, and is what considered to be useful for future students.

```
1  degree = 3;                                  % Degree of polynomial
2  nRem   = 340;;              % Initional number of samples zero weighted
3  nt     = 2000;                               % Number of rf samples
4  nt0    = 116;                          % Number of zero padded samples
5  %The Weights in range [0 1]
6  Weights = [zeros(nRem,1); ones(nt+nt0—nRem—100,1); zeros(100,1)];
7  it = 4;                                      % Number of iterations
8  boundary = 3e—9;
9  [tau_i weights] = TauDevelopment2(tau_image_bilat, NCH, degree,...
10                  it, boundary);
```

```
1  function [tau_i weights] = TauDevelopment(tau_image_bilat, NCH, degree,...
2                                            Weights, it, boundary)
3  % TauDevelopment uses the function "polyfitCon" to fit the nonlinear time
4  % delay, tau, to a polynom. This is done for each scanline, and an
5  % iterative method is used to remove estimating tau from areas with
6  % noise and reverberations.
7  %
8  % Input:
9  %       — The result for the phase based estimation "tau_image_bilat".
10 %       — Total number of scanlines "NCH"
11 %       — Degree of polynomial "Degree"
12 %       — Initial weighting function "Weights"
13 %       — Total number of iterations "it"
14 %
15 % Output:
16 %       — Fitted tau(i) "tau_i"
```

```
17  %        — Weights for each scanline "weights"
18  %
19  nt = size(tau_image_bilat,1);
20  weights = zeros(nt,NCH);
21  tau_i   = zeros(nt,NCH);
22  for CH=1:NCH
23      org_tau = tau_image_bilat(:,CH);
24      tau_fit1 = polyfitCon(org_tau, Weights, degree);
25      for itNr=0:it—2
26          for ii = 1:nt—1
27              if abs(org_tau(ii) — tau_fit1(ii)) > boundary*exp(—itNr*0.3)
28                  Weights(ii) = 0;    %Remove weighting tau with reverberations ...
                            and noise
29              end
30          end
31          tau_fit1 = polyfitCon(org_tau, Weights, degree);
32      end
33      weights(:,CH) = Weights;
34      tau_i(:,CH)   = tau_fit1;
35  end
36  end
```

```
1   function fittedtau = polyfitCon(tau, Weights, degree)
2   % Function fits the input vector "tau" to a polynomial with "degree"
3   % with weights "Weights".
4   %
5   %  Output:
6   %        — The fitted version of "tau"
7   %
8       [xData, yData, weights] = prepareCurveData( [], tau, Weights );
9       % Set up fittype and options.
10      polytype = sprintf('poly%d',degree);
11      ft = fittype(polytype);
12      opts = fitoptions( ft );
13      opts.Lower = —Inf;
14      opts.Upper = Inf;
15      for ii=1:degree—1
16          opts.Lower = [opts.Lower —Inf];
17          opts.Upper = [opts.Upper Inf];
18      end
19      opts.Lower = [opts.Lower 0];
20      opts.Upper = [opts.Upper 0];
21      opts.Weights = weights;
22      % Fit model to data.
23      fittedobject = fit( xData, yData, ft, opts );
24      fittedtau = fittedobject(1:length(tau));
25  end
```